Engineering the optical properties of subwavelength devices and materials

by

Vikas Anant

Submitted to the
Department of Electrical Engineering and Computer Science
in partial fulfillment of the requirements for the degree of

Doctor of Philosophy in Electrical Engineering

at the

MASSACHUSETTS INSTITUTE OF TECHNOLOGY

September 2007

Author .....
Department of Electrical Engineering and Computer Science
August 31, 2007

Certified by .....
Karl K. Berggren
Associate Professor
Thesis Supervisor

Accepted by .....
Arthur C. Smith
Chairman, Department Committee on Graduate Students

Engineering the optical properties of subwavelength devices and materials

by

Vikas Anant

Submitted to the Department of Electrical Engineering and Computer Science on August 31, 2007, in partial fulfillment of the requirements for the degree of Doctor of Philosophy in Electrical Engineering

Abstract

Many applications demand materials with seemingly incompatible optical characteristics. For example, immersion photolithography is a resolution enhancing technique used to fabricate the ever-shrinking nanostructures in integrated circuits but requires a material that has—at the same time—a large index of refraction and negligible optical loss. Other applications require devices that have optical properties that seem exorbitant given the constraints posed by the geometry, materials, and desired performance of these devices. The superconducting nanowire single-photon detector (SNSPD) is one such device that, on the one hand, needs to absorb and detect single telecom-wavelength photons ($\lambda = 1.55$ μm) with near-perfect efficiency, but on the other hand, has an absorber that is subwavelength in its thickness ($\lambda/390$). For both cases, it is simply not enough to look for alternative materials with the desired optical properties, because the materials may not exist in nature. In fact, it has become necessary to engineer the optical properties of these devices and materials using other means.

In this thesis, we have investigated how the optical properties of materials and devices can be engineered for specific applications.

In the first half of the thesis, we focused on theoretical schemes that use subwavelength, resonant constituents to realize a material with interesting optical properties. We proposed a scheme that can achieve high index ($n \gg 6$) accompanied with optical gain for an implementation involving atomic vapors. We then explored the applicability of this high-index system to immersion lithography and found that optical gain is problematic. We solved the issue of optical gain by proposing a scheme where a mixture of resonant systems is used. We predicted that this system can yield a high refractive index, low refractive index, anomalous dispersion, or normal dispersion, all with optical transparency.

In the second half, we studied the optical properties of SNSPDs through theoretical and experimental methods. In the study, we first constructed a numerical model that predicts the absorptance of our devices. We then fabricated SNSPDs with varying geometries and engineered a preprocessing-free proximity-effect correction technique to realize uniform linewidths. We then constructed an optical apparatus to mea-

sure the absorptance of our devices and showed that the devices are sensitive to the polarization of single photons.

Thesis supervisor:

Karl K. Berggren
Associate Professor

Acknowledgments

This thesis is dedicated to my wife **Umaa Rebbapragada** who I was fortunate enough to meet during my time at MIT and is the most prized, (unpublished) result of my Ph.D. (sorry Karl!) My time at MIT would not have been fruitful and/or enjoyable if it were not for:

Professor **Karl Berggren**, who gave me the opportunity to learn from and work with some brilliant minds, including his own;

Professors **Steven Johnson** and **Terry Orlando**, who graciously agreed to be in my committee and gave me valuable feedback;

Ayman Abouraddy, who has been a friend, collaborator, and mentor;

Eric Dauler, **Jamie Kerman**, and **Magnus Rådmark** who have made meaningful contributions to the results published in this thesis;

Joel Yang, one of the aforementioned brilliant minds, who has not only been a great colleague, but also someone who will always be a part of my family along with his wonderful wife **Ari** and baby **Michael**;

Kris Rosfjord, yet another brilliant mind, for her cheerful disposition, physics knowledge, and yummy cookies;

Charles Herder, for being a great help during testing experiments;

Jim Daley and **Mark Mondol**, who supported me and countless other graduate students in the Nanostructures Lab;

Tiffany Kuhn and **Cindy Gibbs**, for patiently placing a great many orders for me;

Jerimy Arnold, who was my office mate, ski buddy, lunch buddy, and partner in crime as we made fun of...

Stefa(aaaaaaa)n Harrer, who is seelenruhig, ein helles Köpfchen, lebenslanger Freund, and also taught me my first German phrase "wo est mein auto verdammt!"

Amil Patel, who was my lunch buddy, friend, ex-roommate, and may revolutionize nanotechnology one day;

Knut Gezelius, and **Erwan Salaün**, who made the Ph.D. more enjoyable by being great roommates and tennis coaches to me;

Karen & Al Blum, and **Francine & Eric Chittenden**, who are among the nicest and warmest people I have ever met (times two), who have all-but-adopted me as their own son;

Vikrant Agnihotri and **Sushil Kumar**, who have both been good friends and colleagues;

Vikram 'Sampras' Sivakumar, who has been a good friend and reliable tennis partner;

and my **family** who have lovingly supported me throughout my academic career.

Contents

List of Figures

List of Tables

Chapter 1

Introduction

This thesis is fundamentally about the interaction of light with matter, a subject that has been studied for decades. So what makes this interaction so intriguing even today?[1] Because it is only very recently that we have been able to control *and exploit* the interaction of light and matter on a truly grand scale and with great impact. One example of the high impact of light-matter interactions can be found in the electronics industry, where exquisite control of this interaction has enabled data storage media, microprocessors, and wireless devices to be ubiquitous. Advances in technology that can generate, control, and detect light have given the world high-speed intercontinental optical communication and have ushered in a new age of information technology. There is still much to discover relating to the interaction of light and matter that, with further research, development, and commercialization, may have a similar impact.

This thesis is divided into two distinct parts, each relating to how we can control the interaction between light and matter to our advantage.

In the first part, I will describe ways to control the optical properties of subwavelength materials using quantum-optical techniques. The central result in this part is a conceptual framework for designing optical materials where the susceptibility χ, a parameter that describes the response of matter to light, can be precisely controlled. A key element of this result is that these optical materials exhibit transparency and do not require quantum coherence.

[1] One can equally wonder, why should I read this thesis?

Major applications of the proposed materials include optical immersion lithography and optical communications, both of which are indispensable to the high-tech industry. Other applications include devices that enable optical storage and buffering in quantum computing, an area that holds promise for the future.

The second part of this thesis investigates the optical properties of devices called superconducting nanowire single-photon detectors (SNSPDs) that, as the name suggests, can detect single quanta of light. In this device, light and matter interact to produce an electrical signal when a single photon disrupts the superconductivity in a nanowire. However, whether the photon is absorbed, reflected without detection, or transmitted is determined by the optical properties of the device which contains subwavelength features. The central results of this part consist of modeling and experiments that determine the optical absorptivity of SNSPDs. A key finding of this part is that these devices are sensitive not only to single photons, but also to their polarizations.

The impact of knowing the optical properties of these devices is that the optical designer can use the optical model to design higher efficiency devices. High efficiency single-photon detectors are required for future quantum key distribution (QKD) networks and free-space optical communication. SNSPDs are particularly promising for these applications because they have roughly 1000 times faster response and low jitter (on the order of 10's of picoseconds).

Part I

Controlling the properties of subwavelength optical materials

Chapter 2

Introduction to refractive-index engineering

In this chapter, we will introduce the reader to a number of concepts related to the refractive index and absorption. This knowledge will allow us to discuss the major applications that drive the development of materials with unique optical properties.

The refractive index n is a quantity that plays a part in many optical phenomena. Lets consider a simple example that illustrates the effect of n on three optical phenomena: angle of propagation, wavelength, and speed of propagation. Figure 2-1 shows a lossless dielectric medium with index $n_{\mathrm{d}} > 1$ at an interface with air ($n_0 = 1$). Also pictured in this figure is a plane wave with free-space wavelength λ_0 approaching this air-dielectric interface at an angle θ_0 with respect to the normal with speed c_0. The refractive index of both air and dielectric influence the propagation direction of the wave when it is in the dielectric medium via Snell's law: $n_0 \sin\theta_0 = n_{\mathrm{d}} \sin\theta_{\mathrm{d}}$. The dielectric index also changes another property of the light in the dielectric medium: the wavelength. In this example, the wavelength scales down from λ_0 in air to λ_0/n_{d} in the dielectric. The third optical property of light that is impacted by the dielectric refractive index is the speed of propagation, which is slowed down by a factor of $1/n_{\mathrm{d}}$.

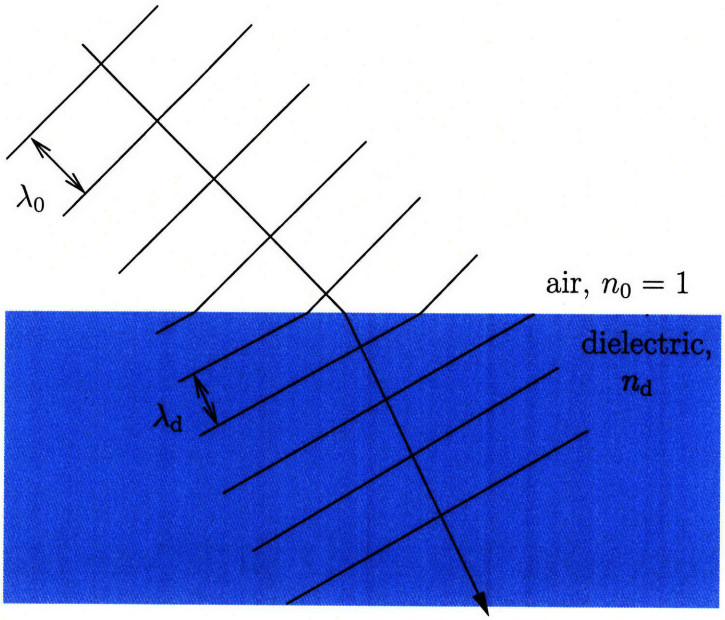

Figure 2-1: Schematic of a wave propagating across an air-dielectric interface. The refractive indices n_0 and n_d influence the angle of propagation, wavelength, and speed of the wave in the dielectric medium. Parallel lines signify constant phase fronts of the wave. The reflected wave is not pictured.

2.1 Applications and prior work

2.1.1 Immersion lithography

In this thesis, we will apply refractive-index engineering techniques to many applications. One application that we will focus on is optical lithography, where the need for materials with a large refractive index and low absorption is immediate. Optical lithography is a process by which a pattern is transferred, usually with a reduction in size using lenses, to a photosensitive material. Immersion lithography, a variant of optical lithography, is a technique where a fluid with refractive index n, sandwiched between the lens system and the photosensitive material, is used to further reduce the size of the pattern by a factor of n. A schematic of an immersion lithography system is shown in Fig. 2-2. The immersion fluid used today is water because of its elevated refractive index and low optical losses at 193 nm wavelength [1]. 193 nm water immersion has been used to achieve 65 nm half-pitch features, and is currently

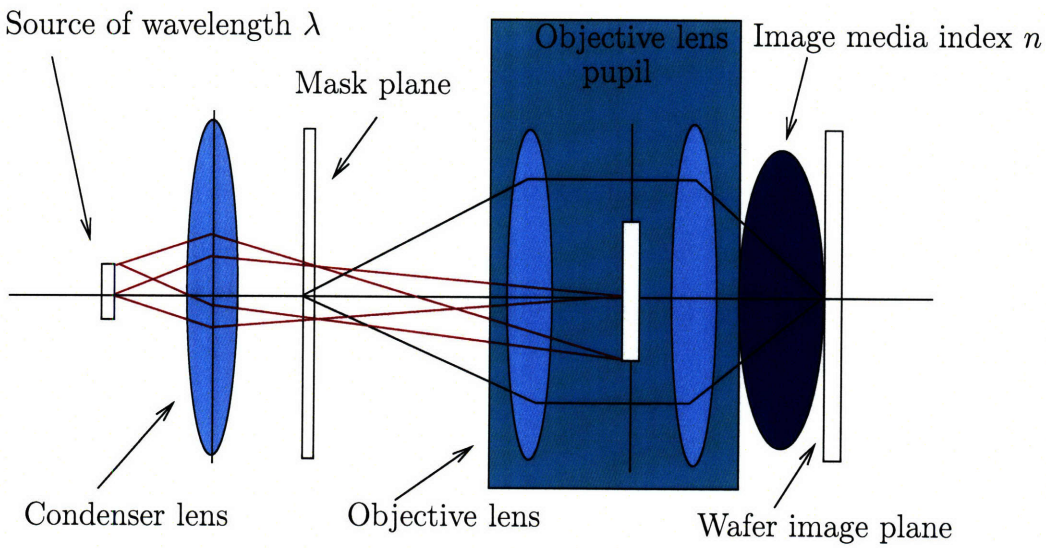

Figure 2-2: Schematic of an immersion lithography tool showing the path of the light as it passes through a condenser lens, mask, objective lens, and immersion fluid to form an image on the wafer. Reproduced from Ref. [3].

being developed to produce 45-nm-half-pitch features [2]. Because immersion lithography has been recognized as a cost-effective alternative to scaling the optical source wavelength, the industry is betting on it to realize 32-nm- and even 22-nm-half-pitch features [2]. The challenge will be to find a fluid with two seemingly incompatible characteristics: a high index of refraction *and* low absorption. In the next two chapters of this thesis, we will examine refractive-index engineering techniques that may yield immersion fluids of the future.

2.1.2 Fast and slow light

In this thesis, we will also focus on finding refractive-index engineering techniques for applications where the speed of light needs to be altered. These applications include optical buffers [4,5], optical switches [6], and new schemes for optical quantum computing [7]. In some cases, the speed of light can be reduced by increasing the refractive index by changing a physical property (e.g. the thermo-optical effect), or by using a special structure (e.g. photonic crystals [8], coupled-resonators [9]). But in other cases, light can be sped up [10], slowed down [10, 11], and even brought to a complete halt [12–14] using a different technique. In these experiments, the speed

of light was manipulated by an abrupt change in the refractive index change with frequency. But to succeed in observing fast or slow light in many of these experiments, the researchers required advanced quantum-optical techniques that suppressed loss. These techniques came at the expense of increased experimental complexity and do not bode well for practical implementations. In this thesis, we will describe techniques that can achieve the same optical effects with more straight-forward implementations.

2.1.3 Near-field lithography

Another application that refractive-index-engineered materials can impact is near-field optical lithography. In near-field lithography, the evanescent field from a mask under illumination is used to expose resist on a substrate. An advantage of near-field lithography is its potential to realize structures with dimensions much smaller than the wavelength of illumination. But because evanescent fields decay exponentially, for near-field lithography to work, the mask must be brought very close to the resist. In practice, the proximity of mask to resist can be difficult to achieve without using fragile conformal masks.

One way to overcome the problem of rapidly decaying evanescent fields is to build a lens that amplifies them. In general, the material that composes such a lens needs to have a negative refractive index [15].[1] Achieving a negative refractive index is not easy: it requires both the permittivity ϵ and permeability μ to be negative so that by causality, the negative sign is taken for the refractive index in $n = \sqrt{\epsilon\mu}$ [17]. These materials do not exist in nature, however, can be engineered out of subwavelength components that enable $\epsilon < 0$ and $\mu < 0$.

While negative-refractive index lenses have been demonstrated at microwave frequencies [18–20], but it has been difficult to realize them at optical frequencies because it is difficult to get both ϵ and μ to be negative simultaneously in optical materials. Recently, a metamaterial has been developed that uses plasmon resonances in metallic nanorods to exhibit a negative index of refraction for optical wavelengths [21].

[1] Lou *et. al.* have shown that it is possible to achieve negative refraction without requiring negative refractive index using photonic crystals, albeit for a narrow band of frequencies [16].

However, this metamaterial has yet to be used as a near-field lens.

It turns out that a near-field lens that amplifies normally evanescent fields can also be made using a material with only a negative permittivity, so long as the lens is thin [15]. Metals, such as silver, possess a negative permittivity at optical frequencies below their plasma frequency, and have been used successfully in near-field lithography experiments to demonstrate subwavelength image transfer [22, 23]. In these experiments, absorption severely limits the fidelity of image formation. In this thesis, we will describe a technique to eliminate absorption from a near-field lens with negative permittivity.

2.2 Tackling the problem of absorption

Before we address how to remove absorption, let us first clarify what we mean by absorption. In the applications mentioned in Section 2.1, we define absorption as a loss of energy (or photons) in the electromagnetic field as it propagates from the source to the destination. The energy can be lost to photons in other directions, photons of different frequencies, or via heat or collisions. We will now look at a way to remove the absorption for these applications.

2.2.1 The quantum-optics approach to removing absorption

Absorption is a problem for all applications of refractive index engineering. Fortunately, solutions to this problem can be found in the field of quantum optics. One of the first experiments that suppressed absorption was conducted by Harris and coworkers, where they proposed a scheme involving quantum interference called electromagnetically induced transparency (EIT) [24]. In EIT, two coherent quantum states are destructively interfered in a multi-level atomic system. As a result of this interference, photons at a particular frequency are not absorbed. This scheme has been experimentally demonstrated [25] and many variants have been suggested [7, 26–30]. A good review of EIT can be found in Ref. [31].

But EIT comes with its own set of problems that are pragmatic in nature. For

many applications, EIT is not practical because it requires quantum coherence and can require complicated optical techniques to realize. In addition, EIT is useful only for slow and fast-light applications: the benefit in refractive index enhancement is minute (parts per ten thousand at best) [25]. A larger n is desired for applications like immersion lithography.

Larger refractive indices – upwards of 10 – are achievable by using optical resonances [32]. However the problem with optical resonances is that they are strongly absorbing near their resonant frequency. In the following section, we will examine an optical resonance using classical mechanics of electron motion, and see how absorption accompanies a high refractive index. In the next chapter, we will look at the quantum mechanical picture of a resonance and see how to use the results to eliminate absorption.

2.2.2 Absorption near an optical resonance

The qualitative picture

In the classical picture of light-matter interaction, light interacts with matter through the electrons present in the medium. Electromagnetic waves that oscillate at a particular frequency interact with electron clouds that surround the nuclei in a medium and drive the motion of these clouds at the frequency of the field. An electromagnetic wave is said to be on resonance with a medium when the frequency of excitation matches the frequency of the transition between two electron orbitals. At this resonant frequency, the electromagnetic wave maximally transfers energy to the electron cloud motion, which in turn emits light back into the total field. The light emitted back into the total field by the atom is 180 degrees out of phase with the incident light, leading to destructive interference and a decay of the total field. Other losses occur through spontaneous emission which is incoherent with the incident field and emits into all angles; and collisions, which cause the electron motion of multiple electron clouds to dephase with respect to each other and cause an exponential decay in the total vibration.

The quantitative picture

We will now derive the mathematical relationship between the electric field and electron motion [33], and find the frequency dependence of susceptibility χ, a parameter that is related to the refractive index via $n = \sqrt{1+\chi}$, near a resonance. Let the vector of displacement of an electron cloud from its rest position be given by $\vec{s}$. The displacement follows the differential equation

$$\ddot{\vec{s}} + g\,\omega_0\,\dot{\vec{s}} + {\omega_0}^2\vec{s} = \frac{q}{m}\vec{E}, \tag{2.1}$$

where

ω_0 is the resonant frequency,

g is a dimensionless damping constant (attributed to spontaneous emission and collisions),

$q = -1.60210^{-19}$ C is the electron charge,

m is the electron mass,

and $\dot{\vec{s}}$ denotes a time derivative of $\vec{s}$.

Let $\vec{E}$ be a plane wave given by

$$\vec{E} = \hat{\alpha}E_0 e^{i(\vec{k}\cdot\vec{r}-\omega t)}, \tag{2.2}$$

where $\vec{k}$ is the wave vector, ω is frequency, E_0 is amplitude, and polarization is given by $\hat{\alpha}$. If we assume that $\vec{s}$ has an $e^{i(\vec{k}\cdot\vec{r}-\omega t)}$ dependence, then we can replace $\dot{\vec{s}}$ with $-i\omega\vec{s}$ and $\ddot{\vec{s}}$ with $-\omega^2\vec{s}$ to obtain the solution

$$\vec{s} = \frac{q/m}{(\omega_0^2 - \omega^2) - i\,\omega_0\,\omega\,g}\vec{E}. \tag{2.3}$$

We can relate the electron motion to the polarization $\vec{P}$ through

$$\vec{P} = Nq\vec{s}, \tag{2.4}$$

where N is the electron density. The polarization is related to the electric field via

$$\vec{P} = \epsilon_0 \chi \vec{E}. \tag{2.5}$$

Combining Eqs. (2.3), (2.4), and (2.5), we get an expression for the susceptibility as a function of frequency ω given by

$$\chi(\omega) = \frac{Nq^2}{m\epsilon_0} \frac{1}{(\omega_0^2 - \omega^2) - i\omega_0 \omega g}. \tag{2.6}$$

Finally, we can simplify Eq. (2.6) near resonance by making the substitution $\omega + \omega_0 \sim 2\omega$ to obtain

$$\chi(\omega) = \frac{Nq^2}{2\omega m\epsilon_0} \frac{1}{(\omega_0 - \omega) - i(\omega_0 g/2)}. \tag{2.7}$$

Absorption occurs when the field given by Eq. (2.2) reduces in magnitude, which only occurs when there is an imaginary component of $\vec{k}$. Since $|\vec{k}| = \omega n/c$, an imaginary component of n clearly attenuates $\vec{E}$. If we relate $n = n' + in''$ to $\chi = \chi' + i\chi''$ through $n = \sqrt{1+\chi}$, we find that sgn(n'')=sgn(χ'').[2]

A plot of the real and imaginary parts of the susceptibility as a function of frequency, as shown in Fig. 2-3, reveals the problem with using resonances for refractive index engineering. We find that a positive χ'', associated with absorption, is centered around ω_0 and accompanies the features of χ' that are required for interesting optical phenomena, i.e. $\chi' \gg 0$, (high index) $\chi' \ll 0$ (low index) and $d\chi'/d\omega \ll 0$ (anomalous dispersion).

2.2.3 Eliminating absorption from resonances

But optical resonances do not always need to be accompanied by absorption. To understand how absorption can be eliminated from a resonant system, we need to describe a resonance using quantum-mechanical language. In the next chapter, we

[2] n'' is also denoted as κ in many texts. There are also different conventions used in the literature with the sign of $n'' \equiv \mathrm{Im}(n)$ that lend themselves to how the complex exponential in Eq. (2.2) is defined by different authors. Sometimes $\mathrm{Im}(n) > 0$ and other times $\mathrm{Im}(n) < 0$ so be sure to check the definition.

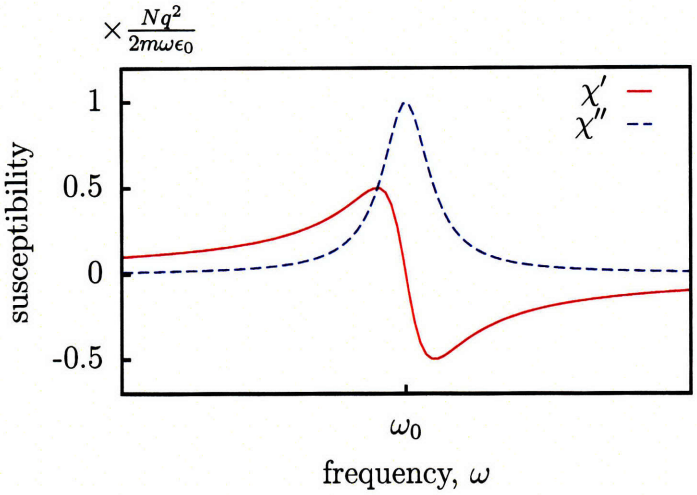

Figure 2-3: Plot of the real (χ') and imaginary (χ'') components of the susceptibility $\chi = n^2 - 1$ as a function of frequency ω near an optical resonance centered at ω_0. This plot shows that while it is possible to obtain large index ($\chi' \gg 0$) near a resonance, it is accompanied with large absorption ($\chi'' \gg 0$).

will see how a quantum-mechanical resonance allows for high index with amplification instead of absorption. We will also examine the utility of a medium with high index and amplification to immersion lithography. In Chapter 4, we will describe a different scheme where absorption is replaced with transparency. Different permutations of this scheme result in high index, low index, and large changes in index, all accompanied by transparency. We will describe two implementations of this scheme, one useful for fast/slow light and the other for near-field microscopy.

Chapter 3

High index with amplification

In this chapter, we will use the language of quantum mechanics to relate susceptibility to frequency near an optical resonance. We will find that, just in the classical case discussed in the last chapter, absorption masks the interesting optical phenomena present in the susceptibility spectrum. But we will also find that the quantum mechanical treatment has an advantage over the classical treatment of absorption near resonance.

We will examine a pumped two-level system that can achieve population inversion, which is a non-classical concept. Using this system, we can eliminate absorption and instead have amplification accompany an enhanced index of refraction [34]. We predict that a refractive-index of ~ 6 without requiring quantum coherence for reasonable experimental parameters. In comparison, other quantum-optics-based index-enhancement techniques achieve enhancements of only $\Delta n \approx 10^{-4}$ due to practical experimental obstacles, and moreover, require quantum coherence [25]. In principle, the refractive index can be enhanced beyond 6 by using other the experimental parameters. An index as high as this may be useful for applications in microscopy [35], all-optical switching, and optical buffering [36].

We will focus on the application of pumped atomic systems to immersion lithography. In immersion lithography, a fluid with index n_{fluid} sits between the final lens (with index n_{lens}) and resist-coated substrate and improves the resolution by a factor of n_{fluid}. If an atomic system were used as a high-index immersion fluid, it needs to

have a high index of refraction without absorption, and not require multiple phase-locked lasers, quantum coherence, or even collinearity between a pump and probe source. In this chapter, we will see that despite fulfilling these requirements, the pumped two-level quantum system has major shortcomings that make it impractical for immersion lithography. We will discuss these shortcomings in Section 3.5. In the next chapter, we will describe a system that avoids these shortcomings, and will also revise the requirements for using pumped atomic systems as immersion fluids.

3.1 Susceptibility spectrum near a resonance

We will now derive the susceptibility as a function of frequency near resonance using quantum mechanical language.[1] The calculations in this section do not take any broadening processes into account (apart from radiative broadening). In Section 3.3, we will take Doppler, collisional, and power broadening into account when calculating the susceptibility and refractive index as functions of frequency.

We will first introduce the density matrix, which we will use later to calculate the susceptibility. We assume the reader is familiar with bra-ket notation and has seen basic quantum mechanics.

3.1.1 Density matrix definition

We define the density matrix as $\rho = |\psi\rangle \langle\psi|$. The density matrix elements are found by evaluating

$$\rho_{ij} = \langle j | \rho | i \rangle . \tag{3.1}$$

To illustrate the process of calculating the density matrix, lets take the case of a two-level system as shown in Fig. 3-1. In this system, the population may be distributed in states $|a\rangle$ and $|b\rangle$. For the pure state $|\psi(t)\rangle = c_a(t)|a\rangle + c_b(t)|b\rangle$, the density matrix

[1] For a similar derivation with slightly different notation, the reader can consult Ref. [32].

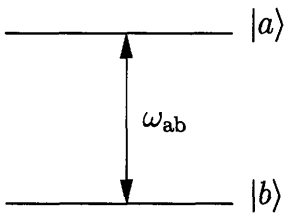

Figure 3-1: Energy level diagram of a two level system.

is given by

$$\rho = \begin{pmatrix} \rho_{aa} & \rho_{ab} \\ \rho_{ba} & \rho_{bb} \end{pmatrix} = \begin{pmatrix} c_a c_a^* & c_a c_b^* \\ c_b c_a^* & c_b c_b^* \end{pmatrix}. \tag{3.2}$$

The density matrix is useful because in many cases, we may not know the wavefunction $|\psi\rangle$ but we know the probabilities (i.e., $c_a c_a^*$, $c_b c_b^*$) that the system is in a particular state. If we couple the knowledge of the state of the system to how the system evolves with time, we can compute the susceptibility seen by a probe laser. We will now find a set of differential equations that describe the time evolution of the density matrix elements and relate their steady-state solution to the susceptibility.

3.1.2 Time evolution of the density matrix

The evolution of the density matrix with time $\dot{\rho}$ can be derived from the definition of the density matrix:

$$\begin{aligned} \dot{\rho} &= \frac{\partial}{\partial t}\left(|\psi\rangle\langle\psi|\right) \\ &= \left(\frac{\partial}{\partial t}|\psi\rangle\right)\langle\psi| + |\psi\rangle\left(\frac{\partial}{\partial t}\langle\psi|\right) \\ &= \frac{1}{i\hbar}\mathscr{H}|\psi\rangle\langle\psi| - \frac{1}{i\hbar}|\psi\rangle\langle\psi|\mathscr{H}^* \\ &= \frac{1}{i\hbar}[\mathscr{H}, \rho], \end{aligned} \tag{3.3}$$

where $\mathscr{H}$ is the Hamiltonian of the system and we have used the time-dependent Schrodinger equation

$$\mathscr{H}|\psi\rangle = i\hbar\frac{\partial}{\partial t}|\psi\rangle. \tag{3.4}$$

Equation (3.3) can be modified further with phenomenological terms that account for population decay from one state to another. This population decay can be in the form of radiative spontaneous emission, or non-radiative decay processes. We can also account for decay in coherence by adding decay rates that impact the off-diagonal matrix elements. The equation becomes

$$\dot{\rho} = \frac{1}{i\hbar}[\mathscr{H}, \rho] + \Gamma \tag{3.5}$$

where Γ is a matrix that contains constants corresponding to incoherent decay processes. Equation (3.5) is also known as the von-Neumann equation [32].

We will now solve this equation and relate its solution to the susceptibility and index of refraction of a pumped two-level system.

3.1.3 Defining the system parameters

A multiple-level quantum system is necessary for achieving steady-state population inversion. We will consider the simplest multiple-level quantum system: a two-level system that is pumped via a third, higher-energy state. We call this system a pumped two-level system to differentiate it from three-level systems that are used in EIT-based approaches, and because we can use any system for this scheme that can attain a population inversion.

A schematic of a pumped two-level system is shown in shown in Fig. 3-2(a). The schematic shows a probe excitation at probe frequency ν between ground state $|b\rangle$ and excited state $|c\rangle$, detuned by Δ. Additionally, an incoherent pump process at ω_{pump} transfers population from $|b\rangle$ to an upper lying state $|a\rangle$ at rate r_{ba}. Radiative decay processes between the various states are shown in Fig. 3-2(b). Γ_{ij} denotes the rate of decay between upper state $|i\rangle$ and lower state $|j\rangle$. The schematics does not show decoherence rates γ_{ij}, which correspond to decay rates for the off-diagonal terms of the density matrix.

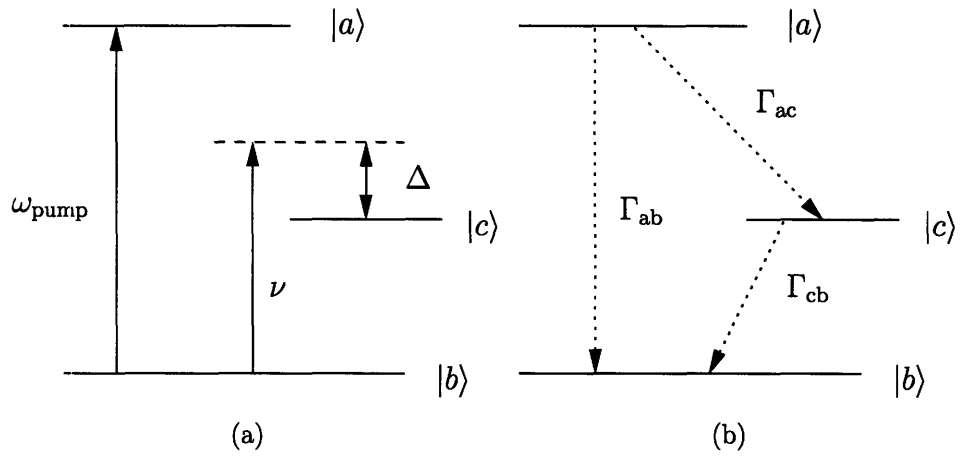

Figure 3-2: Energy level diagrams of a three level quantum system. **(a)** shows the driving field ν (probe) and ω_{pump} (pump). The probe field is detuned by Δ from the $|b\rangle - |a\rangle$ resonance. The pump can be incoherently driven. **(b)** shows the incoherent decay rates Γ_{ij} between the energy levels $|i\rangle$ and $|j\rangle$.

3.1.4 Formulating the equations of motion

To form the equations of motion for the density matrix elements, we use Eq. (3.5) along with the Hamiltonian $\mathscr{H}$ given by

$$\mathscr{H} = \begin{pmatrix} \hbar\omega_{\text{a}} & 0 & 0 \\ 0 & \hbar\omega_{\text{b}} & -(1/2)\hbar\Omega_{\text{R}}e^{i\nu t} \\ 0 & -(1/2)\hbar\Omega_{\text{R}}e^{-i\nu t} & \hbar\omega_{\text{c}} \end{pmatrix}, \tag{3.6}$$

where Ω_{R} is the Rabi frequency of the excitation that couples states $|b\rangle$ and $|c\rangle$, and the rotating wave approximation has been taken.[2] The pump enters the equations of motion through the Γ matrix, where in the form of a term that transfers population from the ground state $|b\rangle$ to the upper level $|a\rangle$ incoherently at rate r_{ba}. The nine

[2]Without the rotating wave approximation, the off-diagonal terms of the Hamiltonian would have both $e^{i\nu t}$ and $e^{-i\nu t}$ terms. If we carried out the calculation with the extra exponential term, we will get terms in the equations of motion that oscillate rapidly i.e. $\nu + (\omega_{\text{c}} - \omega_{\text{b}})$ and slowly i.e. $\nu - (\omega_{\text{c}} - \omega_{\text{b}})$. We have used the rotating wave approximation because we are only interested in the susceptibility near resonance, i.e. $\nu \approx (\omega_{\text{c}} - \omega_{\text{b}})$.

coupled equations of motion are given by:

$$\dot{\rho}_{aa} = -(\Gamma_{ab} + \Gamma_{ac})\rho_{aa} + r_{ba}\rho_{bb}, \tag{3.7}$$

$$\dot{\rho}_{ab} = -(\gamma_{ab} + i\omega_{ab})\rho_{ab} - \frac{i\Omega_R}{2}e^{-i\nu t}\rho_{ac}, \tag{3.8}$$

$$\dot{\rho}_{ac} = -\frac{i\Omega_R}{2}e^{i\nu t}\rho_{ab} - (\gamma_{ac} + i\omega_{ac})\rho_{ac}, \tag{3.9}$$

$$\dot{\rho}_{bb} = \Gamma_{ab}\rho_{aa} + \Gamma_{cb}\rho_{cc} - r_{ba}\rho_{bb} + \frac{i\Omega_R}{2}(e^{i\nu t}\rho_{cb} - e^{-i\nu t}\rho_{bc}), \tag{3.10}$$

$$\dot{\rho}_{bc} = \frac{i\Omega_R}{2}e^{i\nu t}(\rho_{cc} - \rho_{bb}) - (\gamma_{bc} - i\omega_{cb})\rho_{bc}, \tag{3.11}$$

$$\dot{\rho}_{cc} = \Gamma_{ac}\rho_{aa} - \Gamma_{cb}\rho_{cc} + \frac{i\Omega_R}{2}(e^{-i\nu t}\rho_{bc} - e^{i\nu t}\rho_{cb}), \tag{3.12}$$

$$\dot{\rho}_{ba} = \dot{\rho}^*_{ab}, \tag{3.13}$$

$$\dot{\rho}_{ca} = \dot{\rho}^*_{ac}, \tag{3.14}$$

$$\dot{\rho}_{cb} = \dot{\rho}^*_{bc}, \tag{3.15}$$

where Γ_{ij} is the rate of population decay from state $|i\rangle$ to $|j\rangle$, γ_{ij} is the decoherence rate for ρ_{ij} terms, and $\omega_{ij} = \omega_i - \omega_j$. It is assumed that $\gamma_{ij} = \gamma_{ji}$. Further simplifications are made via the substitutions

$$\begin{aligned} \rho_{bc} &= \tilde{\rho}_{bc}e^{i\nu t}, & \rho_{cb} &= \tilde{\rho}_{cb}e^{-i\nu t}, \\ \rho_{ba} &= \tilde{\rho}_{ba}e^{i\nu t}, & \rho_{ab} &= \tilde{\rho}_{ab}e^{-i\nu t}, \end{aligned} \tag{3.16}$$

and a conservation of population $\rho_{aa} + \rho_{bb} + \rho_{cc} = 1$ to result in the following system of first-order linear differential equations

$$\dot{\boldsymbol{\rho}} = \mathscr{M}\boldsymbol{\rho} + \mathscr{B}, \tag{3.17}$$

where

$$\boldsymbol{\rho} = \begin{pmatrix} \rho_{aa} \\ \tilde{\rho}_{ab} \\ \rho_{ac} \\ \tilde{\rho}_{ba} \\ \rho_{bb} \\ \tilde{\rho}_{bc} \\ \rho_{ca} \\ \tilde{\rho}_{cb} \end{pmatrix}, \tag{3.18}$$

and $\mathscr{M}$ and $\mathscr{B}$ are independent of time and are given by

$$\mathscr{M} = \begin{pmatrix} -\Gamma_{ab} - \Gamma_{ac} & 0 & 0 & 0 & r_{ba} & 0 & 0 & 0 \\ 0 & -\gamma_{ab} + i(\Delta - \omega_{ac}) & -i\Omega_R/2 & 0 & 0 & 0 & 0 & 0 \\ 0 & -i\Omega_R/2 & -\gamma_{ac} - i\omega_{ac} & 0 & 0 & 0 & 0 & 0 \\ 0 & 0 & 0 & -\gamma_{ab} - i(\Delta - \omega_{ac}) & 0 & 0 & i\Omega_R/2 & 0 \\ \Gamma_{ab} - \Gamma_{cb} & 0 & 0 & 0 & -r_{ba} - \Gamma_{cb} & -i\Omega_R/2 & 0 & i\Omega_R/2 \\ -i\Omega_R/2 & 0 & 0 & 0 & -i\Omega_R & -\gamma_{bc} - i\Delta & 0 & 0 \\ 0 & 0 & 0 & i\Omega_R/2 & 0 & 0 & -\gamma_{ac} + i\omega_{ac} & 0 \\ i\Omega_R/2 & 0 & 0 & 0 & i\Omega_R & 0 & 0 & i\Delta - \gamma_{bc} \end{pmatrix}, \tag{3.19}$$

$$\mathscr{B} = \begin{pmatrix} 0 \\ 0 \\ 0 \\ 0 \\ \Gamma_{cb} \\ i\Omega_R/2 \\ 0 \\ -i\Omega_R/2 \end{pmatrix}, \tag{3.20}$$

where we have made use of $\Delta = \nu - \omega_{cb}$. The steady state solution, $\boldsymbol{\rho}_{ss}$ is given by

$$\boldsymbol{\rho}_{ss} = -\mathscr{M}^{-1}\mathscr{B}. \tag{3.21}$$

To first order in Ω_R (we will explore higher order solutions later), the non-zero steady state analytical solutions near resonance are

$$\rho_{aa} = \frac{r_{ba}\Gamma_{cb}}{r_{ba}\Gamma_{cb} + \Gamma_{ab}\Gamma_{cb} + \Gamma_{ac}(r_{ba} + \Gamma_{cb})}, \tag{3.22}$$

$$\rho_{bb} = \frac{(\Gamma_{ab} + \Gamma_{ac})\Gamma_{cb}}{r_{ba}\Gamma_{cb} + \Gamma_{ab}\Gamma_{cb} + \Gamma_{ac}(r_{ba} + \Gamma_{cb})}, \tag{3.23}$$

$$\tilde{\rho}_{cb} = \frac{\Omega_R}{2}\frac{1}{\Delta + i\gamma_{bc}}\frac{\Gamma_{ac}(r_{ba} - \Gamma_{cb}) - \Gamma_{ab}\Gamma_{cb}}{r_{ba}\Gamma_{cb} + \Gamma_{ab}\Gamma_{cb} + \Gamma_{ac}(r_{ba} + \Gamma_{cb})}, \tag{3.24}$$

$$= \frac{\Omega_R}{2}\frac{1}{\Delta + i\gamma_{bc}}(\rho_{cc} - \rho_{bb}), \tag{3.25}$$

$$\tilde{\rho}_{bc} = \tilde{\rho}^*_{cb}, \tag{3.26}$$

$$\rho_{cc} = 1 - \rho_{aa} - \rho_{bb}. \tag{3.27}$$

3.1.5 Relating the density matrix elements to susceptibility

We will now relate the steady-state solutions to the equations of motion to the susceptibility χ through the polarization. Polarization, P is related to the off-diagonal density matrix elements via

$$P = N\sum_{\alpha,\beta}\mu_{\beta\alpha}\rho_{\alpha\beta}, \tag{3.28}$$

where $|\alpha\rangle$ and $|\beta\rangle$ are distinct eigenstates of the unperturbed system (where $\Omega_R = 0$, N is the atomic density, and $\mu_{\beta\alpha}$ is the dipole matrix element defined as $e\langle\beta|\vec{r}|\alpha\rangle$, where e is the electronic charge. For the three-level system in consideration, the polarization is

$$P = N\mu_{bc}\rho_{cb} \tag{3.29}$$

$$= N\mu_{bc}\tilde{\rho}_{cb}e^{-i\nu t} \tag{3.30}$$

The polarization is also related to the electric field via

$$P = \epsilon_0\chi E, \tag{3.31}$$

where E is given by

$$E = \frac{E_0}{2} e^{-i\nu t}. \tag{3.32}$$

We can now combine Eqs. (3.30), (3.31), and (3.32) to obtain

$$\chi = \frac{2\mu_{bc}}{\epsilon_0 E_0} \tilde{\rho}_{cb}, \tag{3.33}$$

which becomes

$$\chi = 2N\Gamma_{cb} \frac{3}{8\pi^2} \lambda_{cb}^3 \frac{\tilde{\rho}_{cb}}{\Omega_R}, \tag{3.34}$$

with the use of the relations $\Omega_R = \mu_{bc} E_0/\hbar$ and $\Gamma_{cb} = \mu_{bc}^2 \omega_{cb}^3/(3\pi\epsilon_0 \hbar c^3)$ [37, 38]. We can then combine Eqs. (3.25) and (3.34) to obtain

$$\chi = N\Gamma_{cb} \frac{3}{8\pi^2} \lambda^3 \frac{1}{\Delta + i\gamma_{bc}} (\rho_{cc} - \rho_{bb}) \tag{3.35}$$

where

$$\rho_{cc} - \rho_{bb} = \frac{\Gamma_{ac}(r_{ba} - \Gamma_{cb}) - \Gamma_{ab}\Gamma_{cb}}{r_{ba}\Gamma_{cb} + \Gamma_{ab}\Gamma_{cb} + \Gamma_{ac}(r_{ba} + \Gamma_{cb})} \tag{3.36}$$

is the difference between the excited state and ground state populations that depends only on physical parameters and incoherent pump rate r_{ba}.

3.2 Visualizing the solution using parameters from atomic calcium

In order to see how large the refractive index can get, we need to use parameters from a real quantum system. We will use parameters associated with the 4^1S to 4^1P transition in atomic calcium, because the parameters are typical for atomic systems and are readily available [37]. The parameters and other assumed values as summarized in Table 3.1.

Table 3.1: Parameters relating to atomic calcium vapor. These parameters are used for Figs. 3-3 to 3-7 except as noted otherwise.

Parameter	Value	Units
Wavelength of 4^1S to 4^1P transition, λ_{cb}	422.7	nm
Radiative lifetime, Γ_{cb}	2.2×10^8	s^{-1}
Decoherence rate, γ_{bc}	$\Gamma_{cb}/2$	
Atomic density, N (typical)	10^{16}	atoms/cm^3

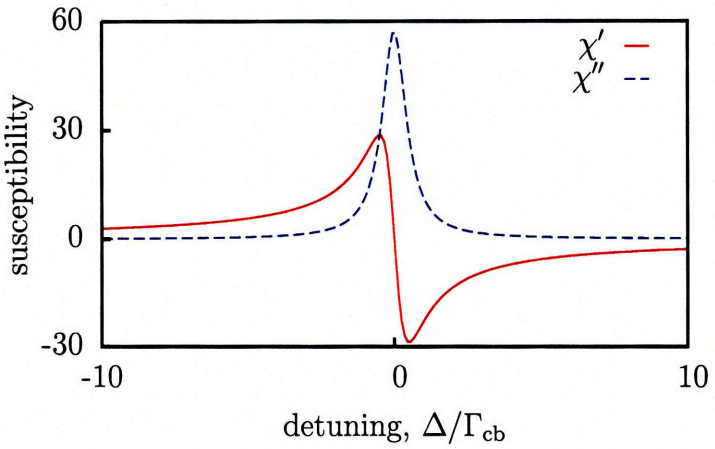

Figure 3-3: Dependence of the real (χ') and imaginary (χ'') parts of susceptibility on probe detuning Δ in the case where the steady state population is in the ground state. In this case, probe light near resonance gets absorbed.

3.2.1 Dependence of susceptibility on probe frequency detuning

We will plot the dependence of real (χ') and imaginary (χ'') parts of susceptibility on the probe frequency detuning for two different cases. Figure 3-3 shows the dependence of χ' and χ'' on Δ for $\rho_{cc} - \rho_{bb} = -1$ (all steady-state population in the ground state). Clearly, the susceptibility spectrum in Fig. 3-3 is identical to that in Fig. 2-3. On the other hand, Fig. 3-4 shows a different dependence for $\rho_{cc} - \rho_{bb} = 1$ (all steady-state population in the excited state), where absorption has been replaced with amplification due to stimulated emission.

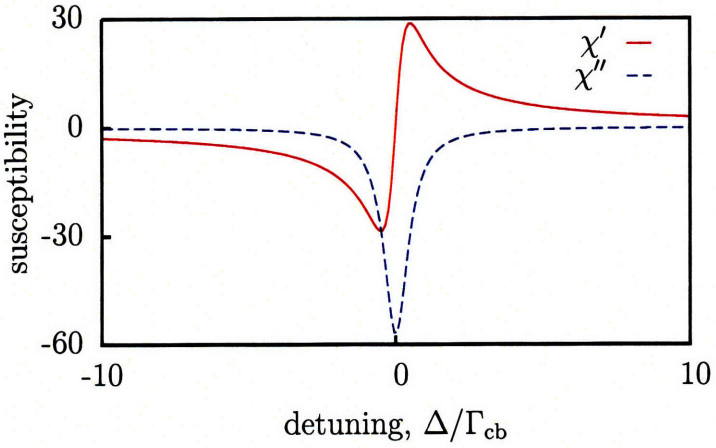

Figure 3-4: Dependence of the real (χ') and imaginary (χ'') parts of susceptibility on probe detuning Δ in the case where the steady state population is in the excited state. In this case, we have population inversion and thus, amplification instead of absorption near resonance.

3.2.2 Dependence of index of refraction on probe frequency detuning

We can calculate the refractive index from the susceptibility by making use of the relation

$$n = \sqrt{1+\chi}. \tag{3.37}$$

We define the complex refractive index through $n = n' + in''$, where n' is the refractive index, while n'' is the absorption coefficient of the medium. If $n'' > 0$ we have absorption, but if if $n'' < 0$ then we have amplification of the probe. We arrive at the following expressions relating the real and imaginary parts of n to those of susceptibility [32]:

$$n' = \left[\frac{\sqrt{(1+\chi')^2+\chi''^2}+(1+\chi')}{2}\right]^{1/2} \tag{3.38}$$

$$n'' = \left[\frac{\sqrt{(1+\chi')^2+\chi''^2}-(1+\chi')}{2}\right]^{1/2} \mathrm{sgn}(\chi'') \tag{3.39}$$

Figure 3-5 shows the dependence of the refractive index and absorption coefficient on the detuning of the probe frequency from resonance for the case where the

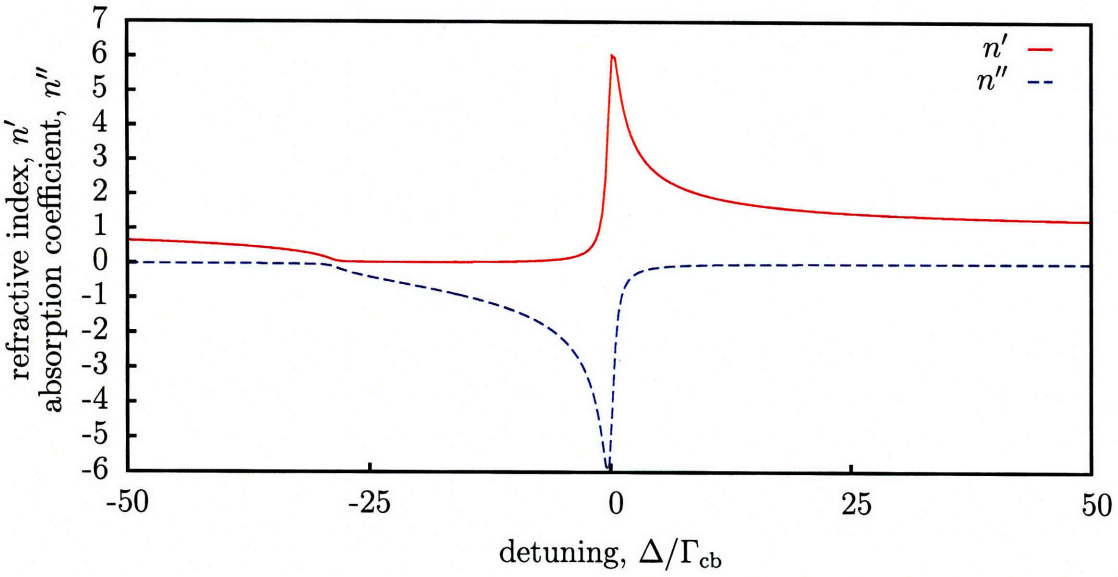

Figure 3-5: Plot of the refractive index (n') and gain/absorption coefficient (n'') as a function of probe detuning from resonance Δ.

population is completely in the excited state ($\rho_{cc} - \rho_{bb} = 1$). The plot is asymmetric because of the nonlinearities that are introduced by Equations (3.38) and (3.39). One interesting feature of this plot is that an index of refraction less than 1 can be achieved with amplification at a frequency to the left of $\Delta = 0$. However, the key point of interest in this plot is an ultrahigh refractive index (~ 6) with gain. We will now examine how increasing the atomic density results in an even higher refractive index.

3.2.3 Dependence of the index of refraction on atomic density

The refractive index depends strongly on the atomic density of the medium. This dependence is shown in Figure 3-6 for the case where the steady-state population is in the excited state ($\rho_{cc} - \rho_{bb} = 1$). We find that n' is proportional to $\sqrt{N}$ above an atomic density of $\sim 10^{14}$, therefore an order of magnitude increase in atomic density yields a factor of ~ 3 increase for the index.

We will now explore the conditions for achieving a steady-state population inversion (i.e. $\rho_{cc} - \rho_{bb} > 0$).

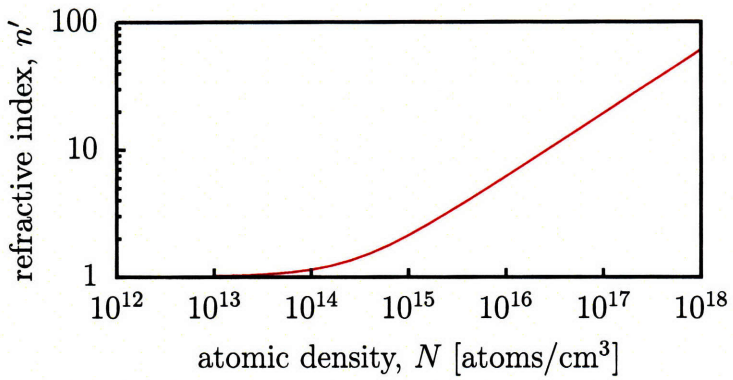

Figure 3-6: Plot of the maximum value of refractive index (with respect to detuning) as a function of the atomic density N.

3.2.4 Dependence of population difference on incoherent pump rate

A population inversion in the atomic system allows us to replace absorption with gain. The population can be inverted by using a pump source that is incoherent, e.g., a lamp. However, the pump rate has to be above a certain amount to induce population inversion. By manipulating Equation (3.36), we can deduce that population can be inverted for values of the incoherent pump rate given by

$$r_{ba} > \Gamma_{cb} + \frac{\Gamma_{ab}\Gamma_{cb}}{\Gamma_{ac}}, \tag{3.40}$$

and that the asymptotic value for the population difference for large values of r_{ba} is given by

$$(\rho_{cc} - \rho_{bb})_{max} = \frac{1}{1 + \frac{\Gamma_{ab}}{\Gamma_{ac}}} \tag{3.41}$$

$$\approx 1 \quad \text{for } \Gamma_{ac} \gg \Gamma_{ab} \tag{3.42}$$

Therefore, fast decay for the $|a\rangle$ to $|c\rangle$ and a long lifetime for the $|c\rangle$ to $|b\rangle$ transition are required to control the population difference between ground state $|b\rangle$ and excited state $|c\rangle$ to any value between -1 and 1. Figure 3-7 illustrates the need for fast decay in order to achieve $\rho_{cc} - \rho_{bb} = 1$. In this Figure, we have used $\Gamma_{cb} = \Gamma_{ab} = \Gamma_{slow}$

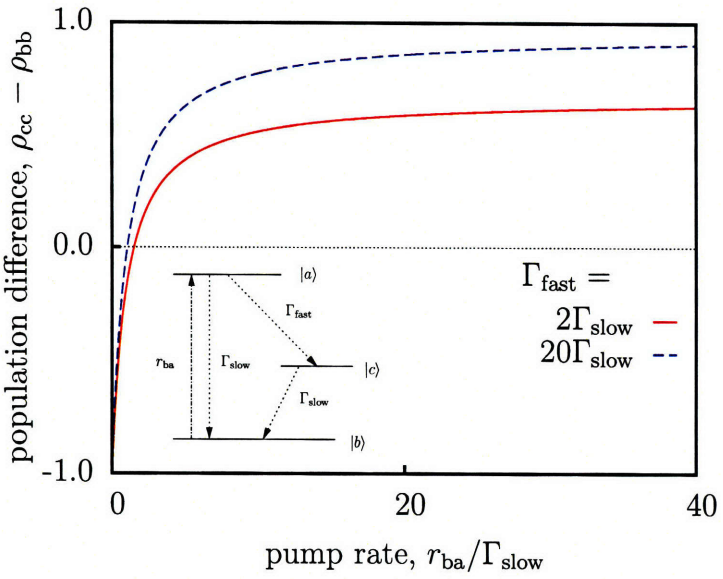

Figure 3-7: Plot showing the dependence of the population difference on the incoherent pump rate, (r_{ba}). $\rho_{cc} - \rho_{bb}$ approaches an asymptotic value of $1/(1 + \Gamma_{slow}/\Gamma_{fast})$ for large r_{ba}. We have used $\Gamma_{cb} = \Gamma_{ab} = \Gamma_{slow}$ and $\Gamma_{ac} = \Gamma_{fast}$ as shown in the inset.

and $\Gamma_{ac} = \Gamma_{fast} = m\Gamma_{slow}$. We will now examine how broadening effects impact the refractive index.

3.3 Including broadening effects

The frequency dependence of the absorption of an atomic medium is known as its lineshape function. The effect of increasing the width of the lineshape function is known as broadening. For example, an atom that undergoes spontaneous emission, the lineshape is broadened from an impulse (the shape if spontaneous emission is not taken into account) into a lineshape function known as a Lorentzian. A Lorentzian differs from a Gaussian in that a Lorentzian function has a larger tail and is less sharply peaked. The broadening due to spontaneous emission is known as radiative broadening, while the resulting lineshape function has a width (usually the full-width at half-maximum) known as the natural linewidth.

However, there are other broadening processes that we have not considered that decrease the peak refractive index obtainable by our scheme. In this section, we will

examine Doppler, power, and collision broadening and see how temperature, atomic density, and probe intensity impact the refractive index. We will now describe the mechanisms for these broadening effects and see how they are incorporated into our model. Later, we will again use parameters from atomic calcium to gage the effect of these broadening mechanisms.

3.3.1 Power broadening

In Section 3.1.4, the solution to the equation of motion of the density matrix elements was taken to first order in the probe Rabi frequency Ω_R. We can make this first-order approximation if we assume that the probe intensity is small. The first order expression is reproduced in the following equation, where the superscripts on the density matrix elements denote their order in Ω_R:

$$\tilde{\rho}_{cb}^{(1)} = \frac{\Omega_R}{2}\frac{1}{\Delta + i\gamma_{bc}}\frac{\Gamma_{ac}(r_{ba} - \Gamma_{cb}) - \Gamma_{ab}\Gamma_{cb}}{r_{ba}\Gamma_{cb} + \Gamma_{ab}\Gamma_{cb} + \Gamma_{ac}(r_{ba} + \Gamma_{cb})} \tag{3.43}$$

$$= \frac{\Omega_R}{2}\frac{\Delta - i\gamma_{bc}}{\Delta^2 + \gamma_{bc}^2}\left(\rho_{cc}^{(1)} - \rho_{bb}^{(1)}\right). \tag{3.44}$$

If we do not assume that the probe is weak, then we need to retain solutions to the equation of motion to all orders in Ω_R. The solution for the off-diagonal density matrix element ρ_{cb} is then given by

$$\tilde{\rho}_{cb}^{(\infty)} = \frac{\Omega_R}{2}\frac{(\Delta - i\gamma_{bc})\big(\Gamma_{ac}(r_{ba} - \Gamma_{cb}) - \Gamma_{ab}\Gamma_{cb}\big)}{(\Delta^2 + \gamma_{bc}^2)\big(r_{ba}\Gamma_{cb} + \Gamma_{ab}\Gamma_{cb} + \Gamma_{ac}(r_{ba} + \Gamma_{cb})\big) + (\Omega_R^2/2)\gamma_{bc}(r_{ba} + 2\Gamma_{ab} + 2\Gamma_{ac})}. \tag{3.45}$$

It turns out that the expression relating the coherence to the populations still holds (compare Eqs. (3.44) and (3.46)):

$$\tilde{\rho}_{cb}^{(\infty)} = \frac{\Omega_R}{2}\frac{\Delta - i\gamma_{bc}}{\Delta^2 + \gamma_{bc}^2}\left(\rho_{cc}^{(\infty)} - \rho_{bb}^{(\infty)}\right). \tag{3.46}$$

To find the contribution of power broadening on the linewidth, we can rearrange

Eq. (3.45) as follows:

$$\tilde{\rho}_{cb}^{(\infty)} = \frac{\Omega_R}{2}\left(\frac{\Gamma_{ac}(r_{ba}-\Gamma_{cb})-\Gamma_{ab}\Gamma_{cb}}{r_{ba}\Gamma_{cb}+\Gamma_{ab}\Gamma_{cb}+\Gamma_{ac}(r_{ba}+\Gamma_{cb})}\right)\frac{\Delta-i\gamma_{bc}}{\Delta^2+\gamma_{nat,pow}^2} \tag{3.47}$$

where the natural linewidth has increased from $2\gamma_{bc}$ to

$$2\gamma_{nat,pow} = 2\left(\gamma_{bc}^2+\frac{\Omega_R^2}{2}\frac{\gamma_{bc}(r_{ba}+2\Gamma_{ab}+2\Gamma_{ac})}{r_{ba}\Gamma_{cb}+\Gamma_{ab}\Gamma_{cb}+\Gamma_{ac}(r_{ba}+\Gamma_{cb})}\right)^{1/2}. \tag{3.48}$$

Clearly, as one increases probe intensity, the Rabi frequency and the linewidth increase, which ultimately reduces the value of $\tilde{\rho}_{cb}$, and consequently, χ' and n'. In the plots to follow, we will use (3.48) with the relation

$$\Omega_R = \frac{\mu_{bc}}{\hbar}\sqrt{2\frac{\frac{I_0}{10}}{c\epsilon_0}} \tag{3.49}$$

where the probe laser intensity I_0 is in units of $\mathrm{mW/cm^2}$ and μ_{bc} is the dipole matrix element for the probe transition.

3.3.2 Collision broadening

Collision broadening is attributed to a change in the phase of atomic wavefunctions resulting from elastic collisions. This effect is taken into account with an extra decay term in the equations of motion for the off-diagonal matrix element ρ_{cb}. The decay rate is given by [39]:

$$\gamma_{coll} = 1/\tau_0, \tag{3.50}$$

$$= 4d_{ctrs}^2 N\left(\frac{\pi k_B T}{M}\right)^{1/2}, \tag{3.51}$$

where τ_0 is the mean period of free flight, d_{ctrs} is the distance between the centers of the atoms during a collision, N is the atomic density, k_B is the Boltzmann contant, and T is the temperature.

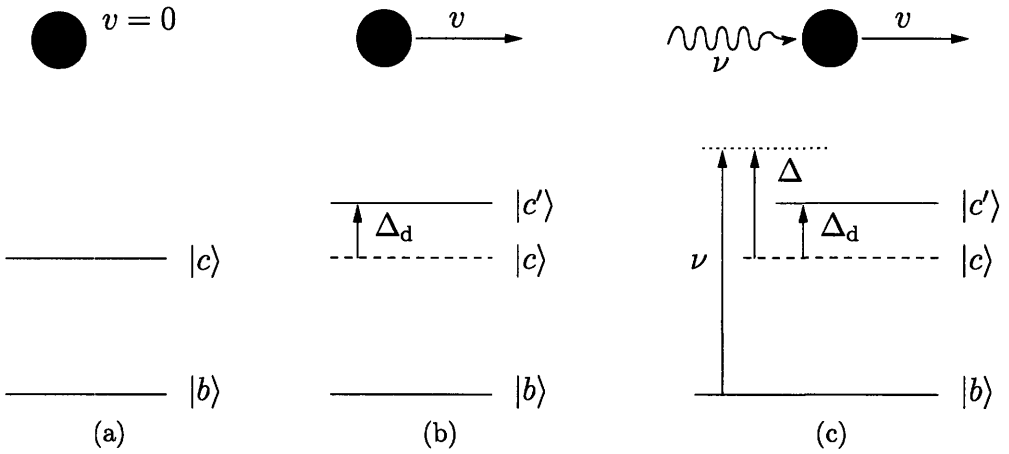

Figure 3-8: Schematic of the relationship between an incoming photon and energy level structure of a two level atom when the Doppler effect is taken into account. **(a)** shows an atom at rest and corresponding energy level structure with ground state $|b\rangle$ and excited state $|c\rangle$. **(b)** shows an atom with velocity v with an energy level structure that is modified from the rest atom. Effectively, the atom has a new excited state $|c'\rangle$ that is detuned by Δ_d from the original excited state $|c\rangle$. **(c)** shows the same atom as in (b) now interacting with a photon with frequency ν detuned from the original excited state energy by Δ.

3.3.3 Doppler broadening

To illustrate the Doppler effect, we take the case of an incoming photon that is exactly on resonance with an atomic transition for an atom at rest (we neglect all other broadening effects). A moving atom will "see" this photon with a different frequency than that of the atom at rest, thus will not absorb it. Only when a photon is appropriately detuned will it be absorbed by the moving atom. This effect is illustrated in Fig. 3-8.

The overall effect of Doppler broadening, however, lends itself to a spread in velocities in an atomic system and taking into account other broadening processes that impose a frequency dependence on the absorption. An atom with a velocity v, as shown in Figure 3-8(b), can be thought to experience an energy shift, denoted by detuning Δ_d, in the energy level of its excited state when at rest, $|c\rangle$ to a Doppler-shifted excited state $|c'\rangle$. From energy and momentum conservation [39], we find that

the detuning, Δ_d is related to the velocity v via:

$$\Delta_d \approx \frac{v}{c}\omega_{cb} = \frac{2\pi}{\lambda_{cb}}v. \tag{3.52}$$

Thus for a gas with a Maxwellian distribution in velocity given by

$$F_G(v) = \frac{1}{\sqrt{\pi}\left(\frac{2k_BT}{M}\right)} \exp\left(\frac{-v^2}{\left(\frac{2k_BT}{M}\right)}\right), \tag{3.53}$$

the distribution of the excited state energy as a function of the detuning Δ_d is

$$F(\Delta_d) = \frac{1}{\sqrt{\pi\delta_d^2}} \exp\left(\frac{-\Delta_d^2}{\delta_d^2}\right) \tag{3.54}$$

where the Doppler width, δ_d is given by

$$\delta_d = \frac{2\pi}{\lambda_{cb}}\sqrt{\frac{2k_BT}{M}}. \tag{3.55}$$

Now when photons with frequency ν (see Figure 3-8(c)) interact with the ensemble of atoms, we need to take into account the difference between detuning of each atom due to the Doppler shift, Δ_d and the detuning of the photon, Δ. To compute the broadened value of $\tilde{\rho}_{cb}$ at a particular detuning Δ, we compute the integral

$$\tilde{\rho}_{cb}^{(dopp)}(\Delta) = \int_{-\infty}^{\infty} \tilde{\rho}_{cb}(\Delta_d)F(\Delta - \Delta_d)\ (d\Delta_d). \tag{3.56}$$

Incidentally, Eq. (3.56) is the convolution between the Gaussian lineshape function for Doppler broadening F, and the off-diagonal matrix element $\tilde{\rho}_{cb}$.

3.4 Visualizing the impact of broadening on the refractive index of atomic calcium

To see the effect of Doppler, collision, and power broadening on the index of refraction of atomic calcium, we will again use parameters for the 4^1S to 4^1P transition in Ca,

Table 3.2: General parameters for Figures 3-9 to 3-13 (except as noted otherwise)

Parameter	Value	Units
Wavelength of 4^1S to 4^1P transition [37], λ_{cb}	422.7	nm
Radiative lifetime [37], Γ_{cb}	2.2×10^8	s^{-1}
Decoherence rate, γ_{bc}	$\Gamma_{cb}/2$	
Atomic density, N	10^{16}	atoms/cm^3
Probe laser intensity, I_0	1	mW/cm^2
Temperature, T	298	K
Atomic mass, M	$40.078 \times 1.6605 \times 10^{-27}$	kg
Distance between centers of atoms during collision, d_{ctrs}	$2 \times 1.8 \times 10^{-10}$	m
Decay rate for $\|a\rangle \rightarrow \|b\rangle$, Γ_{ab}	$0.1\Gamma_{cb}$	
Decay rate for $\|a\rangle \rightarrow \|c\rangle$, Γ_{ac}	$10\Gamma_{cb}$	
Incoherent pump rate for $\|b\rangle \rightarrow \|a\rangle$, r_{ba}	$200\Gamma_{cb}$	

obtained from Ref. [37]. The parameters are listed in Table 3.2 along with other parameters relating to broadening effects.

3.4.1 Dependence of Doppler and collision linewidths on temperature

It is useful to see which broadening mechanism is the dominant one. One way to do this is to compare the broadening linewidths. In Fig. 3-9 we have plotted the linewidths associated with Doppler and collision broadening. While we are not comparing exactly the same metrics in this plot (see the definitions of $\delta_d$and γ_{coll}in the last section), we believe that the comparison should hold to within an order of magnitude. Figure 3-9 shows that Doppler broadening dominates for low atomic densities, but collision broadening becomes relevant as the density approaches $\sim 10^{19}$ atoms/cm^3. Therefore, for an atomic density of 10^{16} atoms/cm^3, we expect Doppler broadening to dominate over collision broadening.

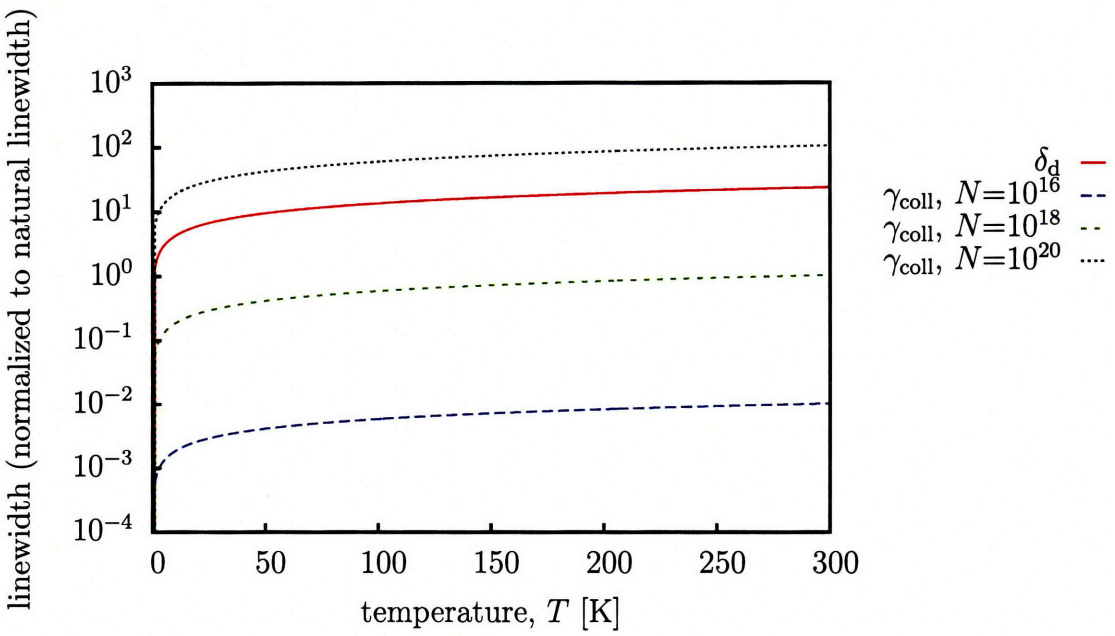

Figure 3-9: Plot of the half-linewidths associated with Doppler broadening (δ_d) and collision broadening (δ_{coll}) as a function of temperature. The collision half-linewidth is plotted for various atomic densities. Doppler broadening dominates over collision broadening for low values of the atomic density.

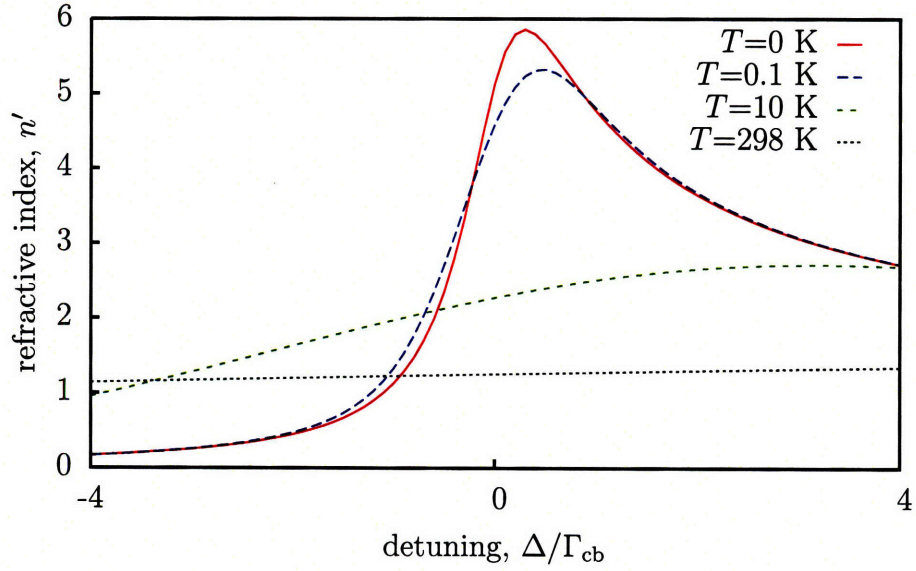

Figure 3-10: Plot of the refractive index n' as a function of probe detuning as a function of temperature for a pumped system with the steady-state population completely in the excited state ($\rho_{cc} - \rho_{bb} = 1$).

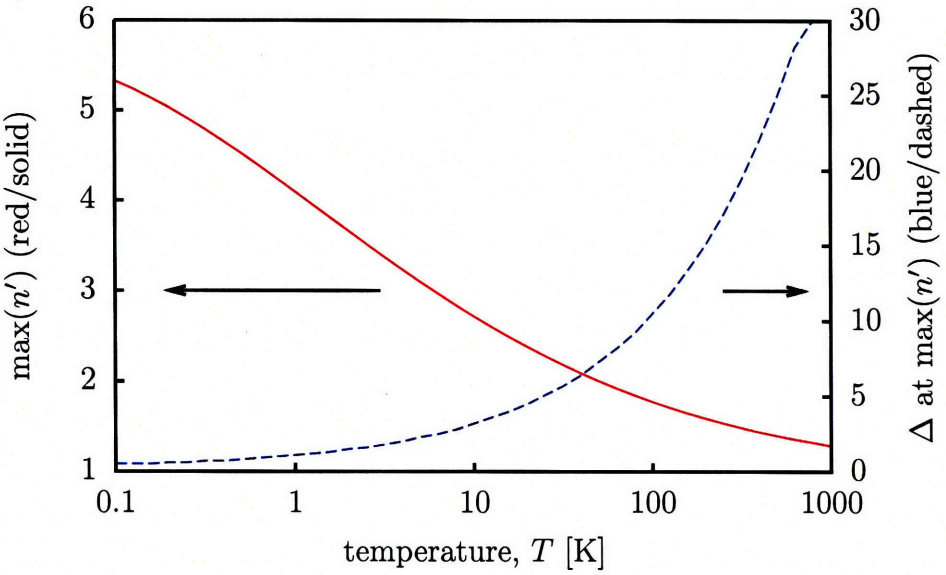

Figure 3-11: Plot of the maximum refractive index $\max(n')$ as a function of the temperature of an atomic system with population inversion. On the right axis, the value of the detuning at which the maximum index is attainable is plotted as a function of temperature.

3.4.2 Dependence of refractive index on temperature

Doppler broadening has a large effect on lowering the index of refraction for temperatures even as low as 10K. Figure 3-10 shows the real part of the refractive index, n', as a function of detuning Δ for various temperatures. This plot shows that as we increase the temperature, the lineshape function of n' becomes broader. Another feature of this plot is that the maximum value for n' occurs at larger values of the detuning as T increases. This effect is also illustrated in Fig. 3-11, where the maximum value, $\max(n')$ and Δ at $\max(n')$ are plotted as functions of temperature. This plot shows that the system will need to be cooled to counter broadening effects and achieve large values for the refractive index for an atomic density of $N = 10^{16}$ atoms/cm^3. The next section shows how atomic density can be increased to achieve a high refractive index even with broadening effects.

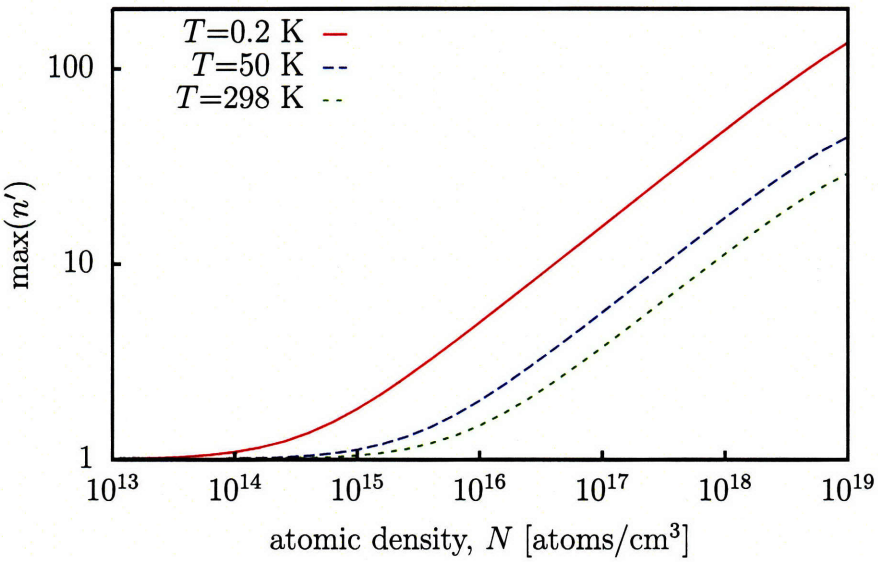

Figure 3-12: Plot of the maximum value of the refractive index, $\max(n')$ as a function of the atomic density for various temperatures. This plot shows that one can attain a large value for the refractive index at elevated temperatures by increasing the atomic density.

3.4.3 Dependence of the refractive index on atomic density

Increasing the atomic density offers a way to increase the refractive index even with the inclusion of broadening effects. Figure 3-12 shows that an increase of an order of magnitude in the atomic density yields more than a three-fold increase in the index of refraction. However, achieving population inversion in systems with high densities will require more pump power.

3.4.4 Dependence of the refractive index on probe intensity

Power broadening has a strong impact on the refractive index. Figure 3-13 shows the dependence of the probe intensity on the refractive index for an infinitesimally thin slab of medium. This plot shows that the probe intensity is the dominant broadening process when the intensity is on the order of $\sim 10^5$ mW/cm^2. This broadening mechanism turns out to be the Achilles' heel of our scheme, as we describe in the following section.

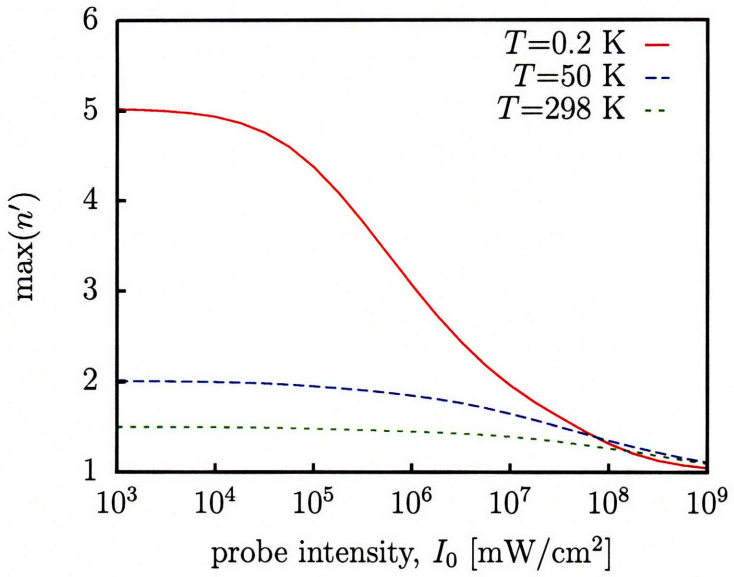

Figure 3-13: Plot of the maximum value of the refractive index, $\max(n')$ as a function of probe intensity for various temperatures.

3.5 The problem with amplification

At first glance, it seems simple to avoid the effects of power broadening: simply use a probe that is weak. However, high gain leads to probe beam intensities that are high enough for power broadening to make a difference. Coupled with this fact is that the amplifying probe beam quenches more of the pumped atoms as it propagates, which leads to a reduction of $(\rho_{cc} - \rho_{bb})$ in Eq. (3.35) and consequently reduces the refractive index as well. As a result, after only micrometers of propagation, the refractive index seen by the probe is reduced to 1. Details of this calculation were performed jointly with Magnus Rådmark and are given in Ref. [34]. The net result is a negative one; we cannot use this system for immersion lithography because amplification will cause a reduction in the refractive index.

There is another reason that this system cannot be used for immersion lithography: amplified spontaneous emission (ASE). ASE is a problem endemic to many optical systems, including erbium-doped fiber amplifiers (EDFAs) [40], and master oscillator power amplifiers (MOPA) [41]. In a simulation conducted in collaboration with M. Rådmark, we found that spontaneous emission was amplified by a factor of ~ 100 in a propagation distance of only $1\,\mu$m [34]. This amount of amplification is

undesirable for two reasons. First, an atom that has undergone stimulated emission from a spontaneous emission photon is unavailable for emission stimulated by a probe-beam photon, thus the population inversion is reduced, leading to a reduction in the refractive index of the medium. Second, a large amount of noise from spontaneous emission reduces the image contrast in an immersion lithography application.

3.6 Conclusion

In this chapter, we have explored a scheme that uses a pumped two-level quantum system to achieve a large refractive index without absorption. Because there is population inversion in the two-level system, the absorption is replaced with amplification. Amplification results in a few problems that make this system unattractive for implementing as an immersion fluid for optical lithography. Ideally, we need a quantum system that mitigates both ASE and power-broadening issues.

In the next chapter, we will explore a system that promises a solution to both of these problems by replacing the amplification with transparency. In addition, the scheme we will propose can achieve $d\chi'/d\omega \ll 0$, $d\chi'/d\omega \gg 0$, and $\chi' \ll 0$ in addition to $\chi' \gg 0$ all with transparency ($\chi'' = 0$).

We will briefly mention other issues that need to be resolved before a pumped quantum system can be used for immersion lithography. One issue concerns the depth into the atomic media that a pump beam can penetrate and maintain population inversion. This issue is addressed in Appendix A. Other issues include spatial intensity variations of the probe and pump beams due to inhomogeneity in the atomic density, and countering high (or total) reflectivity at lens/atomic medium interface. These issues are not addressed in this thesis but will need to be resolved to enable an atomic medium to be used as an immersion fluid.

Chapter 4

Controlling the optical properties of media using a mixture of active and passive resonances

In this chapter, we will present a unified approach to engineering the refractive index of optical materials by using mixtures of active and passive optical materials at frequencies near their resonances. Our approach does not depend on quantum coherence and can realize large and small (much less than 1) indices of refraction and negative permittivity ($\epsilon < 0$), normal and anomalous dispersion, all while maintaining transparency. Transparency allows us to avoid problems of amplified spontaneous emission and power broadening, both of which were problems of the scheme presented in the previous chapter.

4.1 Introduction

In recent years, the accepted wisdom regarding limitations of the optical properties of materials has been challenged. Electromagnetically induced transparency (EIT) can render an otherwise opaque medium transparent to electromagnetic radiation using quantum interference [31]. Light can be sped up to superluminal group velocities, slowed down, or even stopped [10, 12–14, 42]. While early demonstrations relied on

systems exhibiting quantum coherence, consequently reducing their practicality, these desirable optical properties have also been proposed and achieved by schemes that either do not require quantum coherence or rely only on classical optical phenomena [11, 28, 43–46].

Many applications require low optical losses or, ideally, optical transparency. However, achieving optical transparency in schemes such as those in Refs. [11, 28, 43–46] is problematic because these schemes rely on the optical properties of resonant media. On its own, a classical resonant medium can exhibit large or small susceptibility (χ) or a large change in χ with respect to frequency [32], albeit accompanied by strong absorption that masks these desirable optical phenomena. The same optical properties are achievable using an active resonance that results, for example, when population inversion is achieved in a laser gain material or a excited atomic gas [39]. As we have seen in the previous chapter, the strong amplification that accompanies an active resonance can be as problematic as strong absorption [34]. Recent experiments have used gain or loss doublets as an attempt to mitigate these problems of loss and gain [11, 45]. Two papers in the literature note that by mixing two materials, one passive and the other active, enhanced index [28] and negative index [47] can be realized in truly transparent systems. But these results were not applied more generally to demonstrate the wide variety of effects discussed above.

In this chapter, we will describe a conceptual framework that uses mixtures of active and passive resonances to realize a host of novel optical phenomena without quantum coherence and with transparency. This framework is independent of the specific physical realization (nonlinear optics, atomic gas, solid-state, or combinations) allowing for new physical proposals. We show how to control the amplitudes, widths, and resonant frequencies in order to reproduce in new physical systems a variety of *lossless* optical phenomena including normal dispersion ($d\chi/d\omega \gg 0$, identical to EIT-related schemes [10, 31]), anomalous dispersion ($d\chi/d\omega \ll 0$), negative permittivity ($\epsilon = 1 + \chi < 0$), and large refractive index ($n = \sqrt{\chi^2 + 1} \gg 1$).

We will first present the central concept in more detail. We will then identify the specific optical phenomena that our scheme can realize, and finally present a possible

physical system in which to implement this scheme.

4.2 Description of central concept

Consider the susceptibility of a medium described by a generic (e.g. two-level atomic) resonance at frequency ω_0:

$$\chi(\omega; A, \omega_0, \Gamma) = \frac{A(\Gamma/2)}{(\omega_0 - \omega) - i(\Gamma/2)} \tag{4.1}$$

where ω is the probe frequency, Γ is the linewidth, and A is the amplitude; $A > 0$ ($A < 0$) for a passive (active) resonance. Susceptibility, which relates the electric field to the polarization of the medium, is a complex quantity $\chi = \chi' + i\chi''$, where $\chi'' > 0$ ($\chi'' < 0$) corresponds to absorption (amplification). Figure 4-1(a) shows the real and imaginary parts of the susceptibility for a passive resonance $\chi(A, \omega_\mathrm{p}, \Gamma)$, while Fig. 4-1(b) shows an active resonance $\chi(-A, \omega_\mathrm{a}, \Gamma)$. Note that desirable optical characteristics in these spectra (e.g. $\chi' > 0$, $\chi' < 0$, $\mathrm{d}\chi'/\mathrm{d}\omega > 0$, and $\mathrm{d}\chi'/\mathrm{d}\omega < 0$) are masked by the strong absorption shown in Fig. 4-1(a) and amplification in Fig. 4-1(b).

Now consider an incoherent mixture of two optical resonances: one active and the other passive, accompanied by amplification and absorption, respectively. If the optical wavelength is longer than the length-scale of spatial inhomogeneity in this mixture, the effective susceptibility χ_eff of the mixture is given by

$$\chi_\mathrm{eff} = \eta_\mathrm{a}\chi_\mathrm{a} + \eta_\mathrm{p}\chi_\mathrm{p} \tag{4.2}$$

where η_a and η_p are the fractions of active (susceptibility χ_a) and passive (susceptibility χ_p) materials [48]. By carefully choosing parameter values A, ω_0, and Γ to control the spectra of active and passive resonances, it is possible to realize either $\chi'_\mathrm{eff} > 0$, $\chi'_\mathrm{eff} < 0$, $\mathrm{d}\chi'_\mathrm{eff}/\mathrm{d}\omega > 0$, or $\mathrm{d}\chi'_\mathrm{eff}/\mathrm{d}\omega < 0$, *and* guarantee a transparency frequency where $\chi''_\mathrm{eff} = 0$.

In the next section, we outline how to choose parameter values to achieve either lossless negative-χ materials, high-index materials, superluminal light, or slow light,

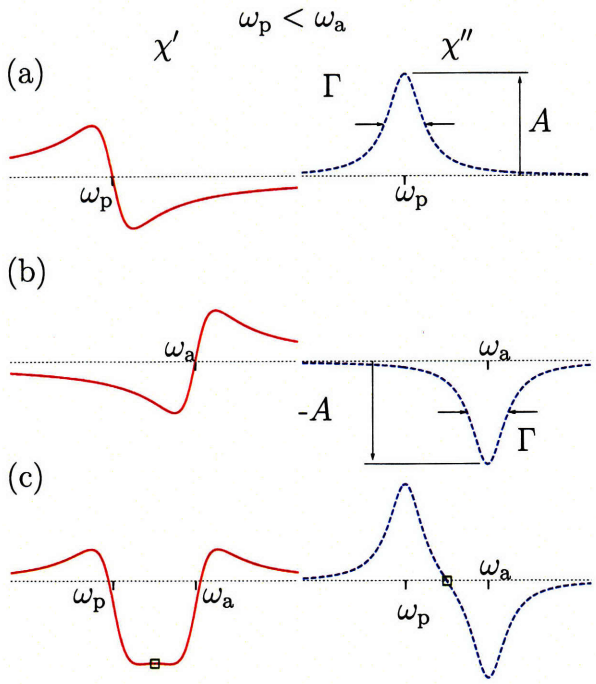

Figure 4-1: Plots of real (χ') and imaginary (χ'') components of susceptibility as a function of frequency ω for materials with $\chi' \ll 0$. If $\omega_a > \omega_p$, the susceptibilities of (a) passive and (b) active resonances can be combined to yield (c) a spectrum with $\chi' < 0$ and transparency. Green squares in (c) indicate the susceptibility value at the frequency where transparency is achieved.

each accompanied by transparency.

4.3 Novel optical phenomena achieved by mixing resonances

Negative susceptibility ($\chi' < 0$) with transparency can be realized with a mixture of active and passive resonances. The spectrum formed by a mixture of media with $\chi(|A_p|, \omega_p, \Gamma_a)$ and $\chi(-|A_a|, \omega_a, \Gamma_p)$, where $\omega_a > \omega_p$, exhibits negative susceptibility at a zero-loss frequency. This spectrum is illustrated in Fig. 4-1(c), where we have chosen $\Gamma_a = \Gamma_p$ and $\eta_p|A_p| = \eta_a|A_a|$. These requirements need only be approximately satisfied in order for the effect to be observed. When $0 < \chi'(\omega_t) < -1$, radiation at the transparency frequency ω_t will travel at superluminal group-velocities [45] in the resulting lossless low-index $n < 1$ medium. A similar spectrum was considered

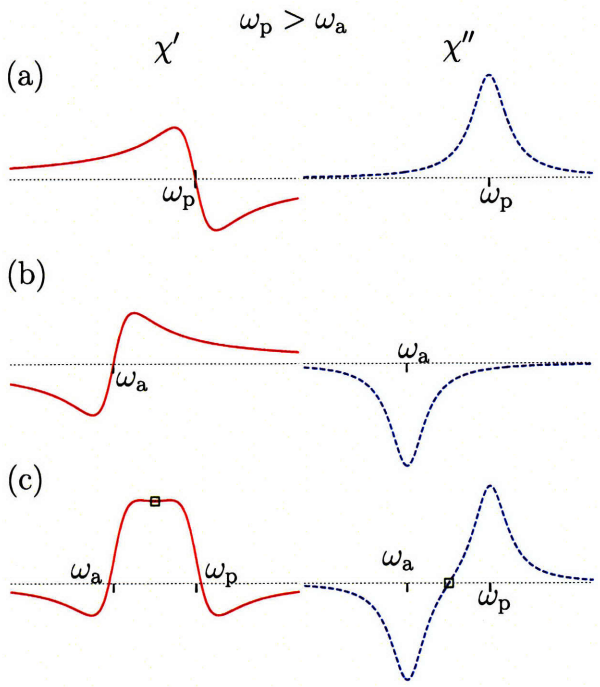

Figure 4-2: Plots of real (χ') and imaginary (χ'') components of susceptibility as a function of frequency ω for materials with $\chi' \gg 0$. If $\omega_a < \omega_p$, the constituents shown in (a) and (b) can be mixed to realize (c) a spectrum with $\chi' > 0$ and transparency. Green squares in (c) indicate the susceptibility value at the frequency where transparency is achieved.

in the context of Sommerfeld precursors and found to result in superluminal pulse propagation [49]. Media for which $\chi'(\omega_t) < -1$ correspond to lossless negative-ϵ media [15] and can also find utility in near-field lithography and microscopy [22].

Alternatively, large χ' accompanied by transparency can be obtained by mixing the same media but with $\omega_a < \omega_p$. Such a mixture is potentially useful as an immersion fluid for nanometer-resolution immersion lithography and microscopy [1, 3]. Figure 4-2(c) shows the spectrum resulting from choosing $\Gamma_a = \Gamma_p$ and $\eta_p|A_p| = \eta_a|A_a|$.

Mixtures of resonances can also be used to realize ultraslow light ($d\chi'/d\omega \gg 0$) and superluminal light ($d\chi'/d\omega \ll 0$) with transparency. Figure 4-3(c) shows a spectrum containing $d\chi'/d\omega \gg 0$ with transparency that was constructed by mixing passive (Fig. 4-3(a)) and active (Fig. 4-3(b)) media. Creating such a spectrum would normally require quantum interference on a multi-level atomic system [10, 31, 42]. However, in this case the spectrum was obtained by mixing equal proportions of media with $\chi(|A|, \omega_0, \Gamma_p)$ and $\chi(-|A|, \omega_0, \Gamma_a)$ and choosing $\Gamma_a < \Gamma_p$. An alternative

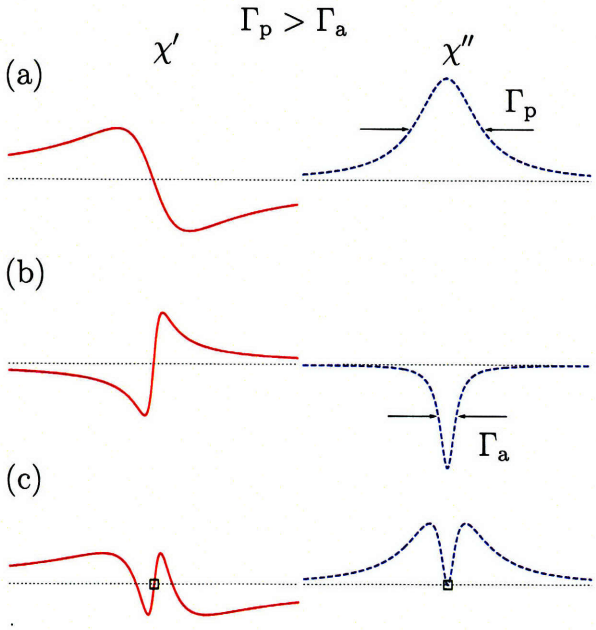

Figure 4-3: Real (χ') and imaginary (χ'') components of susceptibility as a function of frequency ω for materials with $d\chi'/d\omega \gg 0$ accompanied by transparency ($\chi'' = 0$). A spectrum with $d\chi/d\omega \gg 0$ and transparency is shown in (c), where materials with susceptibilities shown in (a) and (b) are mixed. The active resonance linewidth Γ_a is narrower than the passive resonance linewidth Γ_p. Green squares in (c) indicate the susceptibility value at the frequency where transparency is achieved.

choice for the relative magnitudes of active and passive resonance linewidths shown in Figs. 4-3(a-c) can result in a spectrum containing $d\chi'/d\omega \ll 0$ with transparency. Such a spectrum is conducive to achieving superluminal group velocity and is shown in Figs. 4-4(d-f), where $\Gamma_a > \Gamma_p$.

4.4 Proposed implementations

A number of possible implementations of this scheme are realizable. For example, one could mix resonances from optical transitions of two different atoms in a solid-state system, e.g. two rare-earth dopants in a glass host. Alternatively, one could mix resonances resulting from nonlinear optical phenomena such as stimulated Brillouin scattering (SBS) or stimulated Raman scattering (SRS) in the same material. One can even combine an atomic and nonlinear-optical resonance, e.g. an absorption

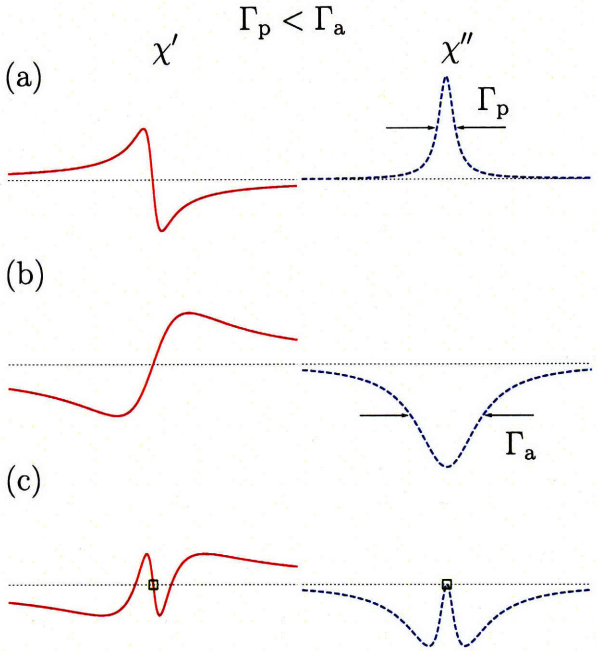

Figure 4-4: Real (χ') and imaginary (χ'') components of susceptibility as a function of frequency ω for materials with $d\chi'/d\omega \ll 0$ accompanied by transparency ($\chi'' = 0$). If $\Gamma_p < \Gamma_a$ as shown in (a) and (b), then the spectrum shown in (c) can be obtained where $d\chi/d\omega \ll 0$ with transparency. Green squares in (c) indicate the susceptibility value at the frequency where transparency is achieved.

profile from dopant atoms and SBS. In fact, these schemes can be realized in *any* material where Eq. 4.2 holds and where collision and broadening effects are minimal, regardless of the physical origin of the resonances. We will now describe a specific example implementation where two SBS resonances are mixed to speed up or slow down an optical pulse.

SBS is a nonlinear optical phenomenon where energy transfer between oppositely-propagating optical waves is mediated by an acoustic wave with frequency Ω_B [50]. An optical pump at frequency ω_{pump}, via SBS, creates both an active resonance at $\omega_{pump} - \Omega_B$ and a passive resonance at $\omega_{pump} + \Omega_B$ that can interact with a counter-propagating probe optical wave. Consider a medium in which two co-propagating pumps, with fields E_1 and E_2, and one counter-propagating probe with field E have frequencies $\omega_1 < \omega < \omega_2$ and corresponding wavevectors $k_1 < k < k_2$, and have fields

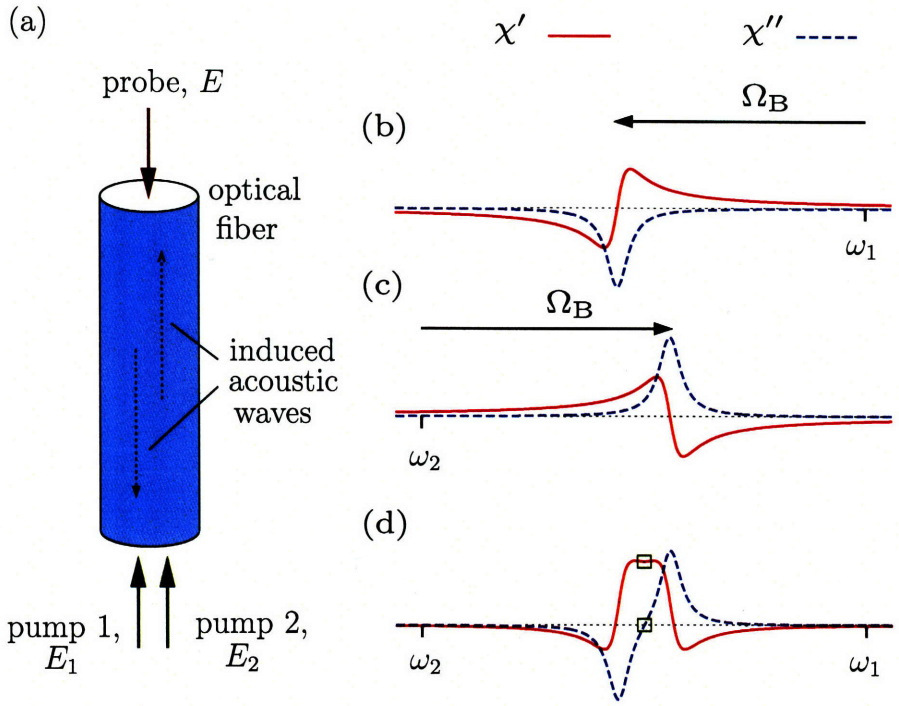

Figure 4-5: A schematic of a proposed physical realization of medium with either high or low index with transparency is shown in (a). An active resonance, shown in (b), and a passive resonance, shown in (c), are generated using stimulated Brillouin scattering. By choosing pump frequencies that are separated by slightly less than $2\Omega_B$, one can create the probe spectrum shown in (d). The spectrum shown in Fig. 4-1(c) can be obtained by separating pump frequencies by slightly more than $2\Omega_B$. Green squares in (d) indicate the susceptibility value at the frequency where transparency is achieved.

given by

$$E_m(z,t) = A_m(z,t)e^{i(k_m z-\omega_m t)} + \text{c.c.}, m = 1,2 \tag{4.3a}$$

$$E(z,t) = A(z,t)e^{i(-kz-\omega t)} + \text{c.c.} \tag{4.3b}$$

where A_1, A_2, and A are slow-varying functions in time and space. Two counter-propagating acoustic waves are generated via electrostriction at the difference frequencies $\Omega_1 = \omega - \omega_1$ and $\Omega_2 = \omega - \omega_2$ with wave vectors $q_1 = k + k_1$ and $q_2 = k + k_2$.

The resulting polarization for the probe wave is expressed in terms of active and

passive resonances as

$$\bar{P} = \left[\chi_{\mathrm{bg}} + \chi(A_{\mathrm{p}}, \omega_{\mathrm{p}}, \Gamma_{\mathrm{B}}) + \chi(-A_{\mathrm{a}}, \omega_{\mathrm{a}}, \Gamma_{\mathrm{B}})\right]\bar{E}, \tag{4.4}$$

where $\omega_{\mathrm{p}} = \omega_1 + \Omega_{\mathrm{B}}$, $\omega_{\mathrm{a}} = \omega_2 - \Omega_{\mathrm{B}}$, χ_{bg} is the linear background susceptibility, Γ_{B} is the Brillouin linewidth, and we have ignored terms of the order $(q_2 - q_1)^2$ in comparison to q_1^2 and q_2^2 since $q_1 \approx q_2$ [50]. In this equation, $\chi(A_{\mathrm{p}}, \omega_{\mathrm{p}}, \Gamma_{\mathrm{B}})$ is the passive resonance that results via anti-Stokes SBS from the pump field at ω_1, while $\chi(-A_{\mathrm{a}}, \omega_{\mathrm{a}}, \Gamma_{\mathrm{B}})$ is the active resonance that results via Stokes SBS from the pump field at ω_2. Parameters A_{p} and A_{a} are given by $A_{\mathrm{p}} = Sq_1|A_1|^2$ and $A_{\mathrm{a}} = Sq_2|A_2|^2$, where S is a constant encompassing the material parameters [50]. The resulting spectra of this mixture of active and passive resonances where $A_{\mathrm{p}} = A_{\mathrm{a}}$ are shown in Figs. 4-1(c) and 4-2(c) for $\omega_{\mathrm{a}} > \omega_{\mathrm{p}}$ and $\omega_{\mathrm{a}} < \omega_{\mathrm{p}}$, respectively. At the transparency point, the probe will experience $\chi' < \chi'_{\mathrm{bg}}$ (Fig. 4-1(c)) and $\chi' > \chi'_{\mathrm{bg}}$ (Fig. 4-2(c)). This modification of χ'_{bg} can be used to delay or speed up an optical pulse. If we assume $A_{\mathrm{p}} = A_{\mathrm{a}}$, the maximum delay or speed-up of an optical pulse occurs when the resonances are spaced by Γ_{B} (i.e. $|\omega_{\mathrm{a}} - \omega_{\mathrm{p}}| = \Gamma_{\mathrm{B}}$). Calculations show that using a 1-km-long optical fiber made with Lucite [51] at λ =1.55 μm, 100 mW pump power, and fiber core diameter of 1 $\mu\mathrm{m}^2$, an optical pulse can be delayed or sped up by 85 ns. An experiment that demonstrates this delay, and hence, change in index with neither gain nor loss, will need a setup similar to one used for other slow- and fast-light experiments involving SBS [43, 44] (in these experiments, the pulse was amplified/attenuated while being delayed/sped up, while in our case, the pulse amplitude is unchanged).

We will now describe a second implementation of the framework described in this chapter that enhances the spatial-frequency bandwidth of super-resolving lens used for high-resolution near-field imaging and lithography [22, 23]. In his proposal for implementing a near-perfect optical lens, Pendry reported that a 40-nm-thick slab of silver where $\epsilon = -1 + 0.4i$, can resolve an object with subwavelength features so long as the electric and magnetic field are decoupled [15]. While Pendry's prediction has been experimentally verified, losses in the silver slab limitted the fidelity of the

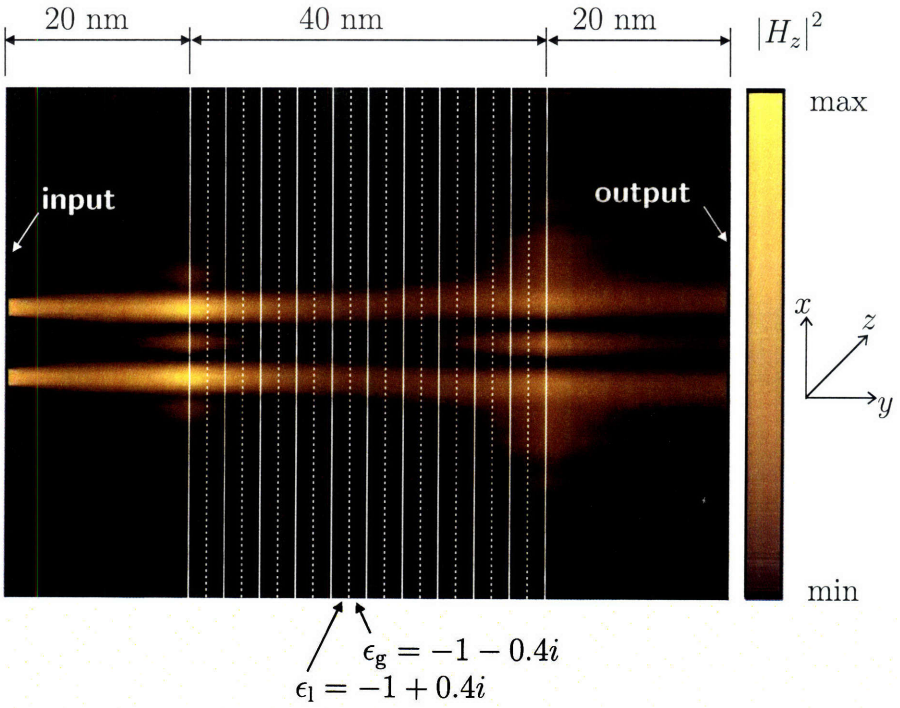

Figure 4-6: The calculated field intensity $|H_z|^2$ for a super-resolving lens composed of bilayers of attenuating (ϵ_l) and amplifying media (ϵ_g) is shown for the input field intensity shown in Fig. 4-7(a).

image [15, 22, 23].

Our calculations show that the resolution can be greatly enhanced (and losses greatly reduced) by using a thin-film stack of alternating attenuating and amplifying layers in place of a silver slab. We used finite-element software (COMSOL 3.2 [52]) to calculate the magnetic field intensity resulting from the propagation of an object with subwavelength features through a bilayer stack. We used identical parameters to those given in Ref. [15] in our calculations. The spatial distribution of the magnetic field intensity is shown in Fig. 4-6, while the object and image field intensities are shown in Fig. 4-7(a) and (b), respectively. Clearly, the image resulting from a bilayer stack has higher contrast than the image after a silver slab or free space because the higher spatial frequencies that decay in the case of a silver slab do not decay for a bilayer stack.

Intuitively, one can attribute the propagation (versus attenuation) of higher spatial frequencies in the case of a bilayer stack to the transparency condition that is met

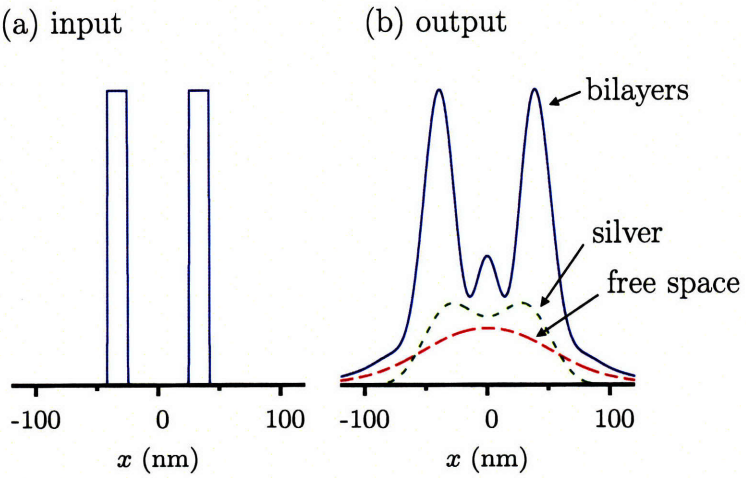

Figure 4-7: The calculated field intensity $|H_z|^2$ for a super-resolving lens composed of bilayers of attenuating (ϵ_l) and amplifying media (ϵ_g), 40-nm-thick silver slab, and free space are shown in (b) for the input field intensity shown in (a). The illumination free-space-wavelength used in the simulation was 356-nm light.

when active and passive materials are equally mixed (i.e. $\chi''_{\text{eff}} = 0$). To quantify our intuition, we used the transfer-matrix method [53] to calculate the transmission spectrum of input spatial frequencies. A similar calculation and result can be found in Ref. [47].

In the transfer matrix method, matrices are used to describe the transformation of the coefficients of forward and backward propagating components of the electric field as they encounter an interface or propagate through a dielectric. Full derivations for each matrix can be found in Ref. [53]. Figure 4-8 shows a generalized version of the geometry that we used in our calculation. The i^{th} layer in the geometry has a refractive index (assume $\mu_i = 1$) is given by

$$n_i = \sqrt{\epsilon_i} \tag{4.5}$$

The component of the wave vector in the direction of propagation in the i^{th} layer is given by

$$\kappa_i = \sqrt{\left(\frac{n_i \omega}{c}\right)^2 - \beta^2}, \tag{4.6}$$

where β is the spatial frequency of the object. The matrix that describes the trans-

formation of the coefficients between an interface composed of the i^{th} and j^{th} layer for a p-polarized (in-plane) electric field is given by

$$D_{ij} = \frac{1}{2}\begin{pmatrix} 1+\frac{n_j^2\kappa_i}{n_i^2\kappa_j} & 1-\frac{n_j^2\kappa_i}{n_i^2\kappa_j} \\ 1-\frac{n_j^2\kappa_i}{n_i^2\kappa_j} & 1+\frac{n_j^2\kappa_i}{n_i^2\kappa_j} \end{pmatrix}, \tag{4.7}$$

while

$$P_m = \begin{pmatrix} e^{-i\kappa_m d_m} & 0 \\ 0 & e^{i\kappa_m d_m} \end{pmatrix} \tag{4.8}$$

describes the propagation in the m^{th} layer, where d_m is the thickness of layer m. To calculate the transformation of coefficients for the entire system shown in Fig. 4-8, we simply chain a series of D and P matrices to obtain

$$M = P_1 \cdot D_{12} \cdot (P_2 \cdot D_{23} \cdot P_3 \cdot D_{32})^{(N-1)} \cdot P_2 \cdot D_{23} \cdot P_3 \cdot D_{31} \cdot P_1. \tag{4.9}$$

The transmission coefficient T is given by

$$T = |\frac{1}{M_{11}}|^2 \tag{4.10}$$

A plot of the transmission T as a function of the spatial frequencies result is shown in Fig. 4-9, where we find that the bandwidth for a bilayer stack is three larger than that of silver. Figure 4-9 also shows that spatial frequencies near the resonance frequencies are unequally amplified and attenuated, which explains the appearance of slight distortion in the output intensity shown in Fig. 4-7(b) for the bilayer stack.

4.5 Conclusion.

We have prescribed a framework that presents a simple approach to refractive index engineering. Our framework does not require quantum coherence to exhibit $\chi' > 0$, $\chi' < 0$, $\mathrm{d}\chi'/\mathrm{d}\omega > 0$, or $\mathrm{d}\chi'/\mathrm{d}\omega < 0$ with transparency. Implementations of our framework could permit application of novel optical methods to next-generation immersion

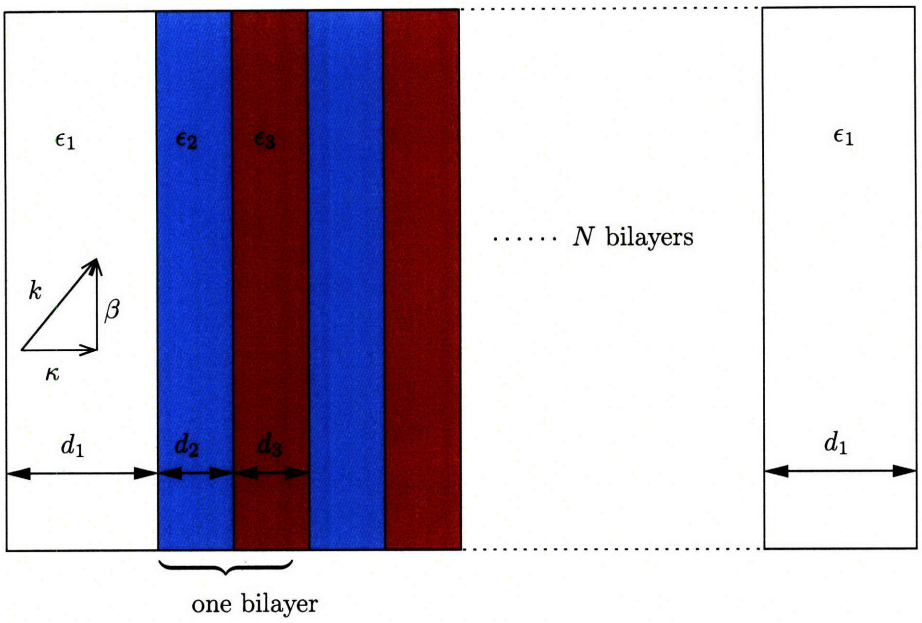

Figure 4-8: Schematic of the geometry used for matrix-method calculations.

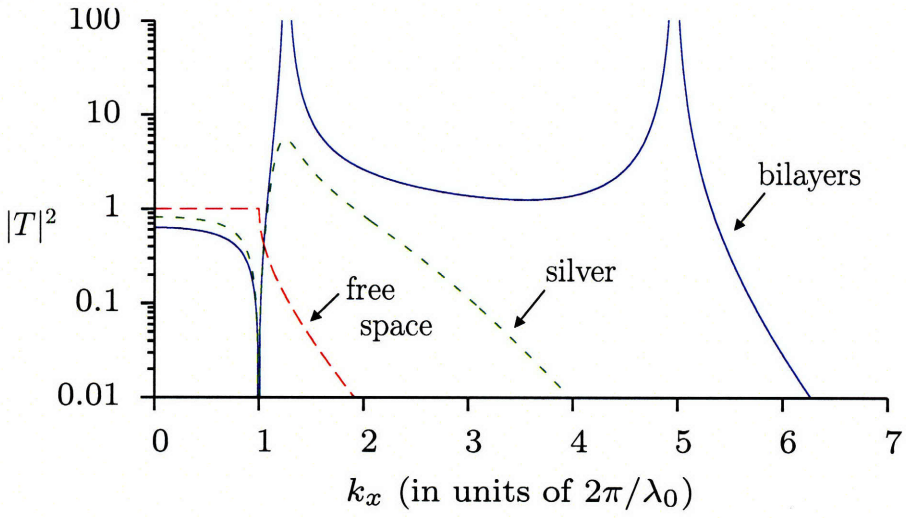

Figure 4-9: Plot of the transmission coefficient as a function of spatial frequencies for the geometry shown in Fig. 4-8 for an illumination wavelength of 356 nm. This plot demonstrates that the bilayer medium resolves the object better than silver because high spatial frequencies can propagate without loss.

optical lithography systems, near-field microscopy, and optical pulse storage.

Part II

Engineering the properties of subwavelength optical devices: Polarization sensitive superconducting single photon detectors

Chapter 5

Introduction to superconducting nanowire single photon detectors

In this chapter, we will introduce the reader to the optical design challenges for SNSPDs. SNSPDs are subwavelength nanostructures that, as the name suggests, are sensitive to single photons. Research within our group has focused on fabrication techniques [54], understanding the electrical response of this device [55], and on its applications in optical communication [56]. We have also recognized that optical design is very important for realizing efficient detectors. By integrating optical microcavities to SNSPDs, we achieved detection efficiencies of 57% at a wavelength of 1.55 μm [57]. However, more work on the optical design is necessary to push this number to above 90%. A detection efficiency this high is needed for many applications that use these detectors. For example, photon-number resolving detectors requires high efficiency to discriminate with high certainty [58–60]. In addition, high detection efficiency detectors can also boost data-rates for free-space optical communication [56], and quantum computation that uses linear optics [61]. In this thesis, our goal is to understand and characterize the optics of SNSPDs, and thereby enable an optical design that maximizes detection efficiency.

We will now briefly describe the mode of operation of SNSPDs and then define the issues that constrain the optical design. A review of SNSPDs can be found in Ref. [62].

5.1 Mode of operation

An SNSPD is composed of a niobium nitride (NbN) superconducting nanowire, that is typically 100-nm wide and 4-nm thick. The nanowire is fabricated in a boustrophedonic pattern on an optically transparent substrate. A schematic of an SNSPD is shown in Fig. 5-1.

In order for the SNSPD to operate efficiently, a current that is just under the critical current is passed through the superconducting nanowire. When a photon is absorbed by the nanowire, a resistive, quasi-particle-rich region (i.e., a so-called 'hotspot') forms in the nanowire with probability P_{R}. The hotspot offers a path of higher resistance to the current, so naturally, the supercurrent tries to avoid it by flowing around it. As a result, three events occur in quick succession: (1) the current density increases above the critical value in the vicinity of the hotspot; (2) the wire is driven from the superconducting state into the normal (i.e., resistive) state; and (3) a voltage appears across across the nanowire. The wire transitions back into the superconducting state in a few nanoseconds. This mechanism, called the hotspot model, was proposed by Gol'tsman *et al.* [63] but has not been rigorously tested in the context of our devices.

5.2 Optical design challenges

The detection efficiency depends on two quantities: the absorptance[1] A, and the probability of resistive state formation due to an absorption event P_{R}. Both of these quantities need to be maximized to make efficient detectors. In this thesis, we will focus our attention on the absorptance. We will now discuss the hurdles to achieving maximum absorption of every photon.

[1]Absorptance is the ratio of the absorbed power to incident power, not to be confused with absorption, which is the process of being absorbed.

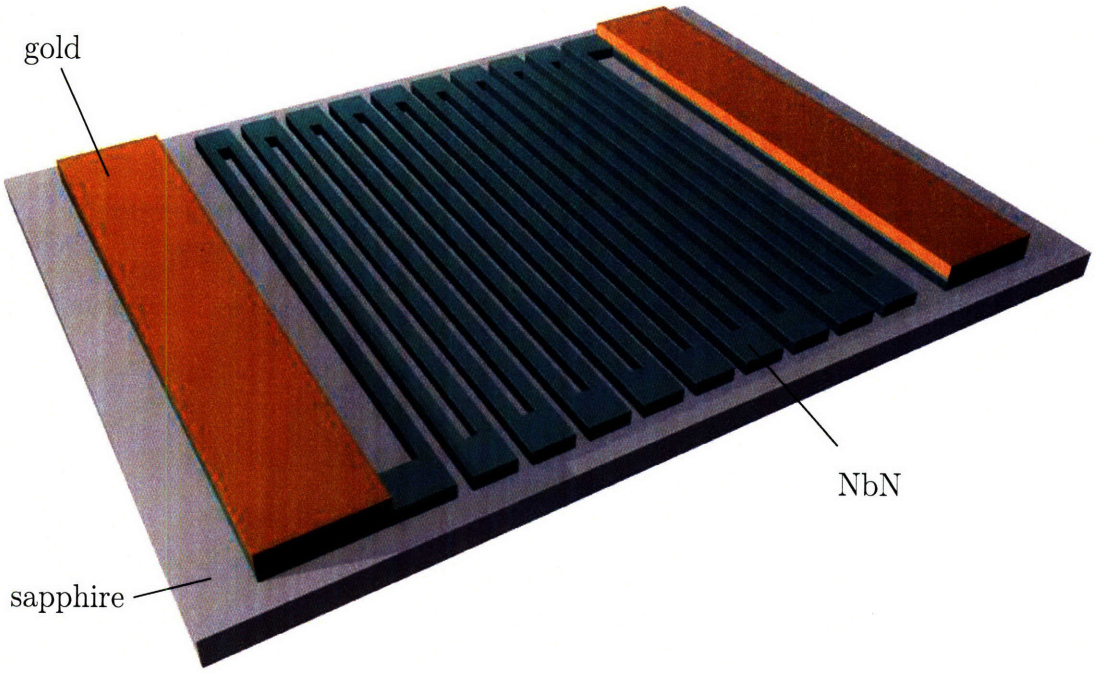

Figure 5-1: Schematic of a superconducting nanowire single photon detector. When a near-infrared photon strikes the current-carrying superconducting nanowire, it can cause the wire to enter a resistive state and be detected.

5.2.1 Geometry

The first impediment to achieving perfect absorption is the geometry of SNSPDs. The operating principle requires nanowires because a nanowire has a small cross-sectional area and hence suitable resistance and inductance properties for electrical operation. As a result, there are gaps between the nanowires through which a photon can escape. While a detector with smaller gaps between nanowires may have higher absorption than detector with larger gaps, making SNSPDs with small gaps is challenging. To avoid over-engineering our fabrication process, we need a quantitative measure of the marginal gains as the gap between nanowires is reduced.

5.2.2 Subwavelength structures

The nanowire width, typically 100 nm, appears subwavelength in comparison to a 1550-nm-wavelength photon. The subwavelength pattern defined by the nanowires has an intrinsic polarization sensitivity. This polarization sensitivity results in a

preferential detection of photons with one polarization and rejection of photons with the other polarization. This sensitivity can be a problem with applications where the polarization of incoming photons is not fixed.

Another dimension that is subwavelength is the nanowire thickness, normally between 4 nm and 6 nm. The subwavelength thickness is necessary for efficient electrical operation of the device, but is thin enough that a photon can tunnel through the film and avoid absorption.

5.2.3 Index mismatch and uncertainty

Another barrier to perfect absorption is an index mismatch between the superconducting film and its interfacing material. For example, if we illuminate an SNSPD from the air side, then many photons are reflected because of the air-NbN index mismatch. Compounding the problem of a possibly large index mismatch between NbN and air is the fact that we only have data for a thick film ($\sim$ 12 nm) taken at room temperature. The refractive index is known to change with film thickness e.g. for SiO_2 [64, 65], and to a much lesser extent, with temperature, e.g. for sapphire [66]. We do not know how the refractive index will change with these two parameters for NbN.

5.3 Our approach

Our approach to tackling these design challenges is to theoretically and experimentally understand their impact on the absorptance of SNSPDs. We will start by modeling the detector as a subwavelength grating using the refractive index values at room temperature. This modeling will, at the least, give a qualitative understanding of the contributors to efficient optical absorption for our structures. At best, the model will require some tweaks in order to have good quantitative agreement with experiment. The modeling approach and results are presented in Chapter 6.

We will then fabricate devices that will be used to validate the model. In Chapter 7, we present fabrication results and advanced techniques that we used in fabricating

SNSPDs. In Chapter 8, we describe the testing techniques that we used for validating the model. Once the model and modeling technique have been validated, it will be possible to design detectors that optimize efficiency, polarization sensitivity, or some other desirable optical characteristic.

Chapter 6

Modeling the optical properties of superconducting nanowire single photon detectors

In this chapter, we will build an optical model of SNSPDs. We will probe the dependence of the absorptance on geometrical parameters and on polarization. This dependence will be tested in Chap. 8. Knowledge and verification of the dependence of absorptance on these parameters will help us understand how to build more efficient detectors.

We will first review prior work where subwavelength structures similar to ours have been modeled.

6.1 Background

We will concentrate on the literature surrounding wire grid polarizers because they most closely match the geometry of our detectors [67, 68]. It is worth mentioning that subwavelength optical structures have been the focus of many recent articles, especially on structures that employ surface plasmons to exhibit interesting optical phenomena [69–71].

6.1.1 Introduction to wire grid polarizers

The wire grid polarizer (WGP) is a polarization-sensitive device composed of periodic, subwavelength, metallic gratings fabricated on an optically transparent substrate. As a result of their polarization sensitivity, WGPs can be used as polarizers and as polarizing beam-splitters. We will now present two intuitive pictures to explain why WGPs are sensitive to polarization.

In the first picture, an electric field, polarized parallel to the metal wires, forces conduction electrons on the WGP to oscillate along the length of the wire [72]. Because the electron motion is unrestricted, the WGP interacts with the field as a metallic film would, and the wave is reflected. For the perpendicular polarization, the conduction electrons are restricted in their oscillation, and therefore, transmit much of the field.

In the second picture, we can use continuity conditions imposed by Maxwell's equations to intuit why a parallel-polarized electric field incurs more loss in the nanowires than a perpendicular-polarized electric field. Continuity conditions for a parallel-polarized electric field (Faraday's law) imply that the field in air is continuous with the field in the nanowire. As a result, a large field intensity is present in the nanowire as shown in Fig. 6-1, and leads to an equally large loss. On the other hand, continuity conditions for a perpendicular-polarized electric field (Gauss' law) imply a discontinuous electric field between air and the nanowire mediated by the presence of a surface charge on the air-nanowire interface. More of the field is confined to air than in the nanowire, as shown in Fig. 6-1, because its refractive index is lower in comparison to the nanowire. As a result, a lower loss occurs in the nanowire for the perpendicular polarization than for parallel polarization.

Theoretical work on WGPs has been ongoing since the 1970s. Early papers focused on effective medium theory to explain their optical properties. We will review effective medium theory and see how it relates to our detectors. We will then motivate why we ended up using numerical methods to model SNSPDs.

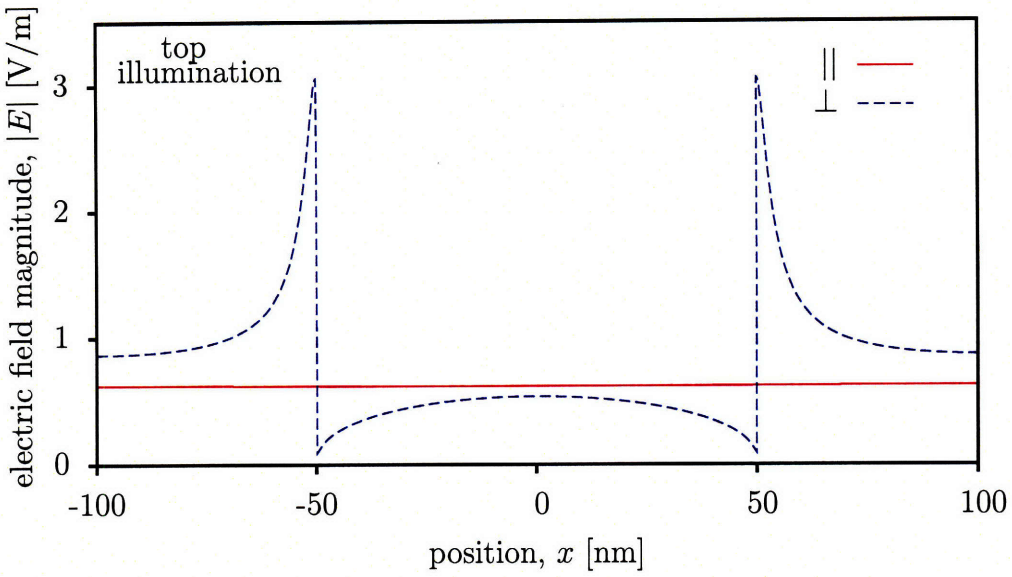

Figure 6-1: Plot of the magnitude of the electric field $|E|$ as a function of position x for a single period of a 100-nm-wide, 200-nm-pitch grating for parallel ($||$) and perpendicular ($\perp$) polarizations. The cross-section was taken at a height $z = 2$ nm above the sapphire substrate (geometry shown in Fig. 6-4). Parameters of this simulation were: wavelength = 1.55 μm, NbN thickness = 4 nm, oxide thickness = 2 nm, and top illumination. Refractive indices of the materials are given in Table 6.1.

6.1.2 Effective medium theory

Effective medium theory is applied to periodic media such as WGPs by relating the optics of periodic media to birefringent media. This application of effective medium theory is called form birefringence theory. Form birefringence theory was developed in 1956 by Rytov [73] for normal illumination and extended to arbitrary angles of illumination in the 1977 by Yeh and Yariv [74, 75]. We will now describe the results of this theory.

In form birefringence theory, the dispersion relation is found for Bloch waves travelling in a periodic 1D grating [74, 75]. The dispersion relation is different for parallel and perpendicular polarizations. We can extract the effective ordinary ($n_{||}$)

and extraordinary ($n_\perp$) indices of refraction:

$$\begin{aligned} n_{||}^2 &= \frac{a}{\Lambda} n_1^2 + \frac{b}{\Lambda} n_2^2, \\ \frac{1}{n_\perp^2} &= \frac{a}{\Lambda}\frac{1}{n_1^2} + \frac{b}{\Lambda}\frac{1}{n_2^2}, \end{aligned} \tag{6.1}$$

from the dispersion relation by assuming a grating periodicity Λ that is smaller than the wavelength. In Eq. (6.1), a and b are the widths of the media with index n_1 and n_2, respectively, that compose the grating, and $a + b = \Lambda$. The Fresnel equations can be used to obtain reflection and transmission coefficients for a lamellar grating with height h sandwiched by semi-infinite media with index n_a and n_s [76]:

$$\begin{aligned} r_j &= \frac{r_{12} + r_{23} e^{2i\beta_j}}{1 + r_{12} r_{23} e^{2i\beta_j}}, \\ t_j &= \frac{t_{12} t_{23} e^{i\beta_j}}{1 + r_{12} r_{23} e^{2i\beta_j}}. \end{aligned} \tag{6.2}$$

In these equations,

$$r_{12} = \frac{n_\mathrm{a} - n_j}{n_\mathrm{a} + n_j}, \qquad r_{23} = \frac{n_j - n_\mathrm{s}}{n_j + n_\mathrm{s}}, \tag{6.3}$$

$$t_{12} = \frac{2n_\mathrm{a}}{n_\mathrm{a} + n_j}, \qquad t_{23} = \frac{2n_j}{n_j + n_\mathrm{s}}, \tag{6.4}$$

$$\beta_j = \frac{2\pi}{\lambda} n_j h, \qquad \text{and} \quad j = ||, \perp . \tag{6.5}$$

We can use this result to find the absorptance for a 4-nm-thick NbN grating with 100-nm-wide nanowires and 200-nm pitch on a sapphire substrate at a wavelength of 1.55 μm. By setting $n_1 = 1$ (air), $n_2 = 5.2 + i5.8$ (NbN [77]), $n_\mathrm{a} = 1$ (air), $n_\mathrm{s} = 1.75$ (sapphire [78]), $a = b = 100$ nm (wire width), $h = 4$ nm (grating thickness), and using $A_j = 1 - R_j - T_j$, where R_j and T_j are the reflectance and transmittance given by

$$R_j = |r_j|^2, \qquad T_j = \frac{n_\mathrm{s}}{n_\mathrm{a}} |t_j|^2, \qquad j = ||, \perp, \tag{6.6}$$

we find that the absorptance for parallel polarization is $A_{||} = 0.19$, while for perpen-

dicular polarizations is $A_\perp = 0.0029$. The ratio of parallel to perpendicular absorptance $A_{||}/A_\perp$ is predicted, quite unexpectedly, to be around 670. At the time when we first performed these calculations, we could not measure the absorptance or absorptance ratio directly. But we had the resources to measure the detection efficiency (DE) of SNSPDs. We measured that the ratio of maximum DE ($\mathrm{DE_{max}}$) to minimum DE ($\mathrm{DE_{min}}$) was between 2 and 3 for devices with similar geometry. While $\mathrm{DE_{max}}/\mathrm{DE_{min}}$ is not the same as $A_{||}/A_\perp$, we certainly did not expect a difference of 2 orders of magnitude. Our instincts were correct: a closer look at the literature revealed that form birefringence theory is ineffective for the perpendicular polarization when gratings are very thin. A comparison of effective medium theory to rigorous coupled-wave analysis (RWCA), a method that requires numerical computation, yields that $n_\perp$ changed by around 50% in the small grating depth limit [79].[1]

Clearly, the literature was pointing us towards numerical methods to solve our problem. One option was to use RCWA, where a Fourier decomposition of the field and dielectric function of the grating are found on route to realizing a set of differential equations that can be solved numerically [80]. But we did not use RCWA to solve our problem mainly because it would prove cumbersome to adapt to arbitrary geometries in the future. Moreover, we had other numerical techniques at our disposal. We will now describe two methods that we considered that allow for arbitrary geometry and straightforward implementation.

6.1.3 The finite-difference time-domain method

The finite-difference time-domain (FDTD) method is a very intuitive and powerful method for directly solving Maxwell's equations [81]. FDTD works by discretizing Maxwell's equations and updating electric and magnetic field on an offset spatial and temporal grid. It was first proposed in 1966 [82], and has since been heavily developed by the research community. A good review of the literature surrounding the FDTD

[1] In Ref. [79], RCWA and effective medium theory were compared in one simulation to see how $n_\perp$ changes with grating-depth. The authors used a lamellar grating with $n_1 = 1$, $n_2 = 3$, $n_a = 1$, and a variable h as their simulation geometry. We can infer from Fig. 6 in Ref. [79] that for small grating depth h, good agreement can be found for $n_{||}$ but not for $n_\perp$ in Eq. (6.1).

method can be found in Ref. [83].

The FDTD method has been used to solve many problems in nanophotonics. For example, Schuck and coworkers used the FDTD method to solve for the field enhancement due to metallic bowtie nanoantennae and found good experimental agreement [84]. However, we found that FDTD was not well suited to our problem because it is implemented in software (e.g. MEEP [85], TEMPEST [86]) with a uniform spatial grid, or mesh. While the uniform spatial grid does not pose a problem where the geometry is proportioned equally in all dimensions, our geometry contains structures that are 4-6 nm (NbN thickness), 50-200 nm (nanowire width), hundreds of nm (cavity thickness), to many micrometers (total detector area). The FDTD method with a uniform grid would require too many grid points and therefore, place large demands on our computing power.

We will now examine the finite-element method, a numerical technique where the grid can be nonuniform.

6.1.4 The finite-element method

In contrast to FDTD, where the *differential equations* that form Maxwell's equations are discretized, the finite element method (FEM) approximates the *solution* on a discrete spatial grid. FEM works by breaking down the problem into pieces, or elements, where approximate solutions can be constructed. The local approximations are then combined to form a global solution. As the number of mesh elements is increased, the FEM converges to the real solution.

To illustrate the FEM, consider the following example[2] where we want to find the circumference of a circle with radius R. We can divide the circle into a number of elements (arcs) as shown in Fig. 6-2(a). The endpoints of these elements are called nodes. The local approximations of the solution on the elements of the length of the i^{th} element, h_i can be easily found using trigonometry as shown in Fig. 6-2(b). The sum of the elements $\sum_i h_i$, gives an approximation to the circumference.

One major advantage of the FEM over the FDTD method is that the nodes

[2]Adapted from Ref. [87].

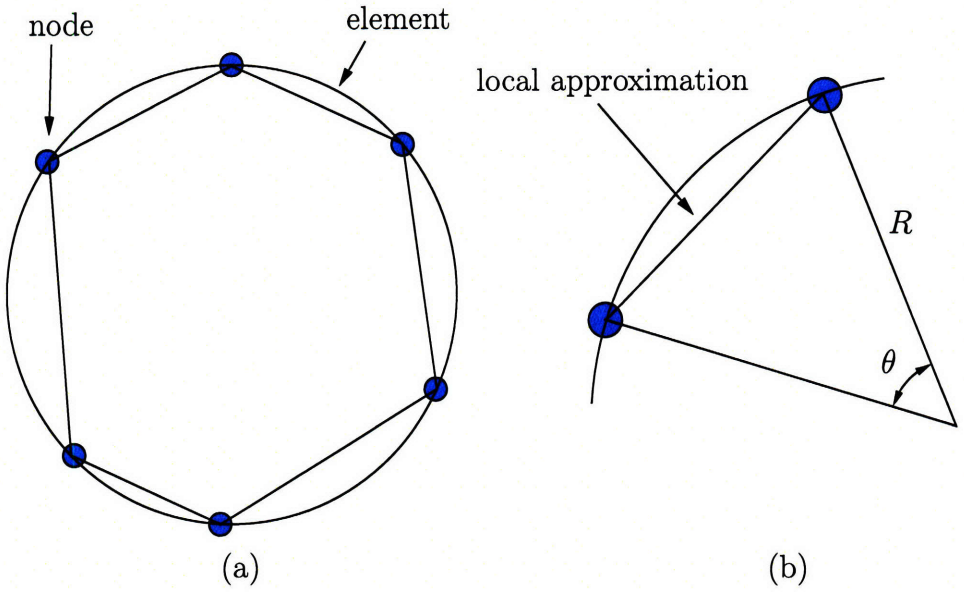

Figure 6-2: Schematic showing the finite-element method applied to the problem of finding the circumference of a circle. (a) shows a circle with radius R and nodes that divide the circle into elements (arcs). (b) shows how we take the local approximation of the length of an element by finding the length of a cord connecting the nodes.

can be spaced nonuniformly. A nonuniform mesh, also called an adaptive mesh, can improve accuracy and be computationally efficient. This advantage drove us to choose the FEM over FDTD in our simulations. We can illustrate the advantage of such a nonuniform mesh by an extension of the previous example. Lets consider the problem of finding the perimeter of the shape shown in Fig. 6-3. In order to improve accuracy and minimize the number of nodes, we can place nodes closely spaced in regions of high curvature and further apart on regions of low curvature.

We will now describe how we implemented the simulation using a commercial FEM code called Comsol Multiphysics (formerly FEMLab).

6.2 Calculating absorptance using the finite-element method

We used Comsol Multiphysics (version 3.2b) with the Electromagnetics Module, an add-on package with different formulations of Maxwell's equations [52]. We used the

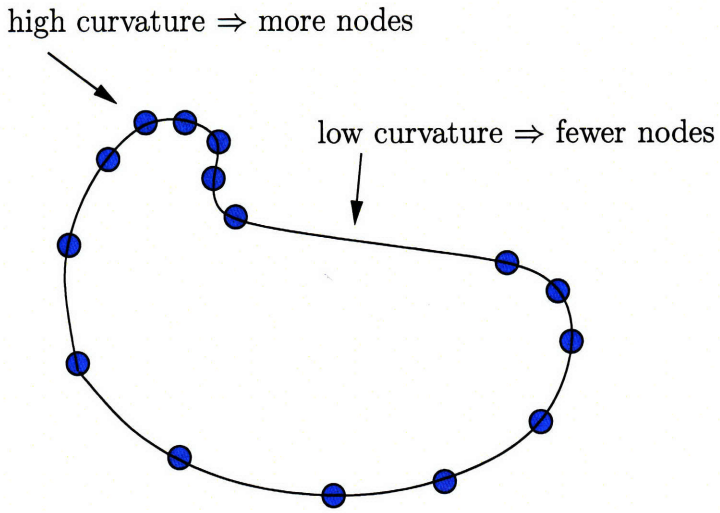

Figure 6-3: Schematic illustrating a nonuniform mesh that can be used to find the perimeter of an arbitrary shape using the the FEM. To improve accuracy and minimize the number of nodes, we can place closely-spaced nodes in regions of high curvature and sparsely-spaced nodes in regions of low curvature.

'In-plane Hybrid-Mode Waves' mode in the Electromagnetics Module. This mode implements the full formulation of Maxwell's equations but confines the incident wave vector to the plane. We simulated our structures in Comsol by defining the (1) geometry, (2) boundary conditions, (3) material parameters, and (4) mesh parameters before (5) solving the problem for the parameters of interest. We used the programming language instead of using Comsol's graphical user interface because we could easily change the geometry in code, and perform batch processing of the simulations. We will now describe each of these five steps in more detail for the geometry used to generate Figs. 6-6 to 6-13. Similar steps were followed with other geometry for the remaining results presented in this chapter.

6.2.1 Setting up the problem

The first step was to define the model geometry. We decided to model the SNSPD as an infinite grating so that we could make use of symmetry and solve the problem with computational efficiency. However before approximating the geometry in this way, we need to make sure that a comparison of experiment and simulation is meaningful.

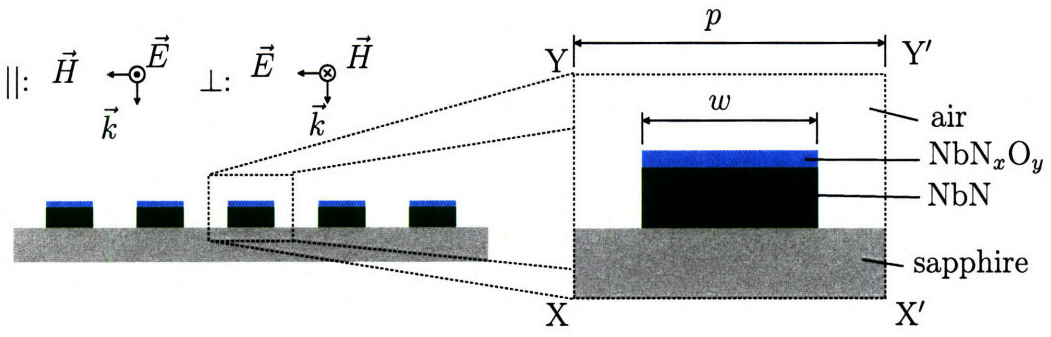

(a) device cross-section (b) unit cell

Figure 6-4: Schematic of simulated geometry. (a) shows the cross-section of the SNSPD geometry approximated to an infinite wire grid. (b) shows the unit cell that was implemented in the simulation. For top illumination, the wave is emitted from edge YY′, while for bottom illumination, the wave is emitted from edge XX′.

Another way to state the problem is, "In what limit does an SNSPD appear like an infinite grating for our experiments"? For our absorptance measurements, the SNSPD geometry needs to be larger than the area illuminated by the laser, which was the case.

We will now describe the geometry in detail. The cross-section of an infinitely long grating is shown in Fig. 6-4(a). An infinite grating geometry was ideal to use with the 'In-plane Hybrid-Mode Waves' mode in the Electromagnetics Module because a wave vector normal to the gratings would be confined in the plane. We took advantage of the lateral symmetry of this grating and defined the unit cell shown in Fig. 6-4(b) as our model. The length of the unit cell was equal to the pitch p, with the NbN wire centered in the middle of the geometry with width w and thickness t. We also defined an oxide layer on top of the NbN wire with a thickness of 2 nm. We did not need to include the entire thickness of sapphire (which can be hundreds of μm) in our unit cell because interference is not present over those length scales for pulsed light (used when measuring detection efficiency), or when an anti-reflection coating is present on the bottom sapphire-air interface (when absorptance was measured).

The second step was to define the boundary conditions and material parameters. In most simulations, the field entered the geometry through the top edge (YY′) with either an out of plane ($E_{||}$), or in-plane ($E_{\perp}$) electric field. In a few simulations,

Table 6.1: Complex refractive indices of the materials used in our simulations, given at $\lambda = 1.55$ μm. Note that in Comsol, the complex refractive index for an absorptive medium is given by $n = n' - i\,n''$ whereas the convention we have used in this thesis is $n = n' + i\,n''$.

Material	Complex refractive index	Reference
NbN	5.23 + i 5.82	[77]
NbN_xO_y	2.28	[77]
Al_2O_3 (sapphire)	1.75	[78]
HSQ	1.39	[77]
gold	0.51 + i 10.72	[89]

we illuminated the wire from the bottom surface (XX′). We used periodic boundary conditions on the left (XY) and right edges (X′Y′), and scattering boundary conditions [88] on the top and bottom surfaces. Scattering boundary conditions were necessary to eliminate reflections back into the geometry. We found that scattering boundary conditions had the same accuracy as perfectly matched layers (PML) [88] when the field was normally incident on the geometry. For off-normal incidence, PMLs may be necessary to absorb any scattered waves.

The third step was to define the material parameters at 1.55 μm, the wavelength of the simulation. The refractive indices used for the various materials are listed in Table 6.1. In simulations involving optical cavities, we used the refractive indices of hydrogen silsesquioxane (HSQ) and gold as the dielectric and mirror respectively.

The fourth step was to define an appropriate mesh. We used Lagrange (quadratic) mesh elements [88] in our simulation. In order to maintain accuracy when using periodic boundary conditions, it was necessary to have a denser mesh at one of the edges. We constrained the maximum mesh size at edge XY (see Fig. 6-4) to 1 nm. We also set the maximum element size in the NbN and NbN_xO_y regions to 0.25 nm. Moving to more mesh elements did not improve accuracy.

In the final step, we solved the problem and then performed post-processing to find the reflectance, transmittance, and absorptance. We used a direct, linear solver (UMFPACK) to solve the problem for the spatial distribution of the electric and magnetic fields. It took roughly 15 to 30 seconds per simulation using a 64-bit, AMD Opteron processor (model 252) operating at 2.6 GHz with 6 GB of RAM. We

computed the reflectance R by finding the line integral of the normal, time-averaged power flow on edge YY', subtracting the incident power integrated over the same boundary, and normalizing the result. The transmittance T was found in a similar manner. We computed the absorptance by integrating the time-averaged resistive heating in the NbN region. The time-averaged resistive heating Q_{av} is a predefined quantity in Comsol and is given by

$$Q_{\text{av}} = \frac{1}{2}\text{Re}(\sigma\vec{E}\cdot\vec{E}^* - j\omega\vec{E}\cdot\vec{D}^*) \tag{6.7}$$

where σ is the conductivity, $\vec{E}$ is the electric field, and $\vec{D}$ is the electric displacement. In our simulations, σ is zero so the expression simplifies to:

$$Q_{\text{av}} = \frac{1}{2}\omega\text{Im}[\epsilon]\,|\vec{E}|^2. \tag{6.8}$$

After integrating Q_{av} over the NbN domain, we normalized it to the incident power to get the absorptance, A. Using Q_{av} to find the absorptance was equivalent to using $A = 1 - R - T$, but had the advantage of allowing us to distinguish the absorption that occurred in different materials. We will now present and discuss the simulation results.

6.3 Simulation results

Using the procedure outlined in the previous section, we calculated the dependence of absorptance on five parameters: fill-factor f, pitch p, wavelength λ, film thickness, and cavity thickness. We will now present results that relate the absorptance to each of these parameters.

6.3.1 Dependence of absorptance on pitch and fill-factor

The fill-factor f is the ratio of the wire width w to the pitch p:

$$f = \frac{w}{p}. \tag{6.9}$$

f is sometimes referred to as a percentage.

We will first hold the fill-factor constant and see the effects of varying the pitch on the absorptance. Figure 6-6 shows the dependence of the parallel and perpendicular absorptance as functions of the pitch for constant values of fill-factor. This plot shows that varying the pitch had no effect on the absorption of parallel polarized radiation. We can explain this effect by recalling that a subwavelength grating acts as a film to parallel polarized light. On the other hand, decreasing the pitch while keeping f constant decreases the absorptance of the perpendicularly polarized light. The reason behind this effect is illustrated in Fig. 6-5, where $|E_\perp|$ is plotted across two periods of an $f = 0.5$, 100-nm-pitch grating and is compared to $|E_\perp|$ for a single period of an $f = 0.5$, 200-nm-pitch grating. There are, in-effect, more air-NbN interfaces per unit area for the grating with the smaller pitch than one with a larger pitch, and the boundary conditions dictate a lower field intensity in the NbN for the structure with smaller pitch. A lower field intensity results in a lower value for both Q_{av} (see Eq. (6.8)) and absorptance.

Figure 6-7 shows how the pitch depends on the ratio $A_{||}/A_\perp$. The ratio between $A_{||}$ and $A_\perp$ is largest for small pitch and low fill-factor.

We can also hold the pitch constant and vary the fill-factor. Figure 6-8 shows a plot of absorptance as a function of fill-factor. Because the curves for different pitch values overlap with each other, we need only focus on increasing the fill-factor in order to maximize the absorptance. This plot also emphasizes one additional point, which is that our SNSPDs can only obtain a maximum of around 28% absorptance even if we approached a 90% fill-factor for top illumination.[3] Achieving greater than 90%

[3]For bottom illumination, we can achieve 45% absorption at a 1550-nm-wavelength because of the smaller mismatch in the NbN-sapphire refractive index in comparison to that of air-NbN.

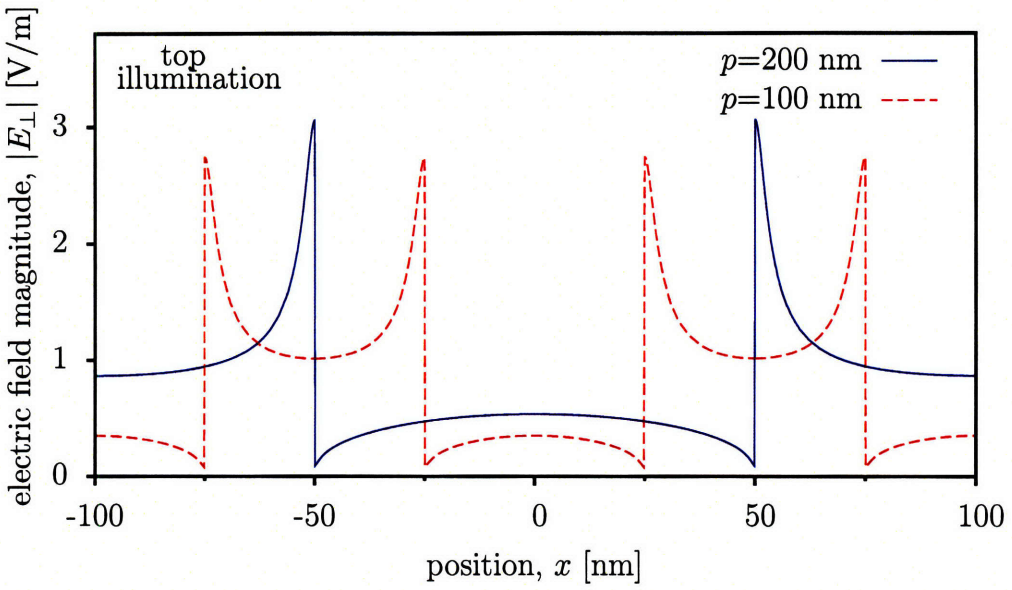

Figure 6-5: Plot of the magnitude of the perpendicular electric field $|E_\perp|$ as a function of position x for one period of a 200-nm-pitch grating and two periods of a 100-nm-pitch grating. The fill-factor f was 0.5 for both curves. The plot shows that $|E_\perp|$ in the nanowire region is lower for $p = 100$ nm than for $p = 50$ nm, leading to lower perpendicular absorptance for a grating with $p = 50$ nm. The cross-section was taken at a height $z = 2$ nm above the sapphire substrate (geometry shown in Fig. 6-4). Parameters of this simulation were: wavelength = 1.55 μm, NbN thickness = 4 nm, oxide thickness = 2 nm, and top illumination. Refractive indices of the materials are given in Table 6.1.

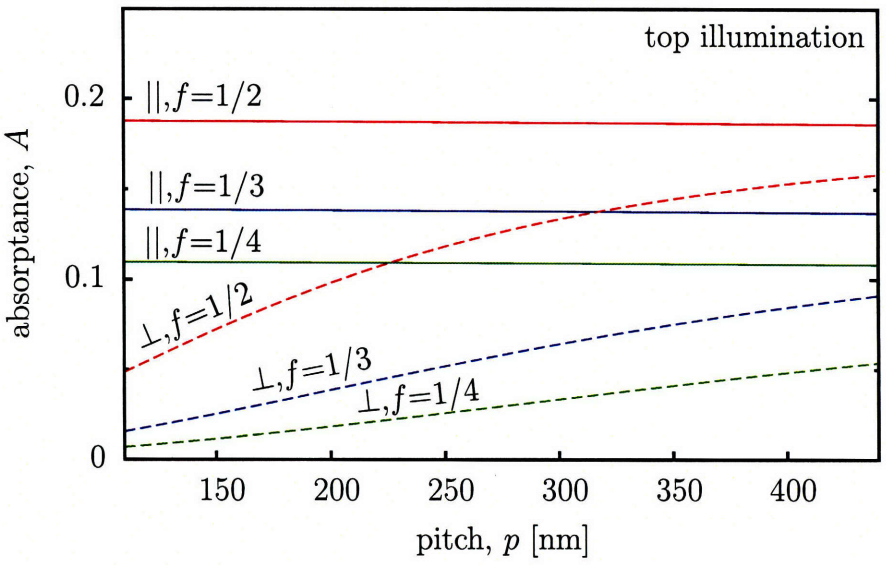

Figure 6-6: Plot of the absorptance as a function of the pitch of the wire grid pictured in Fig. 6-4 for constant values of the fill-factor f. For the same fill-factor, the wire grid is more sensitive to light polarized parallel (||) to the wire grid than perpendicular ($\perp$) to it. Parameters of this simulation were: wavelength = 1.55 μm, NbN thickness = 4 nm, oxide thickness = 2 nm, and top illumination. Refractive indices of the materials are given in Table 6.1.

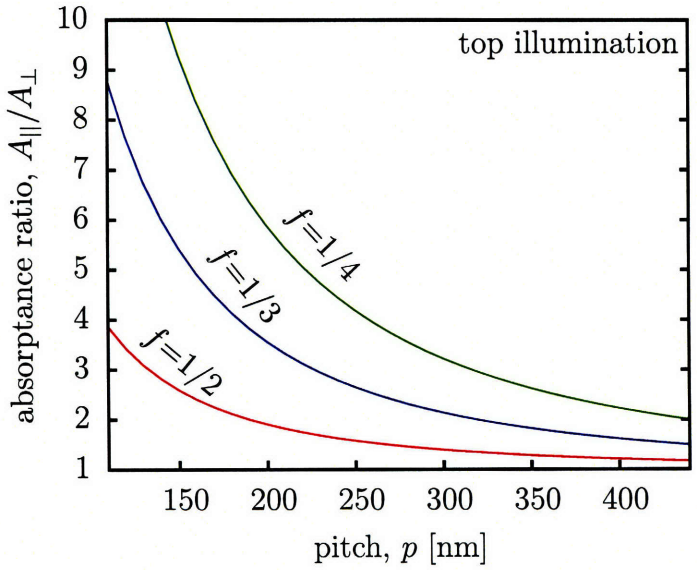

Figure 6-7: Plot of the ratio of parallel (||) to perpendicular ($\perp$) absorptance as a function of the pitch of the wire grid for constant values of the fill-factor f. Parameters of this simulation were: wavelength = 1.55 μm, NbN thickness = 4 nm, oxide thickness = 2 nm, and top illumination. The geometry is shown in Fig. 6-4. Refractive indices of the materials are given in Table 6.1.

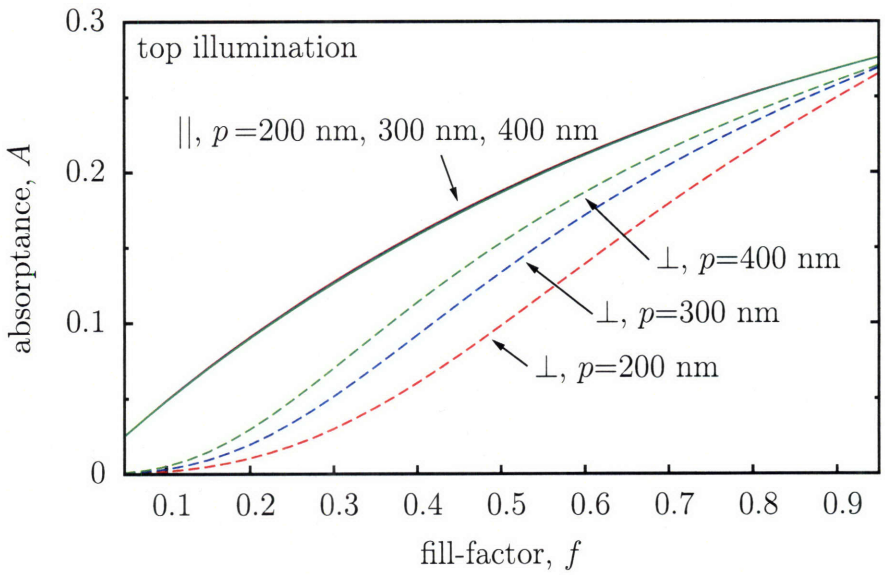

Figure 6-8: Plot of the absorptance as a function of the fill-factor for constant values of the pitch p, and for parallel ($||$) and perpendicular ($\perp$) polarizations. Parameters of this simulation were: wavelength = 1.55 μm, NbN thickness = 4 nm, oxide thickness = 2 nm, and top illumination. The geometry is shown in Fig. 6-4. Refractive indices of the materials are given in Table 6.1.

absorptance will require absorption-enhancing structures such as cavities. We may also be able to enhance the absorption through plasmonic structures.

6.3.2 Dependence of absorptance on cavity thickness

One way to enhance the absorption in the superconductor is to eliminate reflections. Reflections can be eliminated by destructively interfering the transmitted light with the reflected light. Destructive interference is easy to achieve with a mirror that reflects the transmitted light such that it is out of phase with the original reflected light. We fabricated and tested devices with integrated cavities[4] tuned for optimal performance at a wavelength of 1.55 μm [57]. We will now present theoretical results that show how the absorptance depends on cavity thickness and wavelength. We will also show how the wavelength dependence changes as a result of adding a cavity.

[4]We refer to the mirror and dielectric spacer structure as cavity in this thesis and in Ref. [57]. However, we note that the cavity has Q (quality-factor) of ~2-3, so some may disagree with calling such a structure an optical cavity.

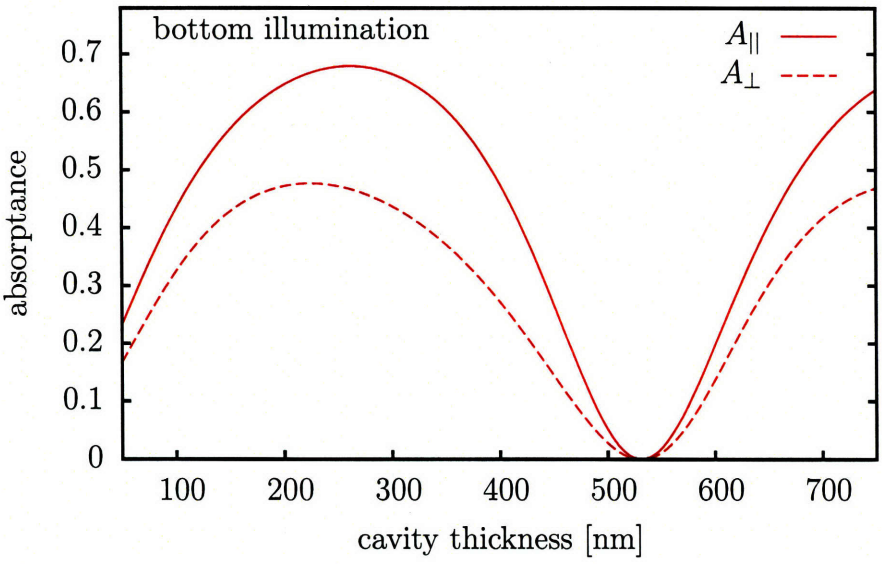

Figure 6-9: Plot of parallel ($A_{||}$) and perpendicular ($A_{\perp}$) absorptance as a function of cavity thickness for a 50% fill-factor, 200-nm-pitch wire grid. Parameters of this simulation were: wavelength = 1.55 μm, NbN thickness = 4 nm, oxide thickness = 2 nm, and bottom illumination. We used the basic geometry shown in Fig. 6-4 with the addition of an optical cavity. The optical cavity consists of an HSQ film and 100 nm gold film on top of the nanowire. Refractive indices of the materials are given in Table 6.1.

First, we will show how the absorptance depends on cavity thickness. An optical cavity consisting of an HSQ film sandwiched between a gold film and patterned NbN can increase the absorptance of an SNSPD by a factor of two to three. However, it is important to use an optimized cavity thickness to achieve maximum enhancement. Figure 6-9 shows the dependence of cavity thickness on the absorptance of a 50% fill-factor, 200-nm-pitch wire grid for a 1.55-μm-wavelength field that back-illuminated the device. This plot shows that a peak of 68% absorptance occurs at a cavity thickness of roughly $\lambda/(4n_{\mathrm{HSQ}})$, while the null occurs at $\lambda/(2n_{\mathrm{HSQ}})$, just as one would expect. The numerical calculations also permit us to see the effect of polarization on the absorptance of a device with a cavity. We can see that a device is roughly 1.5 times more sensitive to parallel polarized light than to perpendicularly polarized light at the maximum.

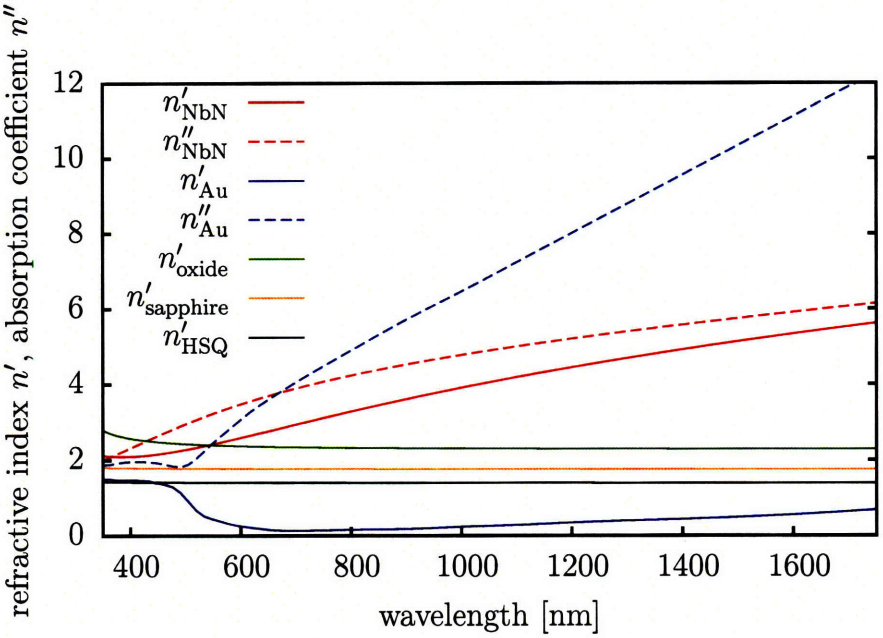

Figure 6-10: Plot of the refractive index (n') and absorption coefficient (n'') as a function of wavelength for the materials used in our simulations [77, 78, 89].

6.3.3 Dependence of absorptance on wavelength

In principle, the wavelength dependence of the absorptance should be negligible if (1) all the dimensions of the simulation geometry are subwavelength, and (2) the indices of refraction of all the materials are constant. Clearly the first point does not hold for all wavelengths: a 200-nm-pitch grating has features that are only $\lambda/3$ when compared to a 300 nm photon. Moreover, the indices of refraction change significantly as a function of wavelength as shown in Fig. 6-10 [77,78,89]. Therefore, it is necessary to perform the calculation at different wavelengths.

We have calculated the dependence of absorptance on the wavelength of the illuminating field by incorporating the wavelength dependence of the refractive index into our model. Our numerical model, unlike effective medium theory, is accurate at both small and large wavelengths. The dependence of the absorptance on wavelength for a number of different gratings is shown in Fig. 6-11. These plots show that the absorptance spectrum of the detectors is relatively broadband.

Adding a cavity has a negative effect on the otherwise broadband spectral charac-

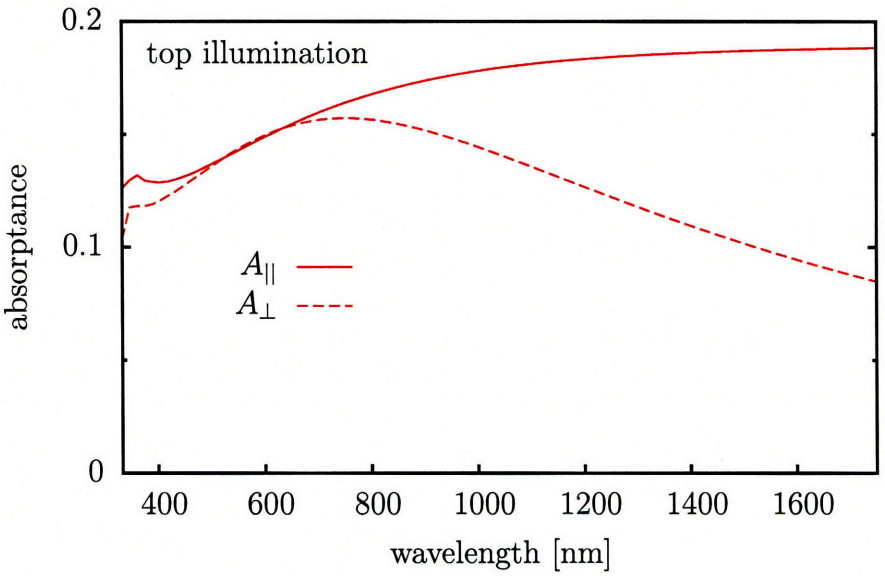

Figure 6-11: Parallel ($A_{||}$) and perpendicular ($A_{\perp}$) absorptance as a function of wavelength for a 50% fill-factor, 200-nm-pitch wire grid. Parameters of this simulation were: NbN thickness = 4 nm, oxide thickness = 2 nm, and top illumination. The geometry is shown in Fig. 6-4. Refractive indices of the materials are given in Table 6.1.

teristics of the absorptance of SNSPDs. In Fig. 6-12, we compare the absorptance of a 50% fill-factor, 200-nm-pitch grating with and without an optical cavity optimized for a wavelength of 1.55 μm. We find that although the cavity enhances the absorptance at one frequency, it decreases the absorptance at other wavelengths.

6.3.4 Dependence of the absorptance on film thickness

Changing the film thickness also has an impact on the absorption of the grating. Figure 6-13 shows the dependence of the absorptance of a 200-nm-pitch, 50% fill-factor grating on the thickness of NbN. We can see that the parallel absorptance saturates to a peak value of 36% for top illumination. This plot also shows that one route to more absorptive devices is to use thicker films, however, the electrical response may be adversely affected for larger thicknesses.

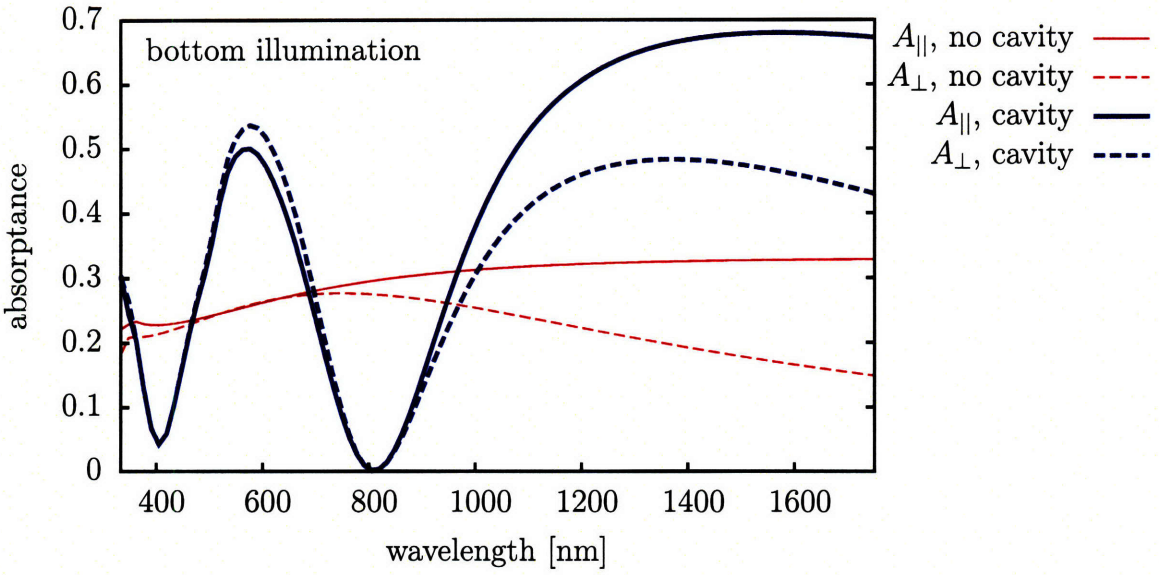

Figure 6-12: Plot comparing the absorptance spectrum for a wire grid with an integrated cavity optimized to 1.55μm to one with a cavity. Parameters of this simulation were: NbN thickness = 4 nm, oxide thickness = 2 nm, pitch = 200 nm, fill-factor = 50%, cavity thickness = 260 nm, and bottom illumination. Refractive indices of the materials are given in Table 6.1.

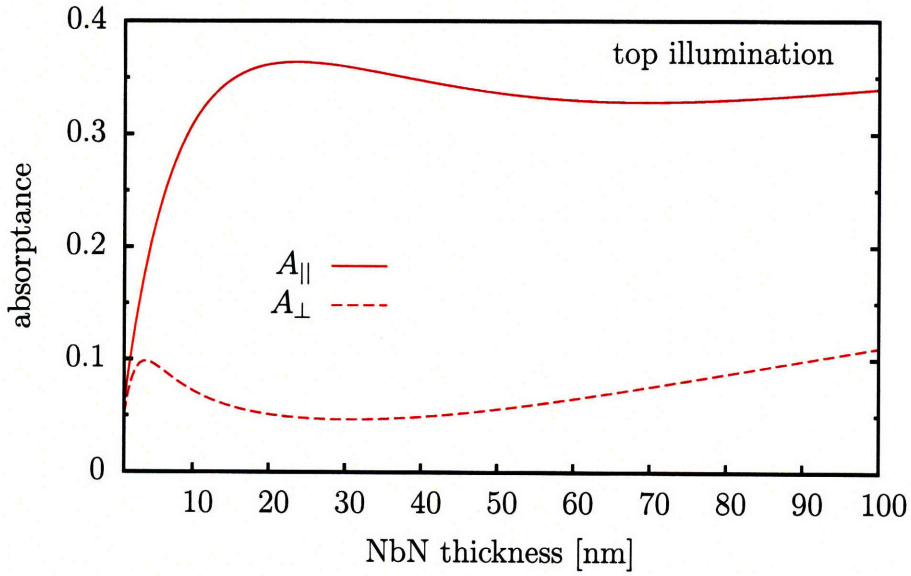

Figure 6-13: Plot of parallel ($A_{||}$) and perpendicular ($A_{\perp}$) absorptance as a function of NbN thickness for a 50% fill-factor, 200-nm-pitch wire grid. Parameters of this simulation were: wavelength = 1.55 μm, oxide thickness = 2 nm, top illumination. Refractive indices of the materials are given in Table 6.1.

6.4 Conclusion

In this chapter, we reviewed the literature on effective medium theory and studied how it relates to our problem. Our review pointed us towards numerical methods such as the finite-difference time-domain method and the finite-element method. We used the finite-element method with a simplified version of our device geometry in order to perform our simulations more efficiently. We simulated the dependence of the absorptance on many geometrical and material parameters.

Our simulation results showed that the absorptance of our structures depended strongly on fill-factor and polarization. Our model predicts that the absorptance can be maximized by constructing high fill-factor devices. High fill-factor devices also exhibit low polarization sensitivity. The addition of an optical cavity can increase the absorptance by a factor of 2-3, but also introduces nodes into the otherwise broadband absorptance-wavelength spectrum.

In the next chapters, we will test our model and its dependence on some of the parameters that can be easily varied, such as fill-factor, pitch, wire width, and polarization. In Chap. 7, we will describe the fabrication techniques we used to make our devices. In Chap. 8, we will describe how we measured absorptance and present results on how the model compares to experiment.

Chapter 7

Fabrication techniques for realizing superconducting nanowire single photon detectors

The procedure for fabricating SNSPDs has been described previously [54, 90], and is summarized in Fig. 7-1. Modifications to this procedure have yielded very narrow nanowires (> 15 nm) through enhancing the etch resistance of our resist [91]. In this chapter, we will describe two new additions to the fabrication procedure. The first addition improved line-width uniformity, while the second aided in diagnostics for fabrication and testing. We will also present our fabrication results.

We will first present a proximity-effect correction technique that achieves linewidth uniformity. This proximity-effect technique is different from the technique developed previously for these detectors [54] in that it does not require pre-processing to yield good results.

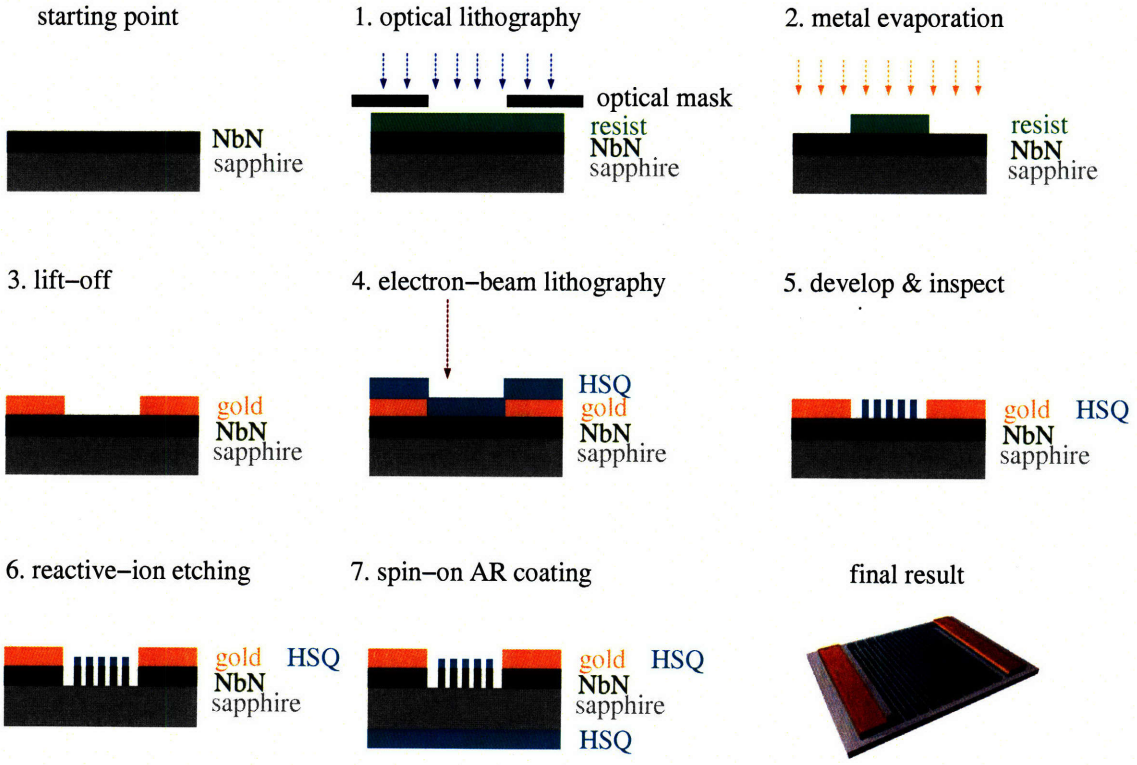

Figure 7-1: Schematic illustrating the fabrication procedure for realizing SNSPDs. Gold contact pads are formed in steps 1-3. Steps 4-6 define the nanowires that form the active region of the SNSPD. In the final step, an antireflection coating is applied to the back of the sapphire wafer. Details of this fabrication procedure can be found in Refs. [54, 90].

7.1 Pre-processing-free proximity-effect correction

7.1.1 Introduction to the proximity-effect

In electron-beam lithography, electrons are accelerated and focused onto a small spot (typically 1 to 2 nm) on a resist. A pattern can be defined by moving the spot to other locations and controlling the electron dose delivered at each location. The deposited electrons, if above some threshold dose, cause a chemical reaction to occur in the resist that either improves (for a negative resist) or degrades (for a positive resist) the solubility of the resist in a solvent. However, electron scattering caused by atomic nuclei in the resist and substrate causes electrons intended for one location to transfer energy to resist in a nearby location. This effect is known as the proximity effect.

The proximity effect can cause features in an intended pattern to be distorted after the resist is developed. The relationship between the intended pattern $I(x, y)$ and the resulting output pattern $O(x, y)$ is given by

$$O(x, y) = I(x, y) * P(x, y) \tag{7.1}$$

where $*$ denotes a convolution, and $P(x, y)$ is the point-spread function specific to the materials and geometry. $P(x, y)$ can be modeled as the sum of two Gaussians:

$$P(x, y) = \frac{1}{\pi(1+\eta)}\left(\frac{1}{\alpha^2}e^{-(x^2+y^2)/\alpha^2} + \frac{\eta}{\beta^2}e^{-(x^2+y^2)/\beta^2}\right), \tag{7.2}$$

where α, β, and η are parameters related to electron scattering [92]. Techniques that circumvent the problems posed by the proximity-effect are known as proximity-effect correction techniques. Countering the proximity-effect is essential to realizing efficient SNSPDs.

For optimal operation and uniform detection efficiency throughout their active area, SNSPDs require uniform line widths. This is because the critical current of an SNSPD is set by the widths of the narrowest wire or segment of a wire (assuming the

wire thickness is constant across the device). The wider regions of the nanowire will be biased further away from the critical current and may not respond as effectively to incoming photons as do narrower sections of the nanowire.

Previously, we used so-called dummy features, such as boxes, that had the sole function of equalizing the electron dose for wires in the active area of the detectors [54, 90]. However, arriving at the appropriate parameters for the dose and size of the dummy features required numerical calculations and some guess-work, because the true point-spread function was not known. While measuring the point-spread function is possible [92], it is labor-intensive and can drift with a change in the process, materials, or exposing conditions.

7.1.2 Our approach

We will now describe a different technique that achieves a uniform electron dose for the nanowires in the active area of our SNSPDs. Our technique relies on the fact that a large grating has a region in its center that has a uniform dose. We can make this region the active area of the SNSPD by shorting adjacent wires in the grating. We show this schematically in Fig. 7-2(a-b). Close attention must be paid to the symmetry of the pattern because any asymmetry can distort the central uniform-dose region of the SNSPD.

Performing proximity-effect correction in this way affords a number of advantages. First, because the dose is guaranteed to be uniform at the center of a grating, we do not need to perform pre-processing. Second, this method can be trivially extended to different resists, resist thicknesses, and substrates. Third, this method can be used to realize even larger active area detectors than we have shown in this thesis, so long as there is sufficient room around the detector for the proximity-effect correcting structures.

We will now show that our design is able to create a uniform dose profile in the active-area region of our SNSPDs. We will assume a point spread function defined by Eq. (7.2) with $\alpha = 0.01$ μm, $\beta = 2.44$ μm, and $\eta = 0.5$ [93]. The point-spread function defined by these parameters is by no means the true point-spread function

(a) input

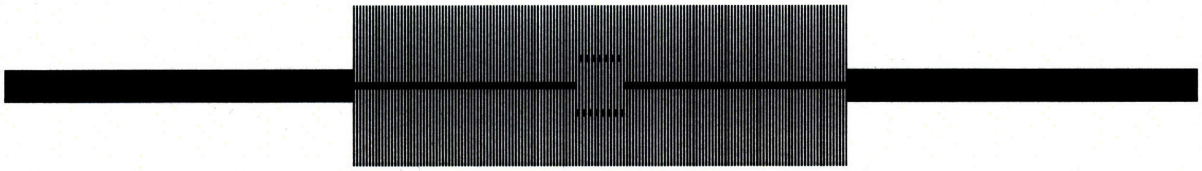

(b) active area

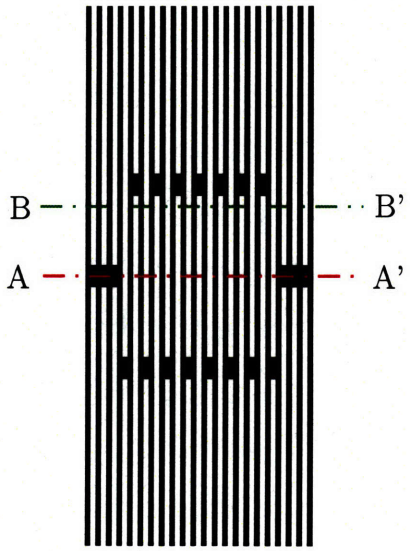

(c) after convolving with point-spread function

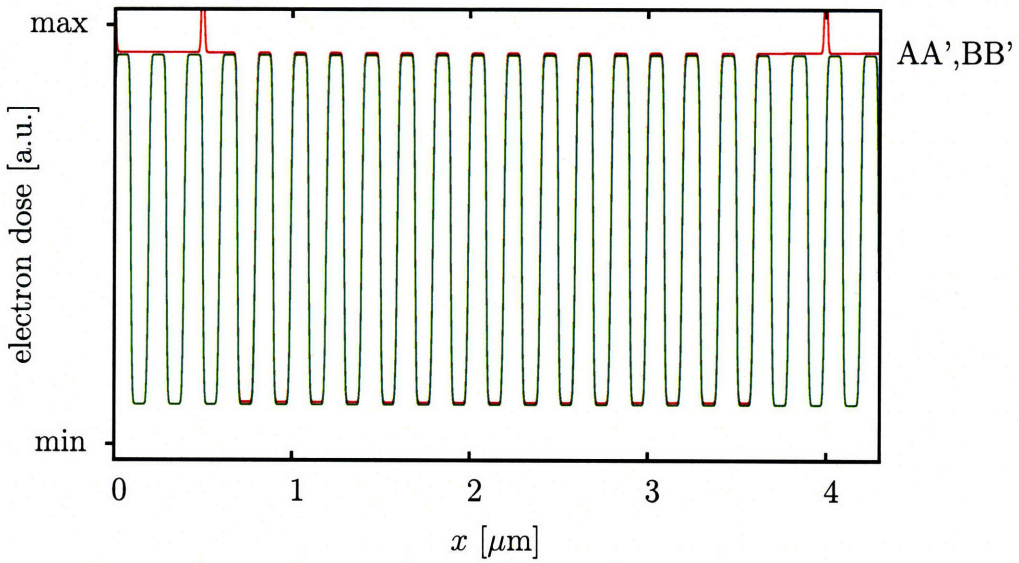

Figure 7-2: Layout of a 50% fill-factor, 200-nm-pitch SNSPD *with* proximity-effect correcting structures. The layout of the entire SNSPD is shown in (a) with a magnified view of the active area shown in (b). A plot of the electron doses at the cross-sections pictured in (b) after the proximity-effect is taken into account is shown in (c). The cross-sections show that the electron doses are identical for both sections AA' and BB' in the active area region.

for our process, but is a reasonable estimate and will serve to emphasize the generality of our approach. We will compute the output dose $O(x, y)$ in Eq. (7.1) for two input functions. The first input function is shown in Fig. 7-2(a) and includes an extended grating structure that will lead to a uniform dose in the center. The second function is shown in Fig. 7-3(a) and does not have any proximity-effect correcting features. We have used a constant electron-dose for both of these input functions.

The resulting output patterns for each of these input patterns are shown in Figs. 7-2(c) and 7-3(c), where the cross-sections at the center and near the edge of the active area have been plotted. A comparison of these two plots shows that the proximity-effect correcting features enable a more uniform dose at the edges and in the center in comparison to a device without proximity-effect correcting features.

We used this proximity-effect correcting method to fabricate SNSPDs that were used to test the results of Chap. 6. Figure 7-4 shows scanning electron micrographs of the structures that we fabricated. After several iterations involving small design changes, we fabricated a chip containing 45 instances of each device (225 devices per chip).

7.2 Automated chip imaging

In the past, one of the problems we noticed when testing the detection efficiency of chips with hundreds of devices was how to explain anomalous observations, such as short-circuited devices or a variation of critical-currents across a chip. To improve the diagnostics of problems such as these, we decided to include a step in the fabrication process where we obtained images of every device on the chip. We will now describe this step in more detail.

Because obtaining hundreds of electron micrographs manually can be laborious, we used the Raith 150 electron-beam lithography tool to automatically image every device on our chip. We performed the imaging step after the HSQ was developed rather than after the NbN was etched because we obtained better image contrast. Images taken after the NbN was etched had lower contrast but did not otherwise

(a) input

(b) active area

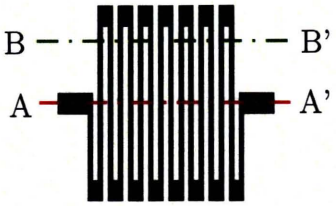

(c) after convolving with point-spread function

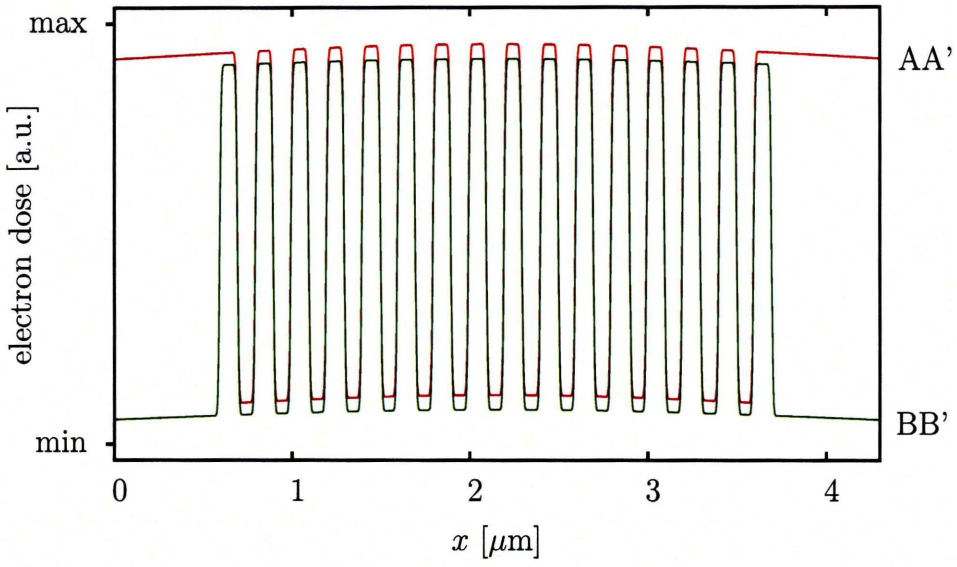

Figure 7-3: Layout of a 50% fill-factor, 200-nm-pitch SNSPD *without* proximity-effect correcting structures. The layout of the entire SNSPD is shown in (a) with a magnified view of the active area shown in (b). A plot of the electron doses at the cross-sections pictured in (b) after the proximity-effect is taken into account is shown in (c). The cross-sections show that the electron doses are not uniform across the active area.

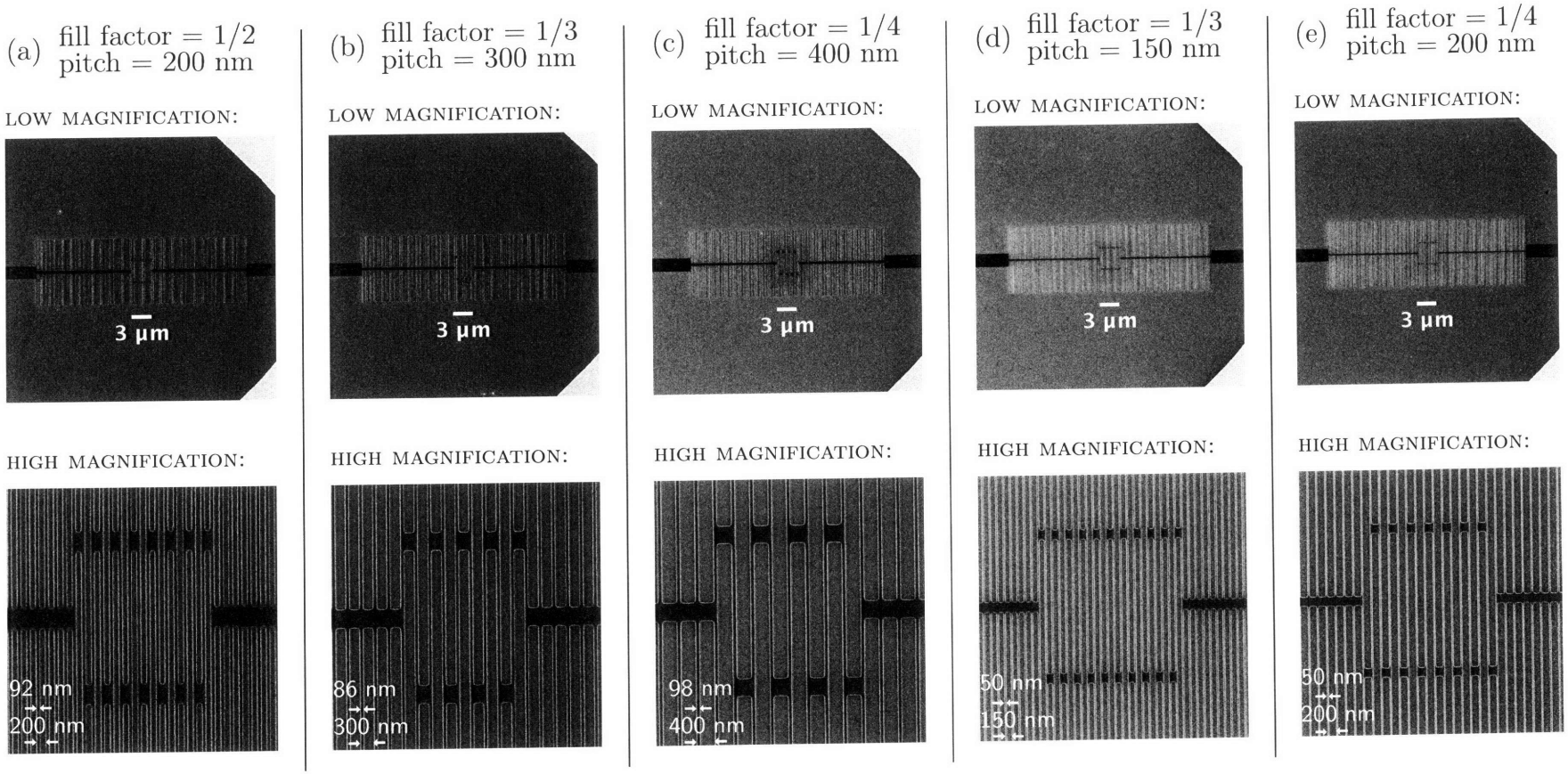

Figure 7-4: Scanning electron micrographs of SNSPDs with different values of fill-factor and pitch. We used these devices (and others identical to them) to check whether the numerical model presented in Chap. 6 was correct.

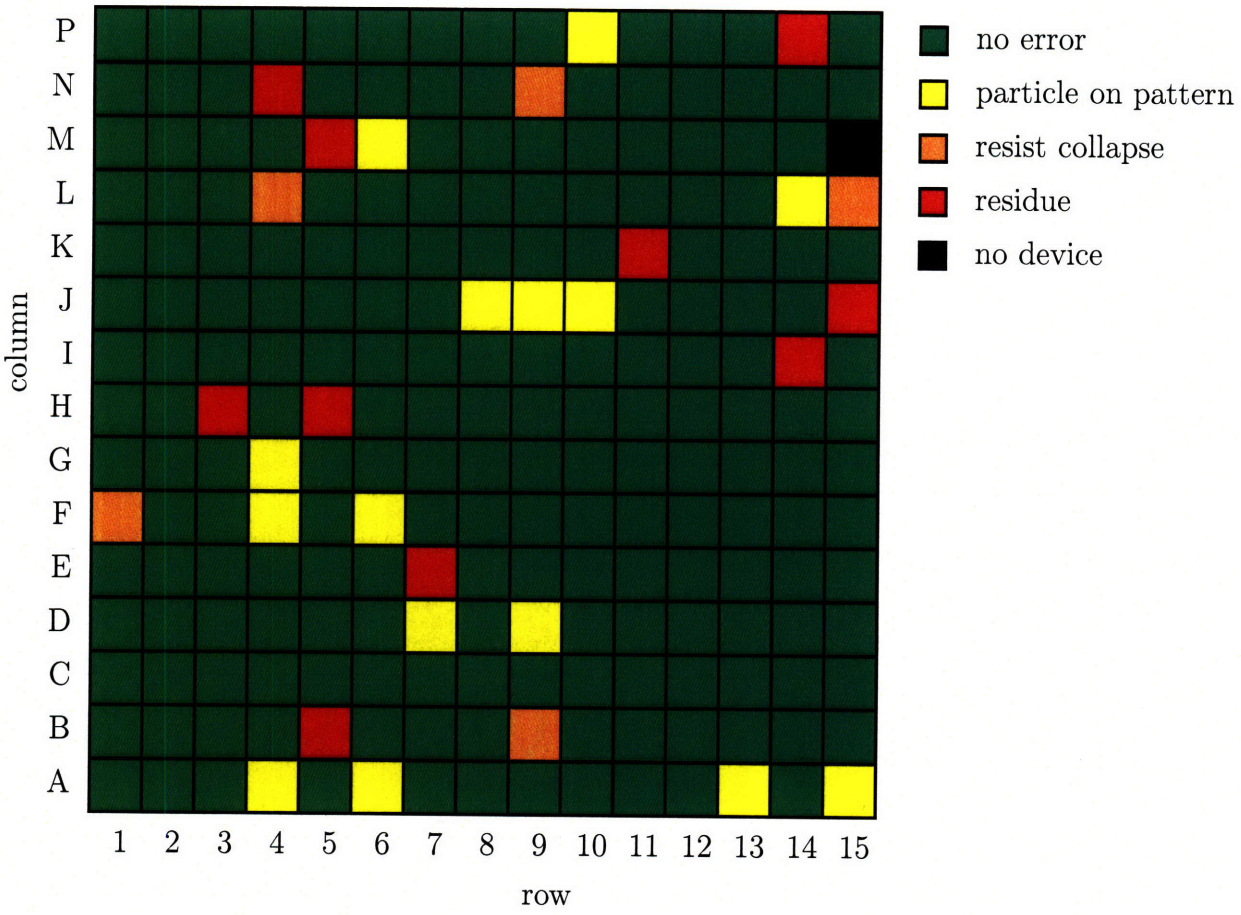

Figure 7-5: Map of the visible defects on our devices across a chip with 225 devices. This plot shows that most of the devices yielded with no visible defects, and that defects were randomly scattered across the chip.

display any visible differences.

The following procedure was used to image our devices. We calibrated the write-field at two different magnifications to ensure that we recorded images that had calibrated dimensions. We also aligned the stage to our layout file. The Raith 150 was programmed to move to the center of a device, where it took two images, each with a different magnification, before the stage was moved to the next device.

We used the images to study the yield of the fabrication process up to the electron-beam lithography step. Figure 7-5 shows a map indicating the precense or absence of defects on every device on the chip. Defects existed on 31 out of 225 devices (13.8%) and were randomly scattered over the chip. The vast majority of devices yielded with no visible defects. A sampling of the devices that had defects is shown in Fig. 7-6.

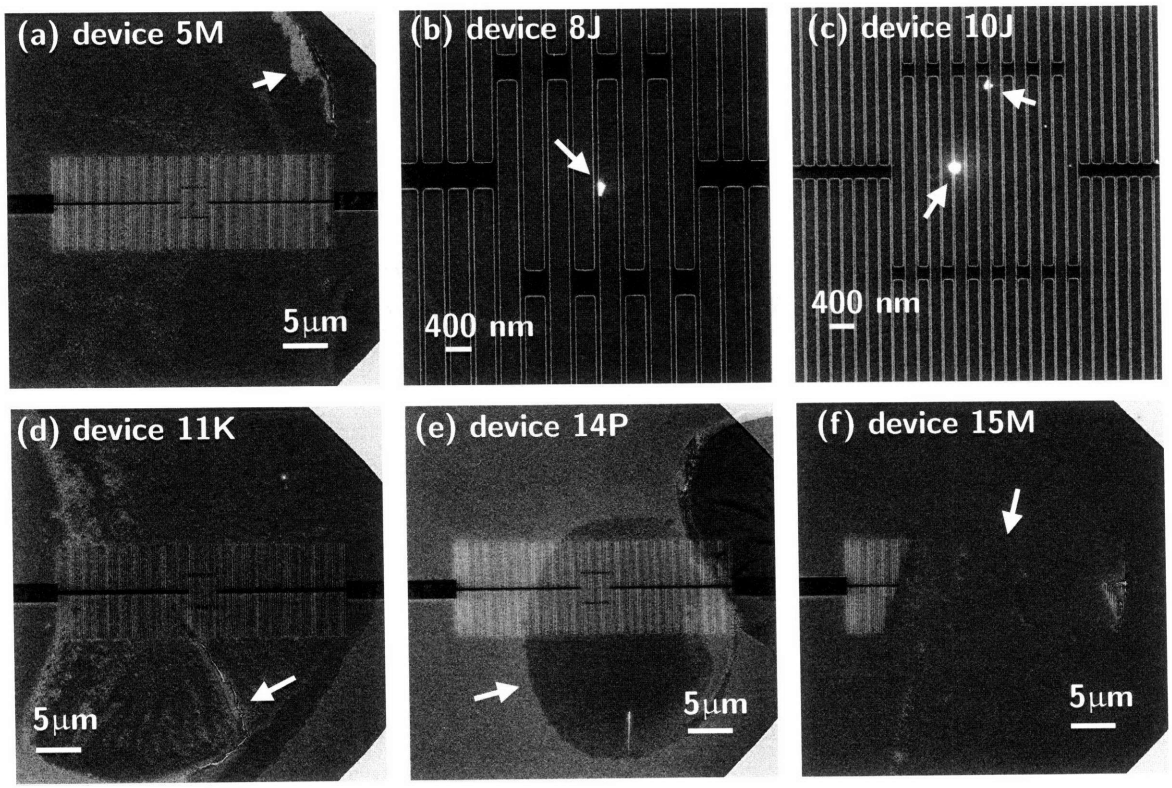

Figure 7-6: Scanning electron micrographs of SNSPDs taken by automating the imaging process. The arrows indicate flaws in the fabrication processes.

While these images were useful in pointing out imperfections in the fabrication process, there were some things that the images did not show. For example, we suspected some devices to have constrictions because they had anomalously low critical currents and detection efficiencies. We could not correlate a constriction in the pattern, such as irregular line width variations, to poor detection efficiency. The lack of visual evidence led us to believe that constrictions were caused by irregularities in the microscopic structure of the superconductor or because of film thickness variations [94].

7.3 Conclusion

We have presented two new additions to the fabrication process of SNSPDs. These additions resulted in simple proximity-effect correction in one case and better diagnostics in the other. In the next chapter, we will describe the way we set up an optical apparatus for measuring absorptance. We will also compare measurements of absorptance to detection efficiency measurements of the same devices.

Chapter 8

Measuring the absorptance of superconducting nanowire single-photon detectors

In this chapter, we will describe how we measured the optical absorptance of our SNSPDs. We will compare our measurements of optical absorptance to the modeling results obtained in Chap. 6. We will also compare our measurements of the absorptance to the detection efficiency measurements of the same devices.

We will first describe the design criteria for an optical setup for measuring absorptance.

8.1 Optical setup for measuring absorptance

8.1.1 Design criteria

We had a number of design criteria for an apparatus that could measure absorptance. The first criteria was that the setup should be able to measure absorptance of actual devices rather than dummy structures so that we could directly compare the measured absorptance to detection efficiency of the same device. Second, we wanted the apparatus to have the ability to measure the absorptance for cold devices (at 2-8 K).

The reasoning behind this criteria was that we may want to investigate how the refractive index changes with temperature. Third, we wanted to be able to measure the polarization sensitivity of our devices. We kept these three design criteria in mind when constructing our apparatus.

We will now describe the optical apparatus used to measure the absorptance in detail.

8.1.2 Apparatus design

Figure 8-1 shows a schematic of the optical apparatus. Free space optics were attached to a three-axis, computer-controlled stage (motorized actuator: Newport LTA-HS, motion controller: Newport ESP300). The stage could be affixed to a cryostat specially designed to allow free-space optical coupling to a cold sample, or be used without a cryostat for room-temperature measurements as shown in Fig. 8-2. We mounted a single-mode optical fiber (Corning SMF-28) to the stage that was illuminated by a 1.55-μm-wavelength diode laser (Thorlabs S1FC1550) and polarized using a state of polarization (SOP) locker (Thorlabs PL100S). By interfacing the SOP locker to a computer, we were able to change the polarization in software without mechanically perturbing the setup. The polarized light was collimated and split equally into two arms. In one arm, a Ge-based sensor (Thorlabs S122A) connected to a power meter (Thorlabs PM100) was used to measure the incident light intensity, mainly for troubleshooting purposes. In the other arm, a long-working-distance microscope objective (Mitutoyo M Plan APO NIR 20X) was used to focus the light into a tight spot onto a device. Light reflected from the device was collected and measured using another power meter. The transmitted light was measured by a third power meter. We controlled the power meters, SOP locker, and motion controller using the Instrument Control Toolbox (ver. 2.4) for Matlab (ver. 7.2/R2006a) and custom written software. The software was designed to make measurements of the reflected and transmitted power over discrete points in a line (line-scan) or an area (raster-scan). A CCD camera (Moticam 1000) was used to find and roughly align the laser to the devices. The camera was accessed by using a flip-mirror placed in between the beam-splitter and

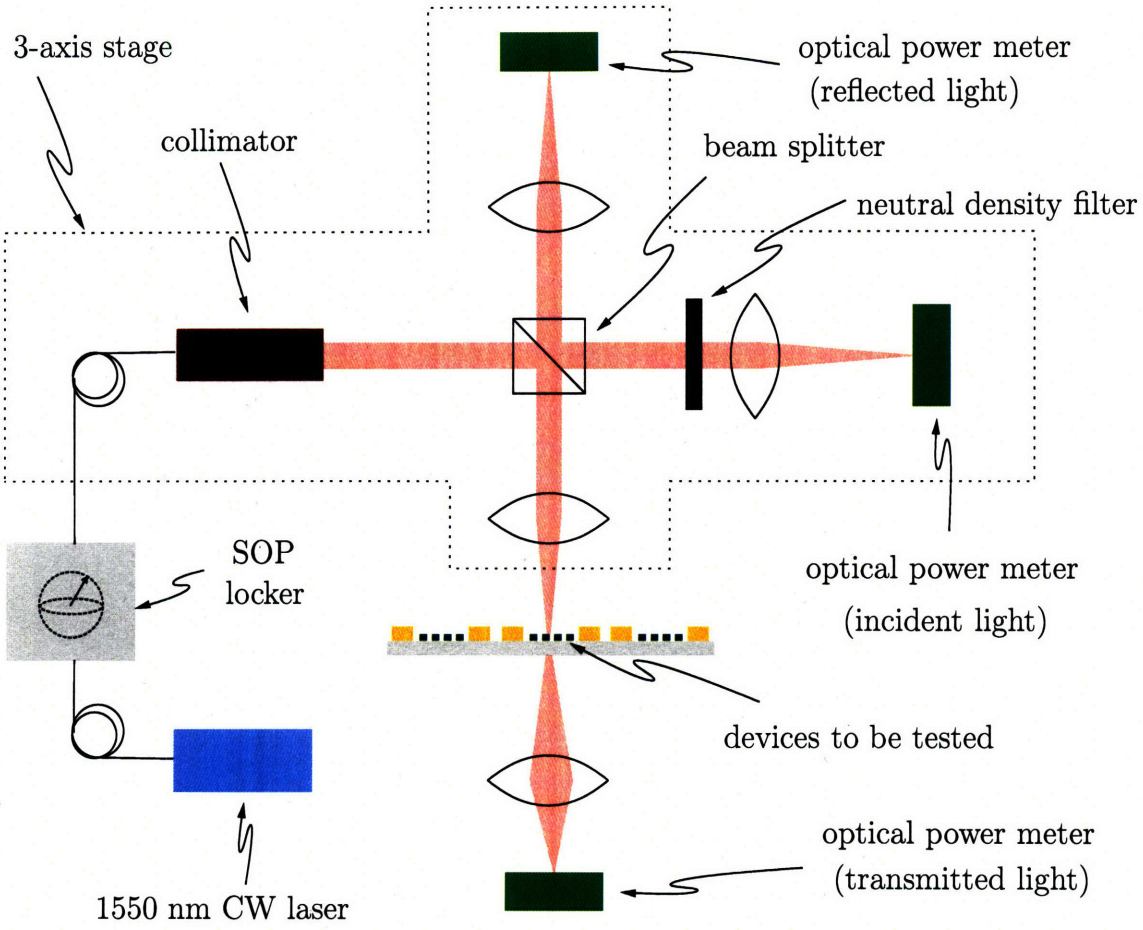

Figure 8-1: Schematic of the optical setup used to measure the optical absorptance. A state of polarization (SOP) locker was used to set the input polarization of the incident 1.55-μm-wavelength light. Light was focused to a 4 μm spot onto a device and the incident, reflected, and transmitted power were measured. The absorptance was calculated from these measurements and earlier calibrations.

microscope objective at a 45° angle.

Before we describe how we made measurements of absorptance using our setup, we will describe the software design and some design challenges we faced when constructing our apparatus.

8.1.3 Software design

It was important to write software on a platform that could control and read-out our instruments efficiently. We looked for a platform that was easy to use, let us perform complex computation for data processing and visualization, and could be easily

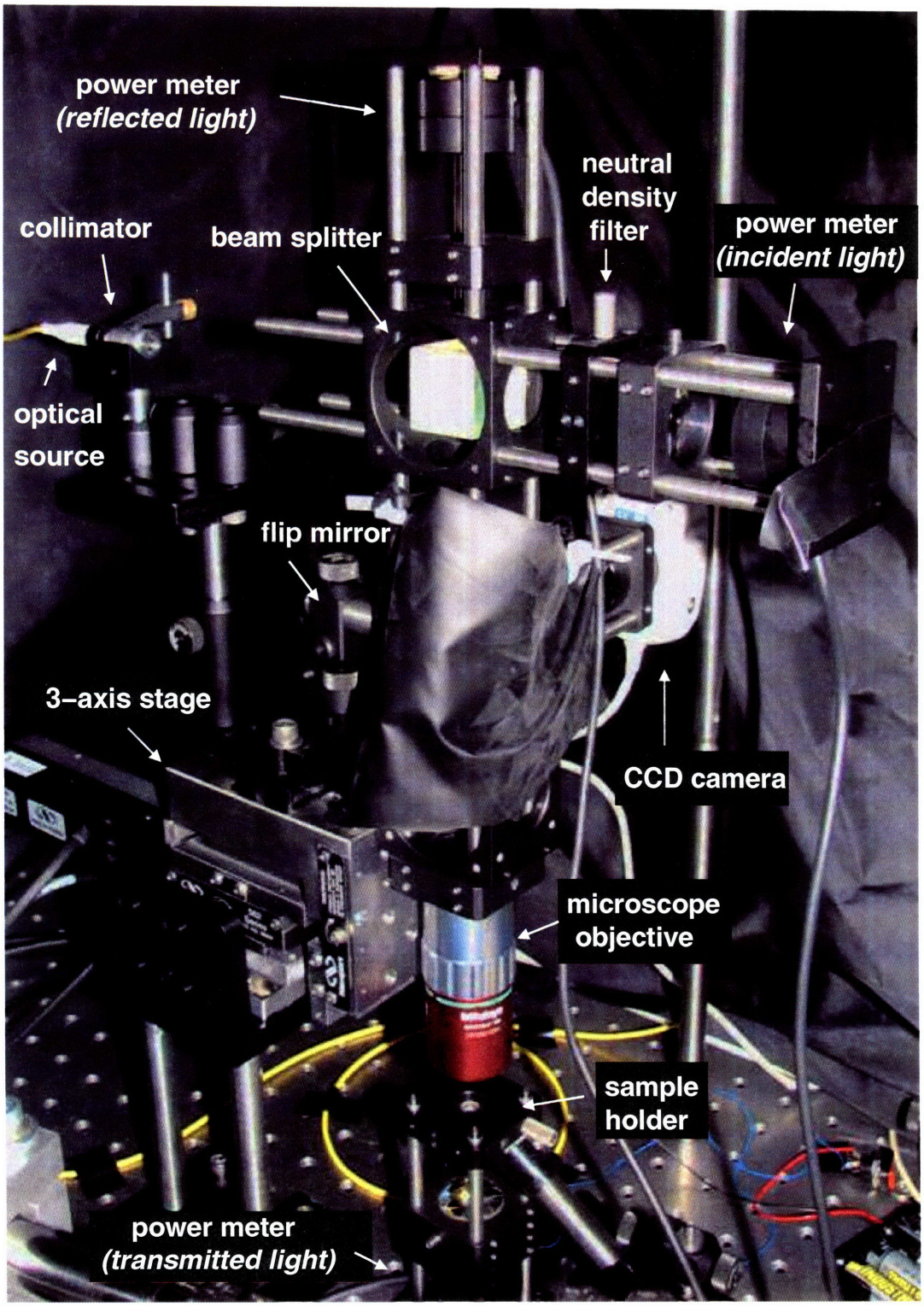

Figure 8-2: Image of the setup used to measure optical absorptance at room temperature.

maintained by future users of the setup. We investigated two options: LabView (National Instruments) and Matlab with the Instrument Control Toolbox (Mathworks). Both software packages were capable of communicating with the motion controller (that used a GPIB interface), and power meters (that used serial interfaces). We chose Matlab over Labview because Labview can be difficult to maintain in the long run. However, most manufacturers do not provide drivers and software support for their instruments to be used through Matlab, so we had to develop our own software routines. We wrote software routines to perform many tasks such as stage movement, line-scans, raster-scans, and saving data to file. Figure 8-3 shows the graphical user interface that was developed to control the stage, SOP locker, power meters, and to visualize the data.

Controlling the SOP locker presented a software challenge, because the manufacturer only supplied a binary library and prototype function files written in the C programming language. The first method we tried was to use Matlab's C compiler (`mex`) to compile an executable so that we could call it directly through Matlab, as if it were any other m-file. This method did not work because the library functions required pointers to be returned, and Matlab does not support pointers to be returned from functions. Another option was to call an executable (created using a different compiler) that took a target polarization as input. While this method worked, it was not efficient because the SOP locker driver has an initialization routine that took approximately 5 seconds each time the executable was run. Since we made measurements along more than 700 points on the Poincaré sphere per device, the initialize route added almost an hour to our measurement routine, which was unacceptable. We opted for a third alternative, in which we used a program that could simulate keystokes (AutoIt ver. 3.2) to communicate with a program written in C that required keyboard input to set the target polarization. This way we only needed to run the initialize process once, and subsequent commands to set polarization we executed in roughly 500ms.

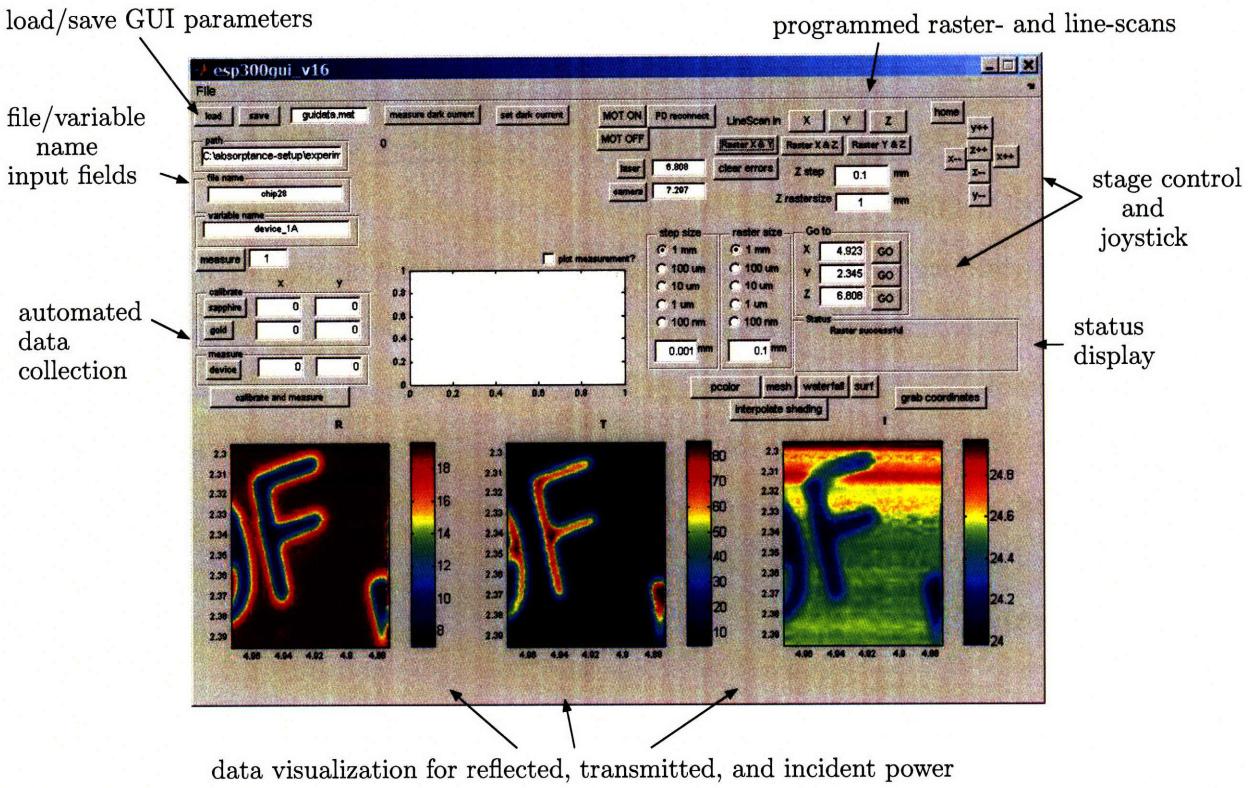

Figure 8-3: Screenshot of the graphical user interface (GUI) developed in Matlab to control the different instruments and make measurements. The screenshot shows raster-scans of reflected, transmitted, and incident power of features on a chip. We notice that the reflected and transmitted power are inverses of each other. The incident power mirrors the reflected power because some of the reflected light is scattered to the incident power meter from the reflection power meter.

8.1.4 Mechanical problems

There were two different mechanical problems that we faced when constructing the absorptance measuring setup. The first problem resulted from mechanical vibration in an earlier design. In that design, the polarization was changed using a linear polarizer and $\lambda/2$-wave-plate mounted to the motion stage. Every time we changed the polarization, the stage experienced an arbitrary shift of a few micrometers. We needed a solution where we did not need to touch the stage to change the polarization. The SOP locker provided that solution, however, the polarization could rotate in the patch of fiber after it exited the SOP locker and before it entered free space (the SOP locker was not compatible with a polarization maintaining fiber). A rotation of the

polarization in this way did not affect our results because we found the minimum and maximum absorptances after taking measurements over the entire Poincaré sphere rather than at specific points.

The second mechanical problem manifested when we noticed that a line-scan in one direction did not produce the same result as a line-scan in the opposite direction for the same absolute stage coordinates. The problem occurred because the drive screw in the motorized actuators incurred a small positional offset when the actuating direction was reversed. We countered this problem in two ways. First, we programmed line-scans and raster-scans to only scan in one direction. Second, we translated the stage to a coordinate that was 50 μm to the top and left of the target location before driving it to the target location. This way, the stage was always driven in the same direction when driving to a coordinate.

We will now describe how we made measurements of absorptance using our setup.

8.1.5 Measurement and calibration procedure

The first step was to measure and calibrate the dark current on each power meter. Second, we placed a chip with the NbN side facing up into the chip holder for doing room-temperature measurements. The bottom surface of the chip had an antireflection coating for calibration purposes.[1] The third step was to bring the laser into focus. To do this, we found an edge (e.g. the edge of a gold pad) and performed a raster-scan in the x-z direction (x = in-plane, z=out-of-plane). We then analyzed the image and found the z position where we obtained the sharpest image. A sample raster-scan near an edge is shown in Fig. 8-4. Figure 8-5 shows that the minimum spot size we were able to obtain had a full-width at half-maximum (FWHM) of 4 μm.

The next step was to find a device. We used a CCD camera to roughly align the laser to the device. We were able to roughly align the laser to within 10 μm of the center of the device by comparing images taken by the CCD camera and a raster-scan. An example of the images we compared is shown in Fig. 8-6. We then used the focused laser beam to finely align the laser to the center of a device (with 1

[1]The procedure for applying an anti-reflection coating is given in Ref. [57].

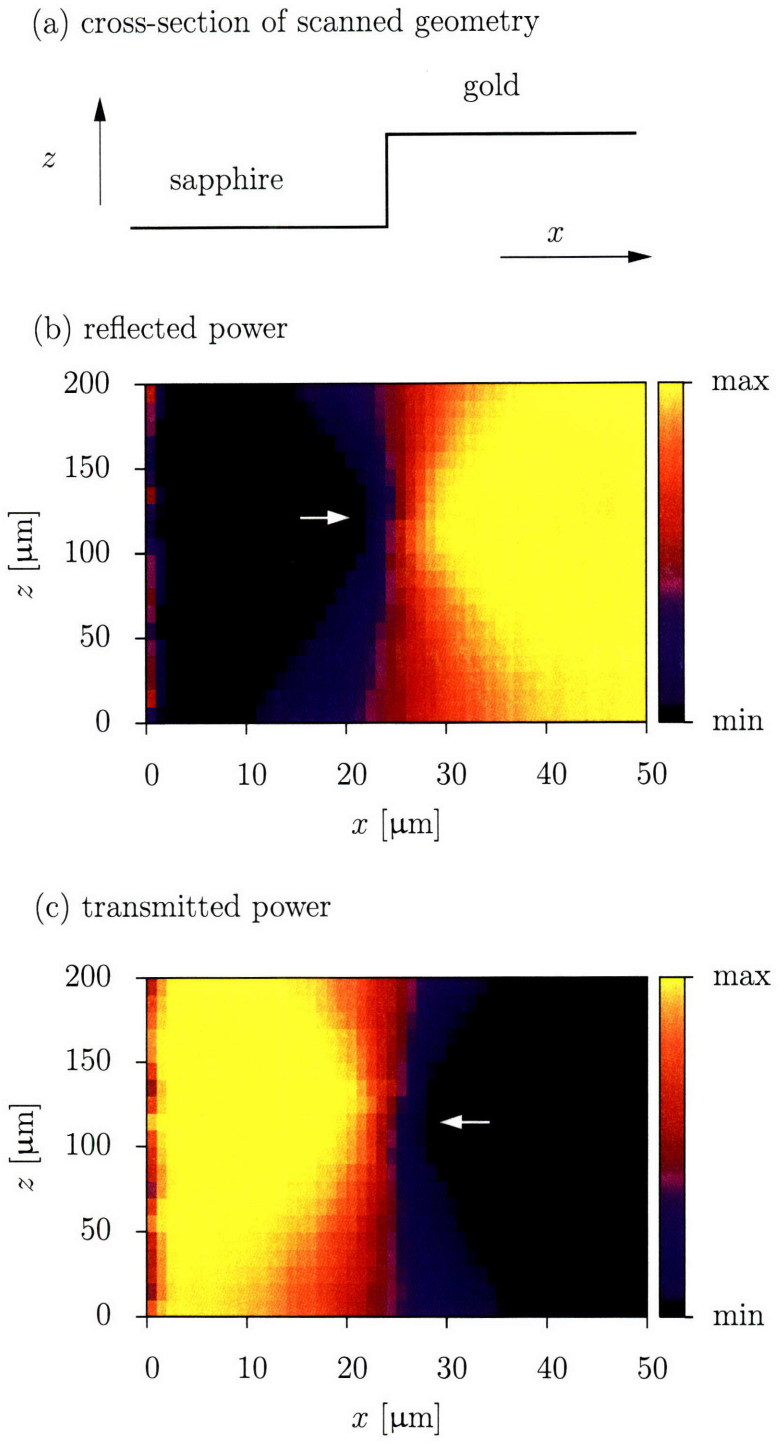

Figure 8-4: Plot of the reflected and transmitted power when the laser was scanned through an edge at different elevations. A raster-scan like this was used to find the focal point. A schematic of the geometry that we scanned through is shown in (a). Gold had higher reflectivity and lower transmissivity than sapphire. (b) and (c) show the results of a raster-scan through this geometry. The white arrows in (b) and (c) show the position at which the edge was sharpest.

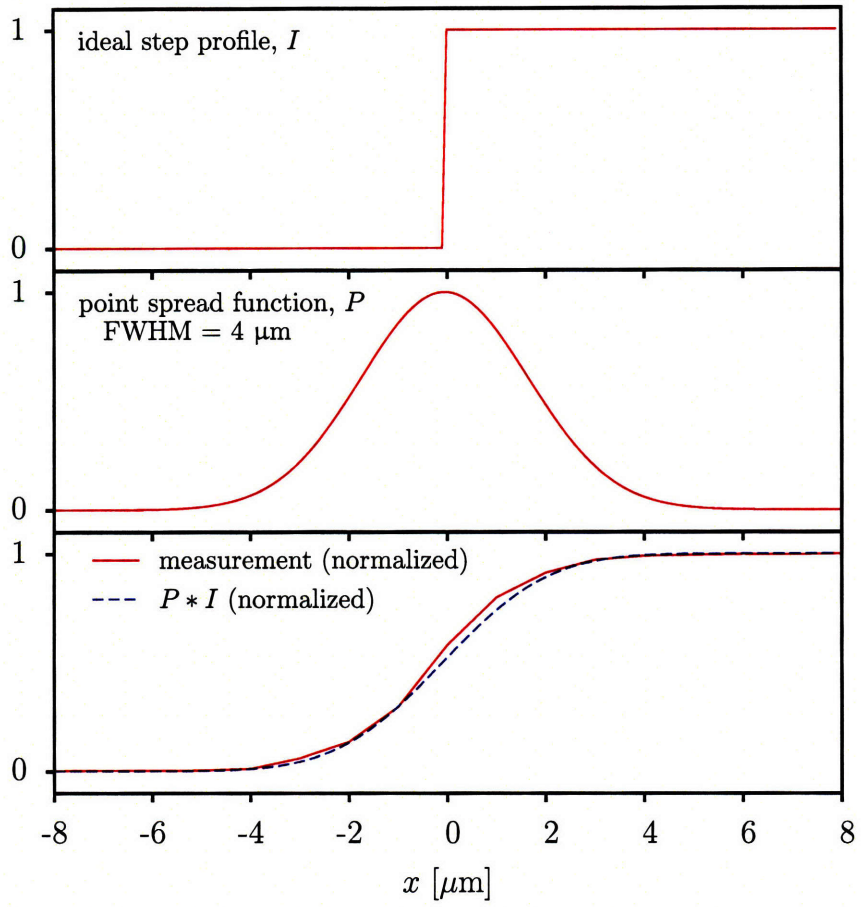

Figure 8-5: This figure shows how the laser spot size can be calculated from a line-scan. We can convolve an ideal edge I (top) with a point-spread function with a 4 μm full-width half-max (middle). The point-spread function is given $P(x) = e^{-x^2/(2\sigma^2)}$ where $\sigma = \frac{\text{FWHM}}{\sqrt{8\ln(2)}}$. The result closely matches the actual measurement of the reflected power at an edge.

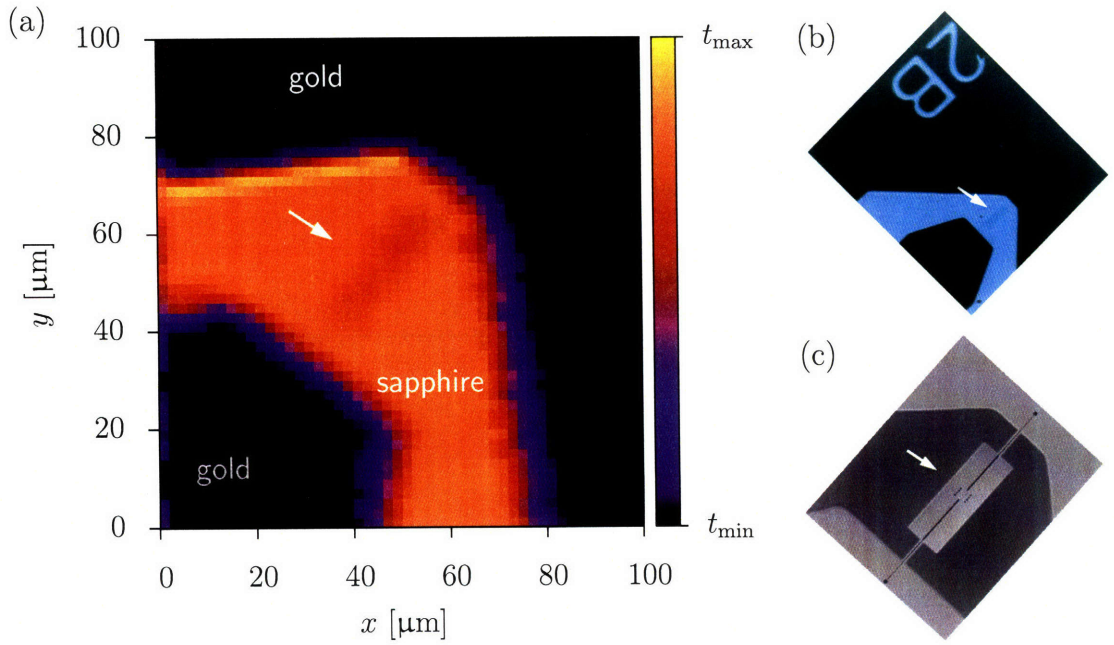

Figure 8-6: One of the problems we faced was how to identify the location of specific devices. We used a CCD camera to identify and roughly aligned to the device of interest. However, in order to roughly align to a device, we needed to make sure that we knew where the laser spot was in relation to an image taken by the CCD camera. To find the laser spot, we first took an image by rastering the laser in a region. We then compared this image to an image of the chip taken through the microscope objective using a CCD camera and noted on the computer monitor where the laser was located in the CCD image. This procedure only needed to be performed once.

μm accuracy).

The next step was to take measurements of the reflected (r) and transmitted (t) power, and obtain the reflectance (R), transmittance (T), and absorptance (A) after proper calibration. We took a line-scan so that gold, sapphire, and the device were imaged, as shown in Fig. 8-7. The locations of gold, sapphire, and the device were inputted into the software. The software directed the stage to move to each location and measure the reflected and transmitted power for polarizations spaced by 10° on the Poincaré sphere. We obtained the reflectance of the device R_d by assuming that $R \propto r$ and that the measurements of the reflected power at gold r_g corresponded to a reflectance of $R_g = 0.98$, while the measured reflected power at sapphire r_s corresponded to $R_s = 0.07$. To relate the transmitted power t_d to the transmittance

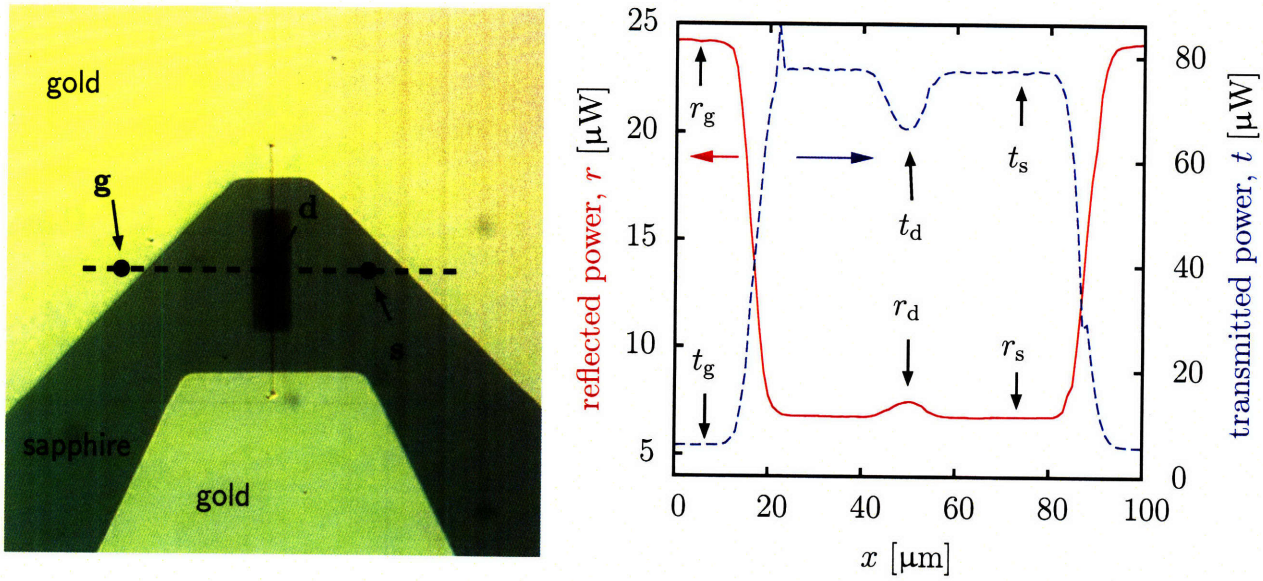

(a) (b)

Figure 8-7: Image of a 33%-fill-factor, 300-nm-pitch device fabricated on sapphire and electrically connected to gold pads is shown in (a). Also pictured in (a) is the trajectory of a line-scan that passes through the device **d**, gold **g**, and sapphire **s**. A plot of the reflected (left axis) and transmitted (right axis) power as a function of distance is shown in (b). Measurements of reflected and transmitted power at gold (r_g, t_g) and sapphire (r_s, t_s) were used to calibrate the reflected and transmitted power at the device (R_d, T_d), and find the reflectance R_d, transmittance T_d, and absorptance A_d.

of the device T_d, we assumed $T_g = 0$ and $T_s = 0.93$. The calibration procedure is graphically shown in Fig. 8-8 for the data shown in Fig. 8-7.

An example of the (uncalibrated) reflected and transmitted power as a function of polarization is shown in Fig. 8-9 for a 50%-fill-factor, 200-nm-pitch device. Two measurement artifacts can be seen in these plots: multiple maxima in plot of reflected power from the device, and a polarization dependence in the reflected and transmitted power from gold and sapphire. We attributed both of these measurement artifacts to the polarization sensitivity of the beam-splitter, which although specified to polarization independent, had a slight bias towards one polarization.

Performing calibrations removed these artifacts. Figure 8-10 shows the reflectance, transmittance, and absorptance as a function of polarization angle for the same 50%-

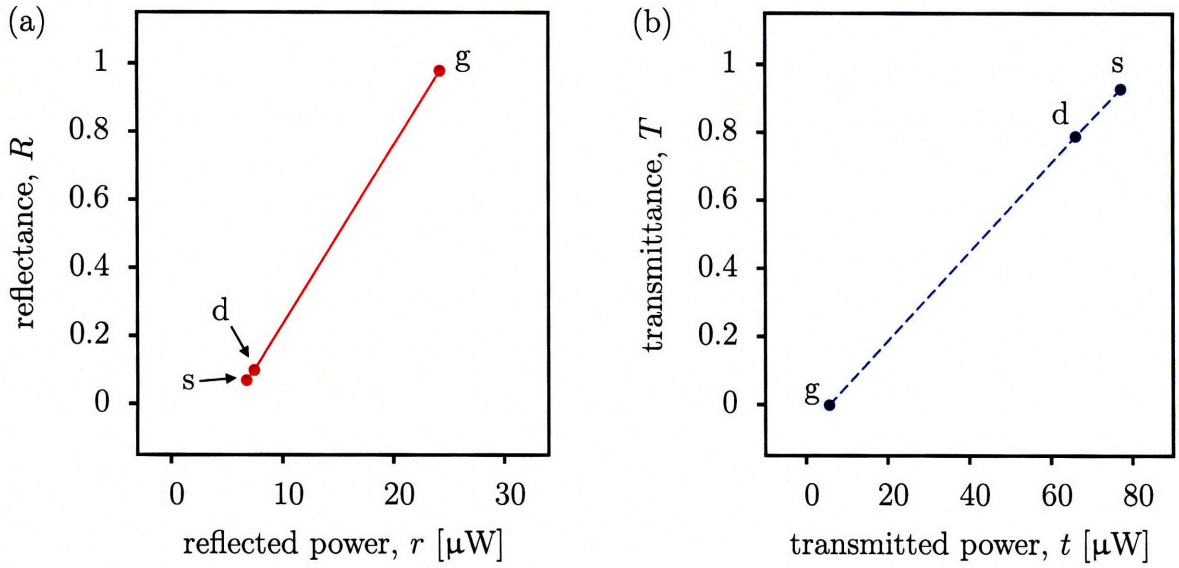

Figure 8-8: Plot of the reflectance R (left), and transmittance T (right) as a function of the reflected (r) and transmitted (t) power. To construct this plot, we assumed that the reflectance and transmittance from an air-sapphire interface has parameters $(R_s, T_s) = (0.07, 0.93)$, while an air-gold interface has parameters $(R_g, T_g) = (0.98, 0)$. The back of the chip had an anti-reflection coating, so did not contribute to additional reflections. We also assumed $R \propto r$, and $T \propto t$ and constructed a straight line between the calibration points. We used this line to find (R_d, T_d) from (r_d, t_d).

fill-factor, 200-nm-pitch device as in Fig. 8-9. In this plot, there is only one minimum and maximum for reflectance, transmittance, and absorptance. The minimum and maximum are located at opposite poles of the Poincaré sphere, as one would expect if they corresponded to parallel and perpendicular polarizations. Figure 8-11 shows the absorptance plotted as a color on a sphere.

We will now present our measurement results.

8.2 Measurement results

We measured the absorptance of five groups of devices with different pitch and fill-factors at room temperature. The groups of devices are pictured in Fig. 7-4. We made measurements on 10 to 13 identical devices in each group to gather some statistics. A plot of the absorptance for each group of devices is shown in Fig. 8-12 along with theoretical absorptances of structures with similar dimensions.

We find that the theoretical data fits the experimental data if we use larger wire widths in our simulation than were nominally measured using the scanning electron microscope. We can justify using different wire widths because increased secondary electron emission from edges makes it difficult to ascertain the true width of the nanowires. Compounding the imaging problem is the fact that we took images of resist and not of the etched structures, because images of etched structures suffer from poor contrast due to substrate charging. The true wire widths can be found using transmission electron microscopy of cross-sectioned devices, but was not performed in this case because of its high cost and destructive nature. Nevertheless, we may be able to find a better fit by tweaking the wire width w, pitch p, and NbN thickness t_{NbN}. We will now explore some of the uncertainties apart from wire width that contribute to the fitting error.

While the fit between experimental and theoretical data was reasonable, it was not ideal for a number of reasons. First, the NbN refractive index we used in our simulations may not be accurate because the refractive index was measured on a thicker film (12 nm) than the film we used to fabricated our devices on (4-6 nm).

Second, we have some uncertainty in the NbN film thickness. We found that a film thickness of 4.35 nm fits the data shown in Fig. 8-12 through a process of trial and error. A small change in the film thickness can result in a significant change in the absorptance. Third, our simple model of infinite gratings may not be sufficient, i.e. a 3D model may be needed. Finally, a better way to perform calibration may be necessary.

We will now discuss the comparison of our absorptance measurements to detection efficiency measurements of the same devices. The detection efficiency measurements were made in collaboration with Dr. Andrew J. Kerman at MIT Lincoln Lab using the setup described in Ref. [55].

8.3 Comparison to detection efficiency measurements

A comparison of detection efficiency to absorptance may possibly answer one important question about our device: is every absorbed photon actually detected? We have measured the detection efficiency of the same devices for which we measured the room-temperature absorptance. We will now compare the results.

In Fig. 8-13, we have plotted the detection efficiency against the room-temperature absorptance for our devices. We have also plotted lines with constant slope P_{R} that represent the ratio between detection efficiency and absorptance. Some features of this plot were as expected; for example, all of the devices had higher absorptance than detection efficiency($P_{\mathrm{R}} < 1$). But there were other features that were unexpected. We will now discuss these features and see how they may yield a new insight into the microscopic physics of SNSPDs.

There are two unexpected features in the data plotted in Fig. 8-13. First, the peak value of P_{R}, the probability of resistive state formation, was only 0.7. In other words, at most 70% of absorbed photons were detected by our devices and the remaining 30% of absorbed photons did not lead to detection events. Second, P_{R} for parallel

polarization ($0.5 < P_{R,||} < 0.7$) is different than P_R for perpendicular polarization ($0.35 < P_{R,\perp} < 0.5$). Figure 8-14 further illustrates the disparity in P_R between the parallel and perpendicular polarizations.

While we do not completely understand the origin of the disparity between $P_{R,||}$ and $P_{R,\perp}$, we have developed a model (jointly with Eric Dauler) that can form a starting point. The main assumption of this model is a position-dependent probability *density* of resistive state formation, i.e. $\psi(x)$, where x is the distance across the nanowire. We do not assume a polarization dependence for $\psi(x)$. The other element of this model is a position-dependent absorption that also depends on the polarization. We can express the absorption through $Q_{av}(x)$, the time-averaged resistive heating [2] given by Eq. 6.8.

These two elements can be combined to give the detection efficiency and absorptance for parallel and perpendicular polarization. The detection efficiency is given by

$$DE = \int_w \psi(x) \frac{Q_{av}(x) t_{NbN}}{i_0} dx, \tag{8.1}$$

where the integral is taken over the wire width w, Q_{av} is the time-averaged resistive heating in units of W/m^2, i_0 is the incident power over one period of the grating, and t_{NbN} is the thickness of the nanowire. The absorptance is given by

$$A = \int_w \frac{Q_{av}(x) t_{NbN}}{i_0} dx. \tag{8.2}$$

We can use these two equations to find a $\psi(x)$ that gives a different P_R for parallel and perpendicular polarizations. We note that $Q_{av}(x)$ has a positional dependence identical to $|E|$ (see Fig. 6-1) and can be easily found through simulations.

Preliminary results show that $\psi(x)$ needs to be larger at the edges of the nanowire than in the center for achieving $P_{R,||} > P_{R,\perp}$. A spatially variant ψ suggests very interesting—and as yet undiscovered—microscopic physics for SNSPDs. Future work will focus on experimentally determining $\psi(x)$ through cryogenic near-field scanning

[2] Our simulations show that it is safe to assume $Q_{av}(x,z) = Q_{av}(x)$ because $|E|$ does not vary much with z across the thickness of the nanowire.

optical microscopy (NSOM) techniques, and researching physical mechanisms for a spatial dependence on $\psi(x)$.

8.4 Conclusion

The goal of the latter half of this thesis was to understand the optical properties of our photodetectors. We developed an optical model for the absorptance and verified that the model makes reasonable predictions. We also found that our measurements suggest interesting microscopic physics involving a spatial dependence for the probability of resistive state formation. We will now summarize our findings by describing the ideal optical design for an SNSPD.

The ideal optical design for SNSPD will achieve high detection efficiencies by ensuring that both the absorptance and probability of resistive state formation (P_{R}) are maximized. The absorptance can be maximized by making devices with high fill-factors. Our data indicates that P_{R} may be higher for narrower wires. A high fill-factor device also has a smaller dependence on the polarization than a low fill-factor device. But if the application calls for a polarization-dependent device, then a low-fill-factor device with narrow wires can be used.

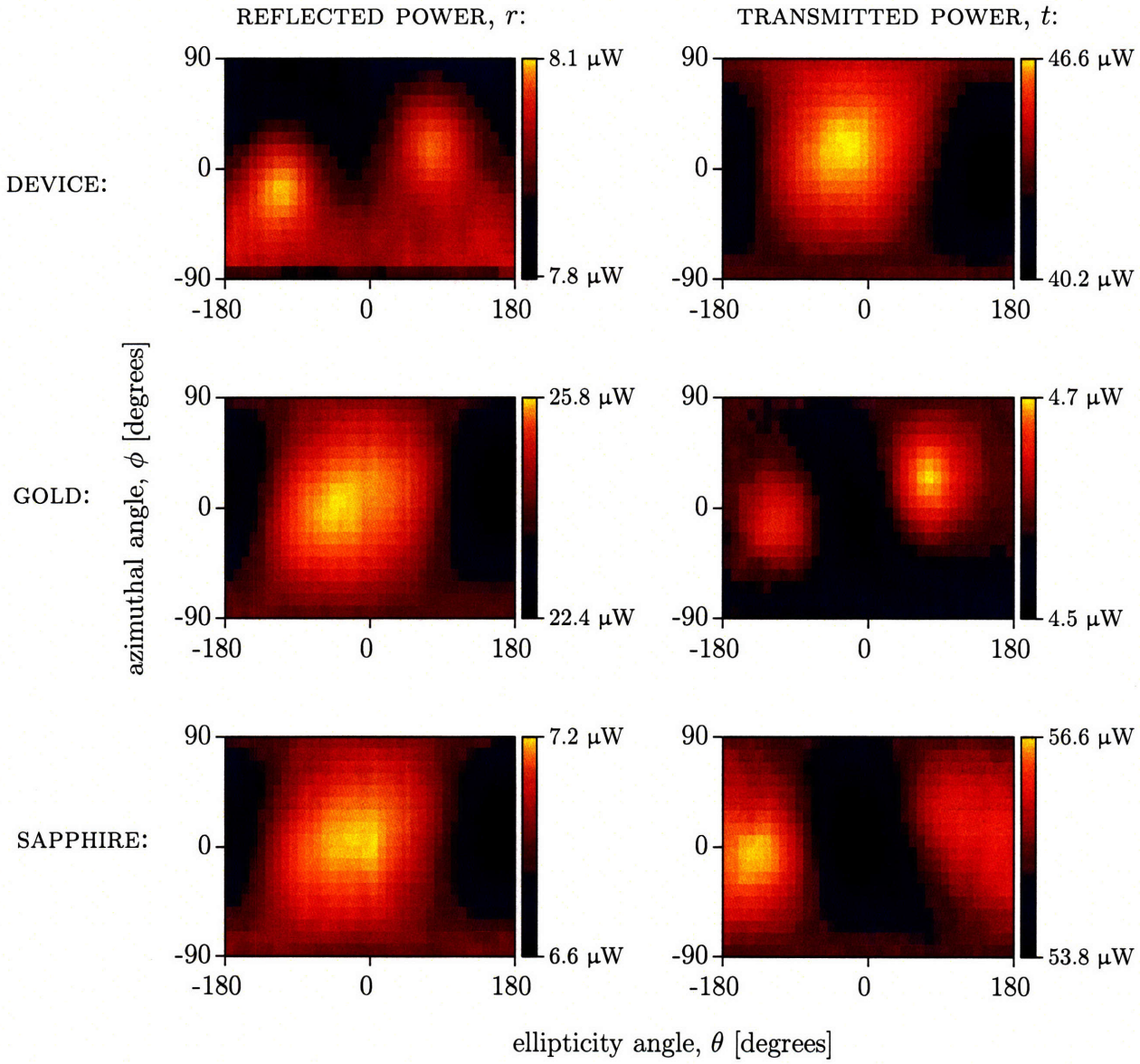

Figure 8-9: Plot of the reflected and transmitted power as a function of the polarization angles θ and ϕ set by the SOP locker for a 200-nm-pitch, 50%-fill-factor device, gold, and sapphire. The beam-splitter introduced a small polarization sensitivity that was manifested for gold and sapphire, which we would otherwise expect to have no polarization sensitivity. Later, we calibrated the reflected power to remove the artifacts introduced by the beam splitter.

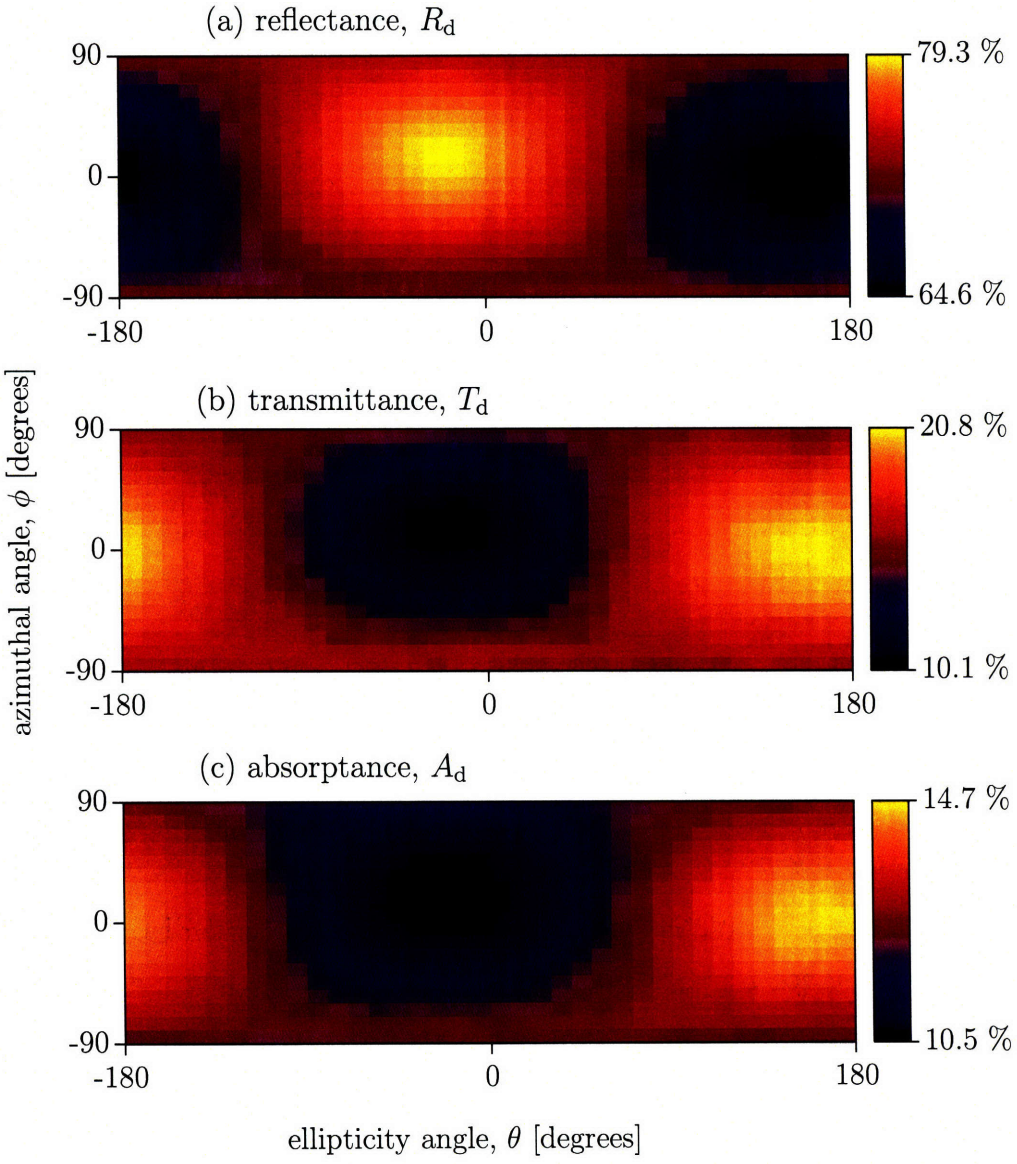

Figure 8-10: Plot of the reflectance, transmittance, and absorptance as a function of the polarization angles θ and ϕ set by the SOP locker for a 200-nm-pitch, 50%-fill-factor device. These plots were generated after calibration was performed on the raw data data shown in Fig. 8-9.

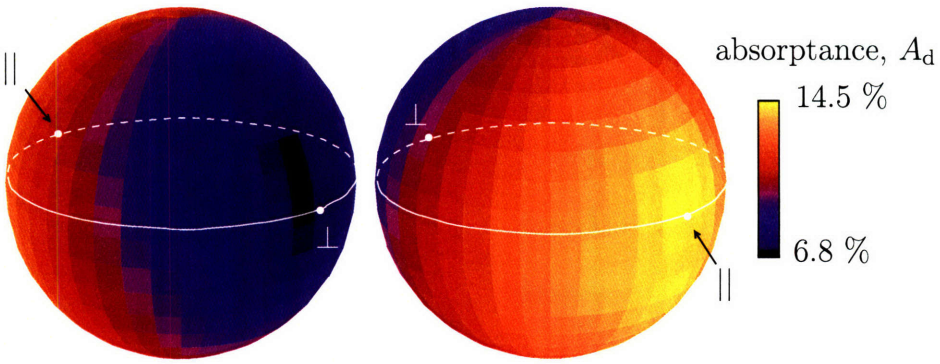

Figure 8-11: Plot of the measured, room-temperature absorptance as a function of polarization for a 25% fill-factor, 400-nm-pitch SNSPD. Locations on the spheres represent polarizations on the Poincaré sphere (e.g. || and ⊥), while the coloring represents the absorptance. Both spheres are plotted with the identical data.

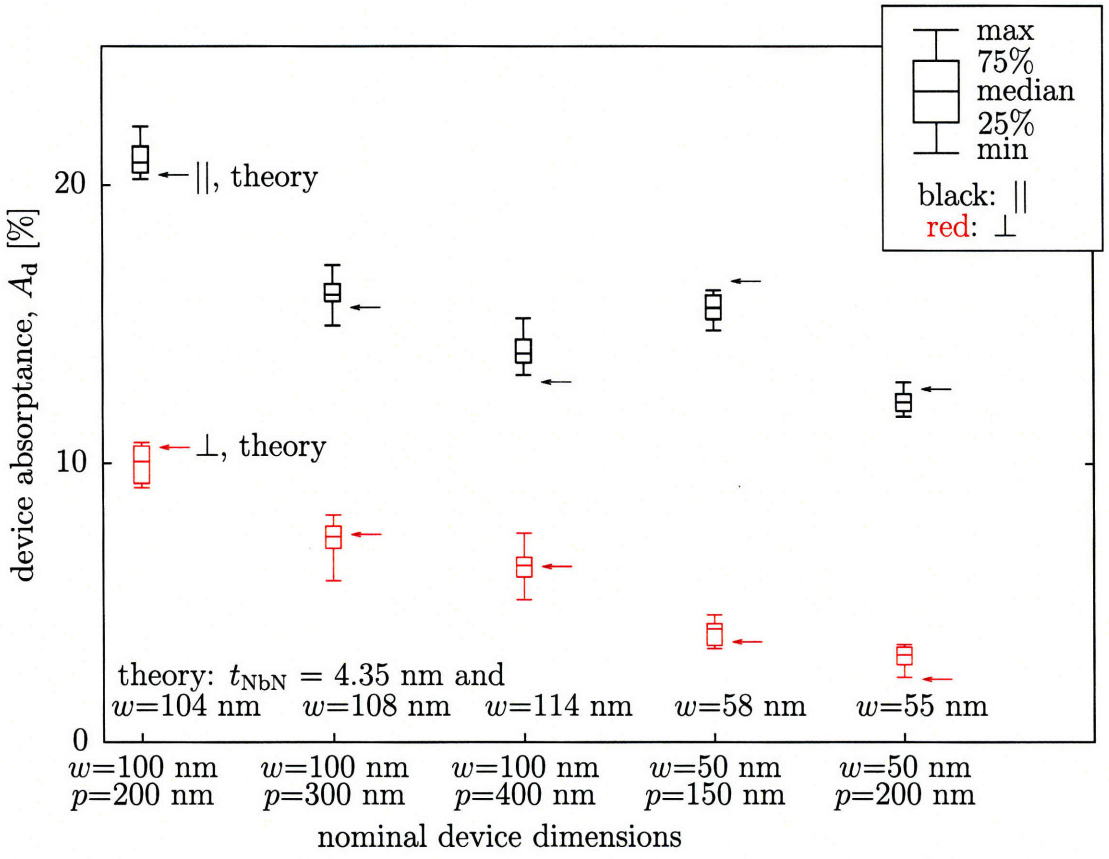

Figure 8-12: Statistical plot of the measured parallel (||) and perpendicular (⊥) absorptance for various device types. Each data symbol represents measurements of at least 10 devices for the polarization that yielded the maximum (||) or minimum (⊥) absorptance. The red and black arrows indicate the theoretical result for structures with wire width w as shown, NbN thickness t_{NbN}=4.35 nm, and nominal values of pitch p.

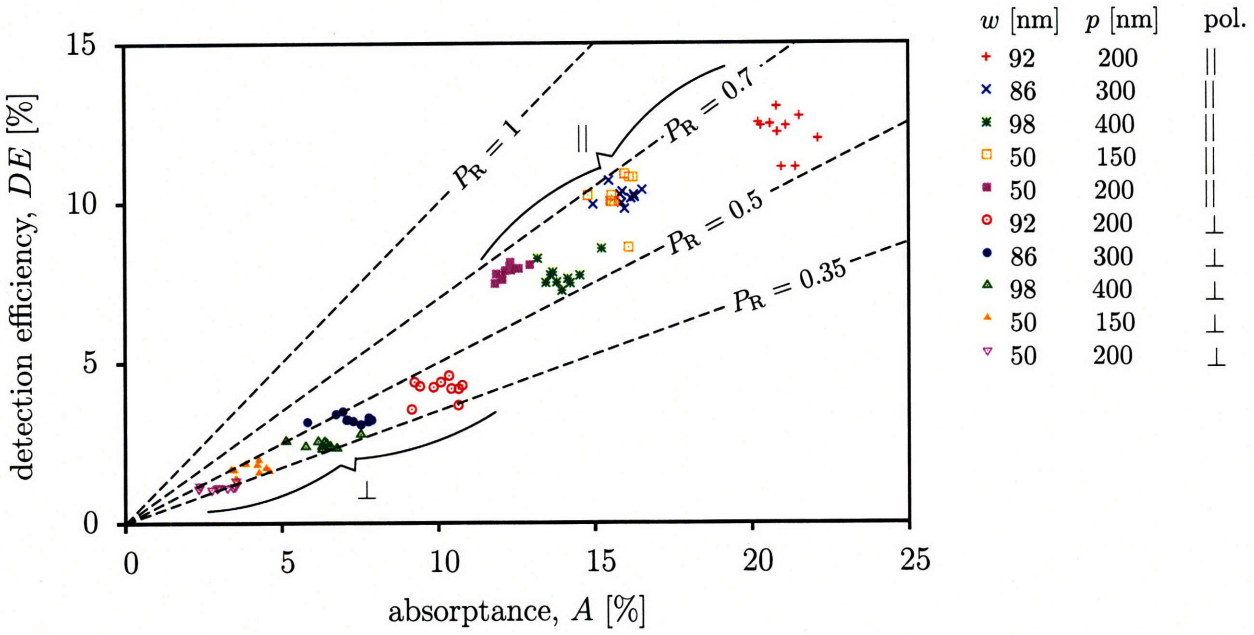

Figure 8-13: Plot of detection efficiency as a function of absorptance for the same devices. Dotted lines have a constant slope given by P_R, the probability of resistive state formation.

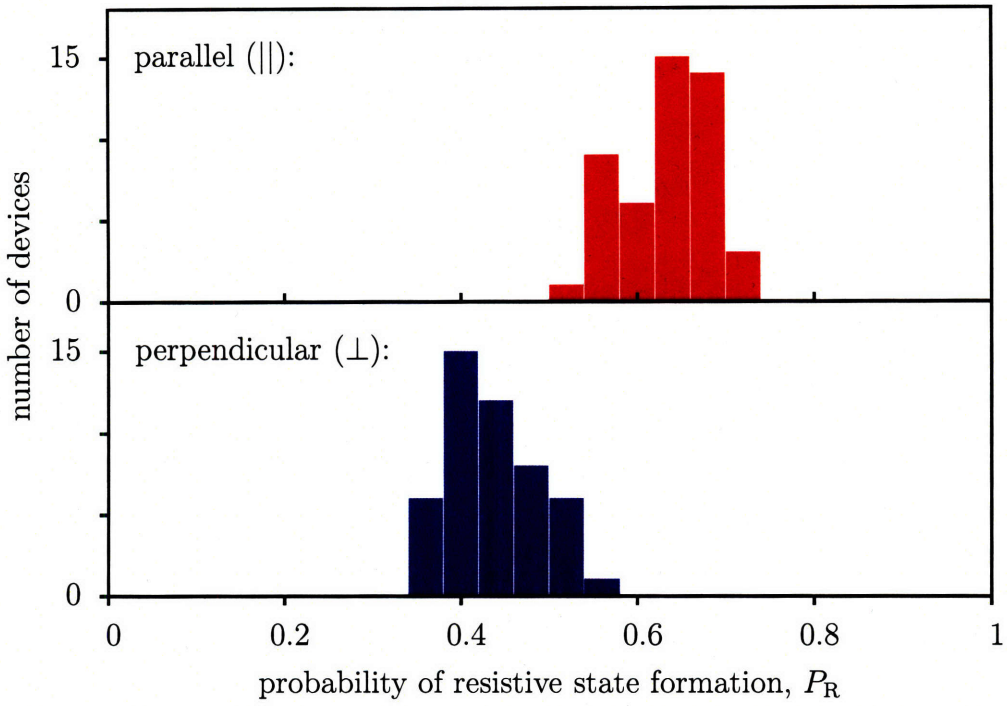

Figure 8-14: Histogram of the probability of resistive state formation (ratio of detection efficiency to room-temperature absorption), P_R for parallel (||) and perpendicular (⊥) polarizations. The histogram clearly that P_R has a different mean for different polarizations.

Chapter 9

Conclusion

In this thesis, many contributions were made to the fields of optics and nanotechnology.

In the first half of the thesis, we explored refractive-index engineering techniques that can impact many applications, ranging from optical lithography to slow light. One of our major results showed that a two-level system with population inversion is not practical for an immersion lithography application. We then proposed a general scheme for refractive-index engineering that uses a mixture of amplifying and absorbing resonances to circumvent the problems we faced with the two-level system. Our proposal unified a number of other refractive index engineering techniques into the same framework.

Future work in this area will involve a search for materials with appropriately spaced resonances that form the building blocks of our proposal. A major challenge of this search will be understanding how to combine the resonances in a homogeneous mixture. Once suitable materials are found, further work will be necessary to apply these materials first to a proof-of-principle experiment, and later to applications.

In the second half of this thesis, we investigated the optical properties of superconducting nanowire single-photon detectors. Our major contributions include an optical model that can predict the absorptance of our devices; an apparatus that achieved the first direct measurement of absorptance of these devices; experimental verification of the polarization sensitivity of our detectors; a direct comparison of

detection efficiency to absorptance; and data that points to a positional dependence of the probability density of resistive state formation, ψ.

There are many interesting questions that spring from the work in this thesis. Future work can focus on what the detection efficiency to absorptance ratio, P_{R} depends on and whether it is capped at 0.7. Another interesting direction is to explore the theoretical basis behind the spatial dependence of ψ. Finally, we can also pursue experimental verification of the spatial dependence of ψ through novel cryogenic imaging techniques.

Appendix A

Pump beam absorption

We will now address the issue of pump beam absorption in atomic media. We will solve a differential equation that phenomenologically describes the effective propagation distance of a strong pump beam in an absorptive atomic medium. We will then graphically illustrate the solution by using parameters from the 4^1S to 4^1P transition in atomic calcium.

A.1 Introduction

In Chapter 3, we focused on the enhancement of refractive index for a coherent probe laser in a pumped two level system. In the pumped two-level system, shown in Figure 3-2, the probe laser is appropriately detuned from $|c\rangle$-$|b\rangle$ transition in the presence of incoherent pump radiation on the $|b\rangle$-$|a\rangle$ transition. When we imposed population inversion between $|b\rangle$ and $|c\rangle$, the refractive index at the probe frequency was greatly enhanced. Moreover, the probe radiation experienced optical gain, thereby averting high absoption that would normally accompany a high index of refraction in an unpumped two-level system.

Our calculations in this appendix, however, are not restricted to this system. It will be required by any system (including the ones we have presented in Chapter 4) that has a pumped quantum system as its constituent for applications such as lithography where we require a patterned probe beam that occupies an appreciable

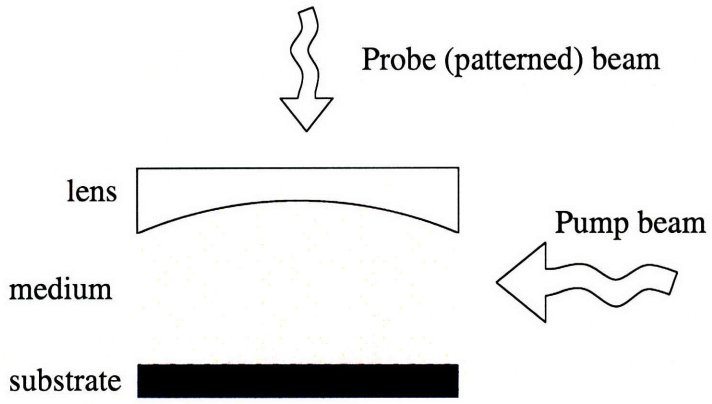

Figure A-1: Schematic of one possible configuration for a lithographic system utilizing our index enhancement schemes.

lateral distance (> 100 μm). One configuration for a lithographic application is shown in Figure A-1, where the pump beam enters the medium laterally, while the probe patterned beam is normal to the substrate. It is clear that the pump radiation must maintain population inversion over the entire region that the probe laser propagates in order to inhibit probe absorption. However, regardless of whether the probe beam experiences amplification (if the scheme from Chapter 3 is used) or transparency (if the scheme from Chapter 4 is used), the pump beam will be absorbed by the medium. In both Chapter 3 and 4, we have assumed the presence of a pump radiation with sufficient intensity. In this Appendix, we will see just how intense the pump radiation must be to maintain inversion.

A.2 Formulating an equation for macroscopic absorption

A two-level system can be used to model absorption for the pump beam in our system. We follow the derivation presented by Loudon [39] for macroscopic absorption of an optical beam in a two level system and then use the 4^1S to 4^1P transition in atomic calcium to illustrate our results.

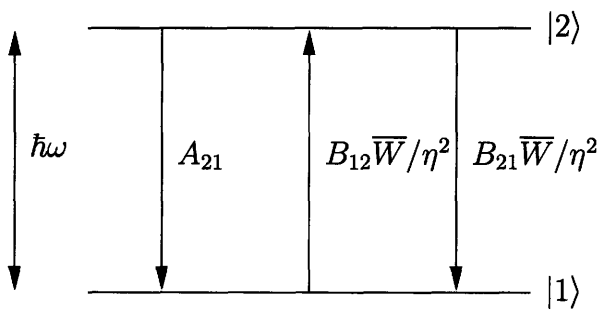

Figure A-2: Transitions for a two level system with refractive index η. Modified version of Figure 1.8 from [39].

A.2.1 Rate equation

We begin by phenomenologically constructing a differential equation relating beam intensity with propagation distance. We consider a two-level quantum system with refractive index η as shown in Figure A-2, where the rates of spontaneous emission, absorption and stimulated emission are proportional to A_{21}, $B_{12}\overline{W}/\eta^2$, $B_{21}\overline{W}/\eta^2$ respectively. $\overline{W}$ is the energy density of radiation (i.e. energy from a photon impinging upon the system), which is required for absorption and stimulated emission in order to conserve energy. From here on, we assume $B_{12} = B_{21} = B$ and $A_{21} = A$.

The rate equation for this system is given by

$$\frac{\mathrm{d}N_1}{\mathrm{d}t} = -\frac{\mathrm{d}N_2}{\mathrm{d}t} = N_2 A + (N_2 - N_1)B\frac{\overline{W}}{\eta^2}, \tag{A.1}$$

which is solved at steady state to give

$$N_2 A = (N_1 - N_2)B\frac{\overline{W}}{\eta^2}, \tag{A.2}$$

where N_i is the population in level $|i\rangle$. Equation (A.2) can be seen as an energy balance equation if we multiply both sides with $\hbar\omega$, where ω is the frequency of an emitted (via stimulation) or absorbed photon. In that case, the left hand side relates the rate that energy is scattered out of the system, $N_2 A\,\hbar\omega$, to the rate of energy loss in the beam that is proportional to the energy density $\overline{W}$. There is a lineshape associated with the frequencies at which stimulated and absorption transitions between $|1\rangle$ and $|2\rangle$ can occur, given by a normalized function $F(\omega)$, usually Lorentzian in shape. By

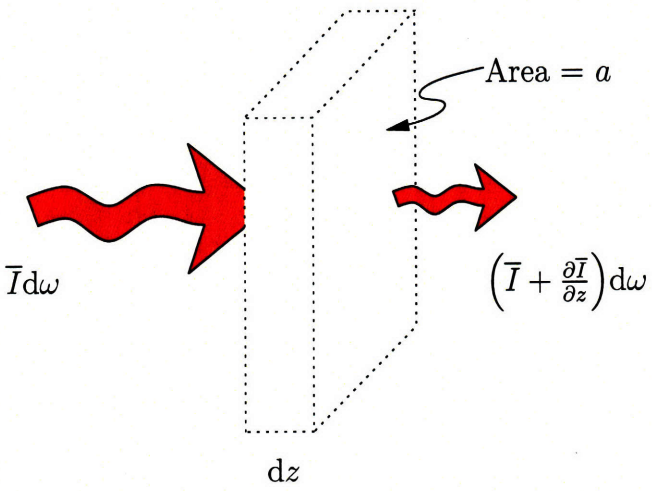

Figure A-3: Beam attenuation after propagation in a slice of the atomic medium. Reproduced from Ref. [39].

multiplying by $F(\omega)\mathrm{d}\omega$, we get the fraction of energy that is absorbed for a small frequency interval $\mathrm{d}\omega$. Therefore, the rate of change of beam energy in an frequency interval of $\mathrm{d}\omega$ is given by

$$-(N_1 - N_2)F(\omega)\mathrm{d}\omega B\overline{W}\hbar\omega/\eta^2. \tag{A.3}$$

A.2.2 Energy loss expressed in term of intensity

Now we consider a beam propagating in the z direction, as shown in Figure A-3, interacting with a thin slice of the atomic medium with volume $a\,\mathrm{d}z$. The beam energy contained within this slice for a frequency interval $\mathrm{d}\omega$ is $\overline{W}\mathrm{d}\omega\,a\,\mathrm{d}z$, while the fraction of the total atoms in our system that are contained within this slice is given by $a\,\mathrm{d}z/V$, where V is the volume of our medium. Therefore, we can write an equation that relates the change of energy in the slice as a function of time

$$\frac{\partial(\overline{W}\mathrm{d}\omega\,a\,\mathrm{d}z)}{\partial t} = -(N_1 - N_2)F(\omega)\mathrm{d}\omega B\overline{W}\frac{\hbar\omega}{\eta^2}\left(\frac{a\,\mathrm{d}z}{V}\right) \tag{A.4}$$

which simplifies to

$$\tag{A.5}$$

$$\frac{\partial \overline{W}}{\partial t} = -\frac{N_1 - N_2}{V} F(\omega) B \overline{W} \frac{\hbar\omega}{\eta^2}. \tag{A.6}$$

Now, we note that the energy density $\overline{W}$ is related to the intensity $\overline{I}$ via

$$\frac{\partial \overline{W}}{\partial t} = \frac{\partial \overline{I}}{\partial z} \tag{A.7}$$

and

$$c\overline{W} = \eta \overline{I} \tag{A.8}$$

so we can recast equation (A.6) as

$$\frac{\partial \overline{I}}{\partial z} = -\frac{N_1 - N_2}{V} F(\omega) B \frac{\hbar\omega}{c\eta} \overline{I}. \tag{A.9}$$

A.3 Analytical solution for intensity decay

By solving the optical Bloch equations under steady state conditions for a two level system, we can substitute for $N_1 - N_2$ in terms of N_t (the total number of atoms) and other parameters into A.9to obtain

$$\frac{1}{\overline{I}}\left(1 + \frac{2B\overline{I}}{Ac\eta}\right)\frac{\partial \overline{I}}{\partial z} = -\frac{N_t B \hbar\omega F(\omega)}{Vc\eta}. \tag{A.10}$$

This differential equation is easily solved to yield

$$\ln\left(\frac{\overline{I}}{\overline{I}_0}\right) + \frac{2\pi^2 c^2}{\hbar\omega^3 \eta}(\overline{I} - \overline{I}_0) = -\frac{N\pi^2 c^2 A F(\omega)}{\omega^2 \eta} z, \tag{A.11}$$

Table A.1: General parameters for Figures A-5 to A-7

Parameter	Value	Units
Frequency of 4^1S to 4^1P transition [37], ω	4.5×10^{15}	rad/s
Einstein A coefficient for transition	2.2×10^8	s^{-1}
Frequency spread of pump laser, $d\omega$	$2\pi \times 10^{10}$	rad/s
Value of lineshape function, $F(\omega)$ over $d\omega$	1	
Saturation intensity, $\overline{I}_{sat}$	2.27×10^5	W/m^2
Index of refraction, η	3	

where $\overline{I}_0 = \overline{I}|_{z=0}$, $N = N_t/V$, and we have substituted

$$B = \frac{\pi^2 c^3}{\hbar \omega^3} A$$

.

A.4 Results for a transition in atomic calcium

We now proceed to calculate the penetration depth of a pump laser in an atomic vapor composed of calcium (without taking temperature effects into account). The relevant parameters are given in Table A.1. The frequency spread of the pump laser, the value of the lineshape function, and index of refraction have been assumed, while the saturation intensity, $\overline{I}_{sat}$ is a derived quantity obtained from Figure A-4, and is discussed in the following section.

A.4.1 Calculating saturation intensity, $\overline{I}_{sat}$

Figure A-4 shows a plot of the fraction of excited state population as a function of intensity obtained via solving the two-state optical Bloch equations in steady state. The point at which the normalized intensity is unity is where we define $\overline{I}_{sat}$, which is also where one-third of the population is in the excited state.

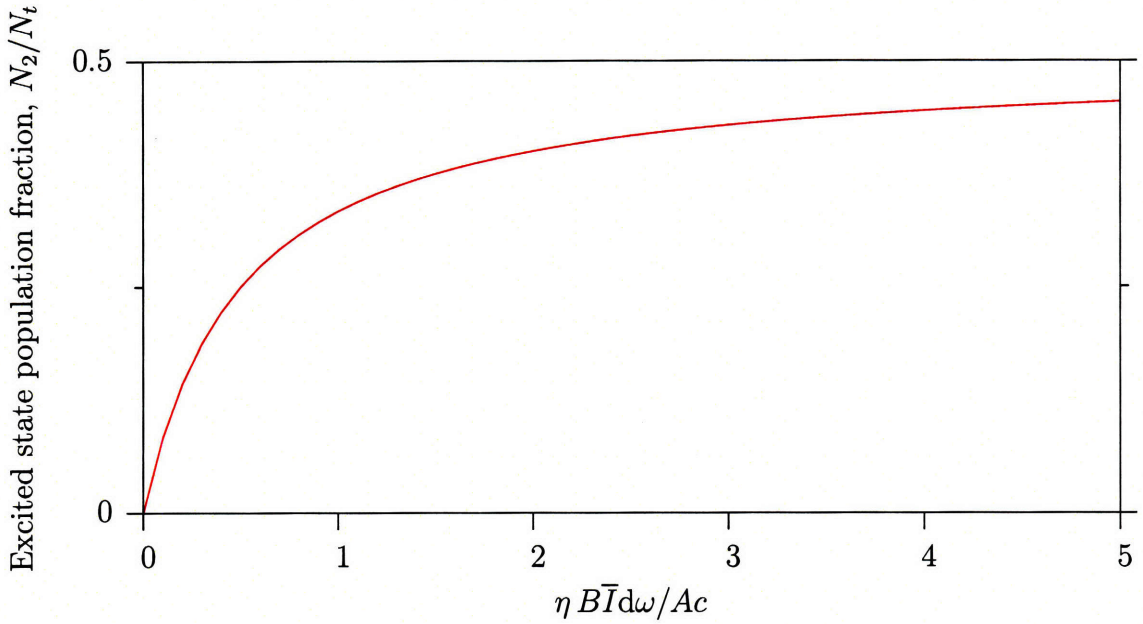

Figure A-4: Fraction of excited state population versus normalized intensity. The point where $\eta B\overline{I}\mathrm{d}\omega/Ac = 1$ is where we define $\overline{I}_{\mathrm{sat}} = \overline{I}\mathrm{d}\omega$, the saturation intensity. Modified version of Figure 1.11 from [39].

A.4.2 Intensity decay within the medium

Figure A-5 shows the decay of intensity for a pump beam with initial intensity $\overline{I}_0\,\mathrm{d}\omega = 10^{10}\,\mathrm{W/m^2}$ as the beam propagates in an atomic medium with parameters given in Table A.1. After some propagation where the intensity decays linearly, a sharp decay is seen, which is where the logarithmic term in Equation A.11 dominates. The intersection between the traces and the saturation intensity, $\overline{I}_{\mathrm{sat}}$ is the point we define as z_{max}, the distance in the medium where the fraction of excited state population is above one-third. z_{max} is plotted versus atomic density, N for various initial intensities $\overline{I}_0\mathrm{d}\omega$ in Figures A-6 and A-7.

A.5 Conclusion

We have determined, through the solution of a phenomenological differential equation describing macroscopic absorption, the effective propagation distance of a pump beam in an absorptive atomic medium. The resulting plots can be very useful in determining the operating point for our system. For example, from Figure A-6 we can see that for

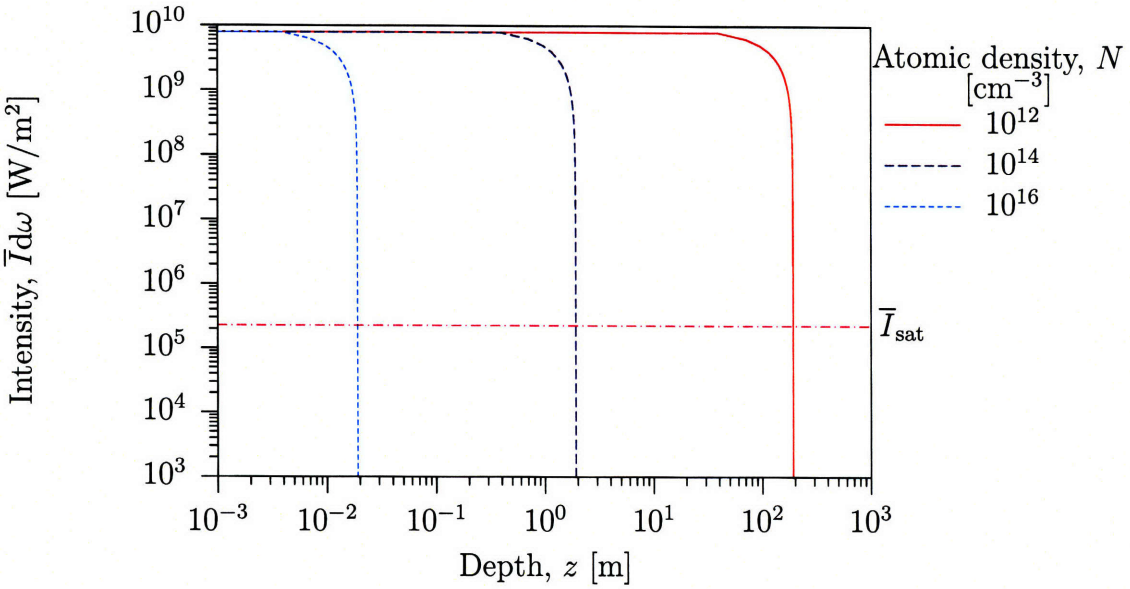

Figure A-5: Variation of intensity of a beam with spectral width $\mathrm{d}\omega = 2\pi \times 10^{10}$ as it propagates in an atomic medium. Marked on the plot is $\overline{I}_{\mathrm{sat}}$, the intensity $\overline{I}\mathrm{d}\omega$ where $\eta B\overline{I}\mathrm{d}\omega/Ac = 1$ (see Figure A-4).

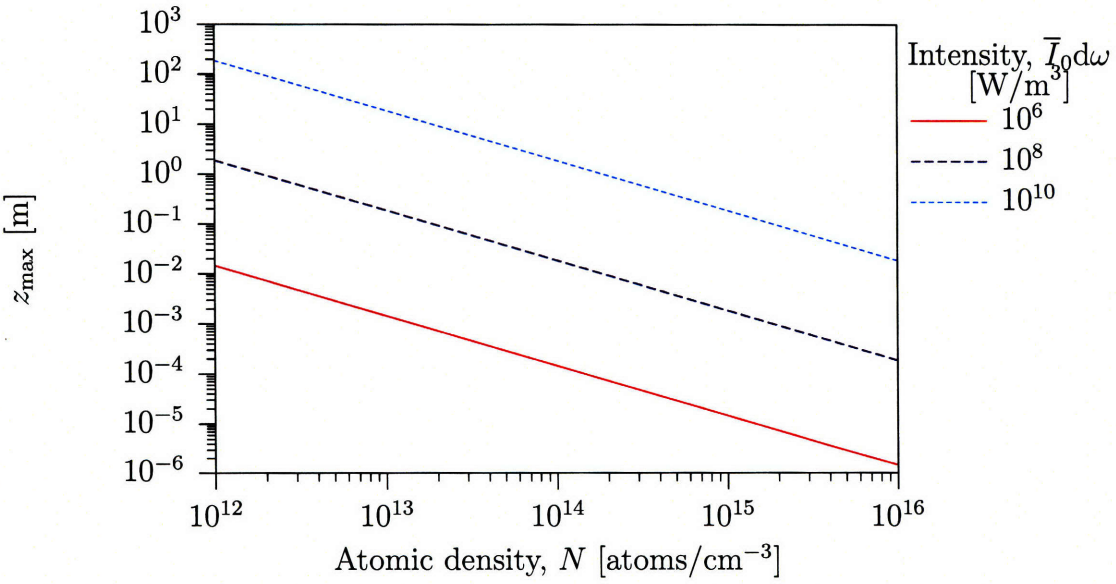

Figure A-6: Maximum depth z_{max} achieved by a beam with various initial intensities $\overline{I}_0\mathrm{d}\omega$ in a medium of atomic density N. z_{max} is defined as the point where $\overline{I}\mathrm{d}\omega = \overline{I}_{\mathrm{sat}}$.

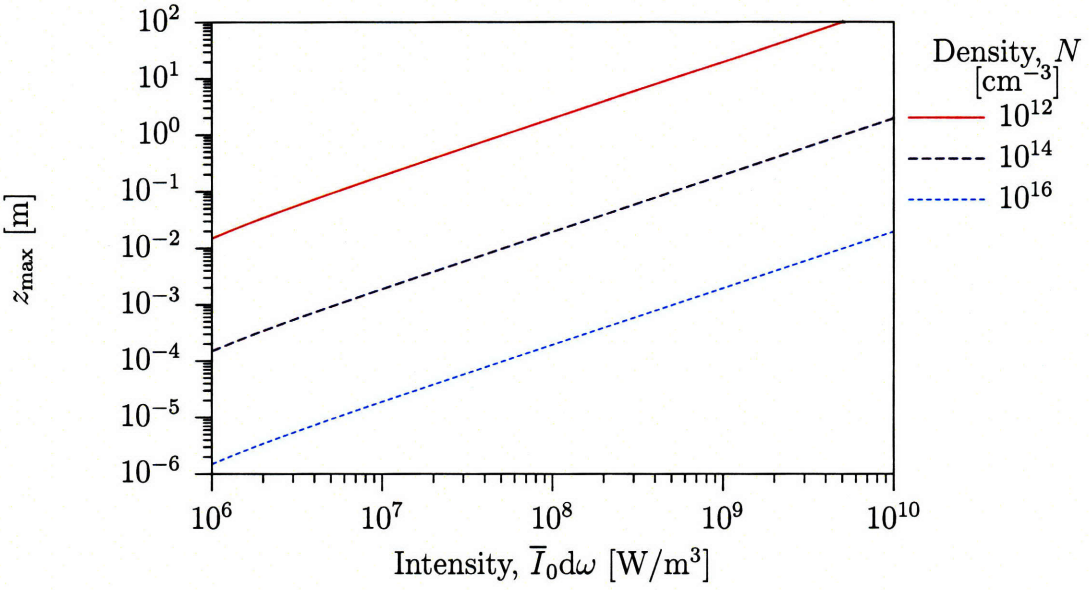

Figure A-7: Maximum depth z_{max} achieved by a beam with initial intensity $\overline{I}_0 d\omega$ for various atomic densities. z_{max} is defined as the point where $\overline{I} d\omega = \overline{I}_{sat}$.

a 1-cm-thick vapor cell with atomic density $N = 3 \times 10^{14}$, we can maintain an excited state population of greater than 1/3 of the total population with an initial intensity, $\overline{I}_0 d\omega = 10^8$ W/m^2. Initial intensity this high can be achieved with a focused laser beam.

List of acronyms

ASE	amplified spontaneous emission
EDFA	erbium-doped fiber amplifier
EIT	electromagnetically induced transparency
FDTD	finite-difference time-domain
FEM	finite element method
QKD	quantum key distribution
SBS	stimulated Brillouin scattering
SNSPD	superconducting nanowire single-photon detector
WGP	wire grid polarizer

Bibliography

[1] D. Gil, T. A. Brunner, C. Fonseca, N. Seong, B. Streefkerk, C. Wagner, and M. Stavenga. Immersion lithography: New opportunities for semiconductor manufacturing. *J. Vac. Sci. Technol. B*, 22(6):3431, 2004.

[2] International technology roadmap for semiconductors, 2006 Update for Lithography, http://www.itrs.net/Links/2006Update/2006UpdateFinal.htm.

[3] M. Rothschild, T. M. Bloomstein, R. R. Kunz, V. Liberman, M. Switkes, S. T. Palmacci, J. H. C. Sedlacek, D. Hardy, and A. Grenville. Liquid immersion lithography: Why, how, and when? *J. Vac. Sci. Technol. B*, 22(6):2877, 2004.

[4] D. F. Phillips, A Fleischhauer, A Mair, R. L. Walsworth, and M. D. Lukin. Storage of light in atomic vapor. *Phys. Rev. Lett.*, 86(5):783, 2001.

[5] Z Wang and S Fan. Compact all-pass filters in photonic crystals as the building block for high-capacity optical delay lines. *Phys. Rev. E*, 68(6):66616, 2003.

[6] M. F. Yanik, S. Fan, M. Soljacic, and J. D. Joannopoulos. All-optical transistor action with bistable switching in a photonic crystal cross-waveguide geometry. *Opt. Lett.*, 28(24):2506, 2003.

[7] M. D. Lukin, S. F. Yelin, M. Fleischhauer, and M. O. Scully. Quantum interference effects induced by interacting dark resonances. *Phys. Rev. A*, 60(4):3225, 1999.

[8] M. Soljacic and J. D. Joannopoulos. Enhancement of nonlinear effects using photonic crystals. *Nat. Mater.*, 3(4):211, 2004.

[9] Q. F. Xu, S. Sandhu, M. L. Povinelli, J. Shakya, S. Fan, and M. Lipson. Experimental realization of an on-chip all-optical analogue to electromagnetically induced transparency. *Phys. Rev. Lett.*, 96(12):123901, 2006.

[10] M. S. Bigelow, N. N. Lepeshkin, and R. W. Boyd. Superluminal and slow light propagation in a room-temperature solid. *Science*, 301(5630):200, 2003.

[11] R. M. Camacho, M. V. Pack, and J. C. Howell. Low-distortion slow light using two absorption resonances. *Phys. Rev. A*, 73(6):063812, 2006.

[12] C. Liu, Z. Dutton, C. H. Behroozi, and L. V. Hau. Observation of coherent optical information storage in an atomic medium using halted light pulses. *Nature (London)*, 409(6819):490, 2001.

[13] J. J. Longdell, E. Fraval, M. J. Sellars, and N. B. Manson. Stopped light with storage times greater than one second using electromagnetically induced transparency in a solid. *Phys. Rev. Lett.*, 95(6):063601, 2005.

[14] A. V. Turukhin, V. S. Sudarshanam, M. S. Shahriar, J. A. Musser, B. S. Ham, and P. R. Hemmer. Observation of ultraslow and stored light pulses in a solid. *Phys. Rev. Lett.*, 88(2):023602, 2001.

[15] J. B. Pendry. Negative refraction makes a perfect lens. *Phys. Rev. Lett.*, 85(18):3966, 2000.

[16] C. Luo, S. G. Johnson, J. D. Joannopoulos, and J. B. Pendry. All-angle negative refraction without negative effective index. *Phys. Rev. B*, 65(20):201104, 2002.

[17] V. G. Veselago. The electrodynamics of substances with simultaneously negative values of ϵ and μ. *Sov. Phys. Usp.*, 10(4):509, 1968.

[18] R. A. Shelby, D. R. Smith, and S. Schultz. Experimental verification of a negative index of refraction. *Science*, 292(5514):77, 2001.

[19] A. A. Houck, J. B. Brock, and I. L. Chuang. Experimental observations of a left-handed material that obeys snell's law. *Phys. Rev. Lett.*, 90(13), 2003.

[20] T. Driscoll, D. N. Basov, A. F. Starr, P. M. Rye, S. Nemat-Nasser, D. Schurig, and D. R. Smith. Free-space microwave focusing by a negative-index gradient lens. *Appl. Phys. Lett.*, 88(8), 2006.

[21] V. M. Shalaev, W. Cai, U. K. Chettiar, H.-K. Yuan, A. K. Sarychev, V. P. Drachev, and A. V. Kildishev. Negative index of refraction in optical metamaterials. *Opt. Lett.*, 30(24):3356, 2005.

[22] N. Fang, H. Lee, C. Sun, and X. Zhang. Sub-diffraction-limited optical imaging with a silver superlens. *Science*, 308(5721):534, 2005.

[23] D. O. S. Melville and R. J. Blaikie. Super-resolution imaging through a planar silver layer. *Opt. Express*, 13(6):2127, 2005.

[24] K. J. Boller, A. Imamoglu, and S. E. Harris. Observation of electromagnetically induced transparency. *Phys. Rev. Lett.*, 66(20):2593, 1991.

[25] A. S. Zibrov, M. D. Lukin, L. Hollberg, D. E. Nikonov, M. O. Scully, H. G. Robinson, and V. L. Velichansky. Experimental demonstration of enhanced index of refraction via quantum coherence in rb. *Phys. Rev. Lett.*, 76(21):3935, 1996.

[26] M. O. Scully. Enhancement of the index of refraction via quantum coherence. *Phys. Rev. Lett.*, 67(14):1855, 1991.

[27] M. O. Scully and S. Y. Zhu. Ultra-large index of refraction via quantum interference. *Opt. Commun.*, 87(3):134, 1992.

[28] M. Fleischhauer, C. H. Keitel, M. O. Scully, C. Su, B. T. Ulrich, and S. Y. Zhu. Resonantly enhanced refractive-index without absorption via atomic coherence. *Phys. Rev. A*, 46(3):1468, 1992.

[29] C. Szymanowski and C. H. Keitel. Enhancing the index of refraction under convenient conditions. *J. Phys. B*, 27(23):5795, 1994.

[30] H. Y. Ling and S. Barbay. Large index of refraction with vanishing absorption in the 2-level atomic system driven by a strong-field. *Opt. Commun.*, 111(3-4):350, 1994.

[31] M. Fleischhauer, A. Imamoglu, and J. P. Marangos. Electromagnetically induced transparency: Optics in coherent media. *Rev. Mod. Phys.*, 77(2):633, 2005.

[32] Marlan O. Scully and Muhammad Suhail Zubairy. *Quantum optics.* Cambridge University Press, Cambridge ; New York, 1997.

[33] John David Jackson. *Classical electrodynamics.* Wiley, New York, 3rd edition, 1999.

[34] Vikas Anant, Magnus Rådmark, Ayman F. Abouraddy, Thomas C. Killian, and Karl K. Berggren. Pumped atomic systems: immersion fluids of the future? *J. Vac. Sci. Technol. B*, 23:2662, 2005.

[35] S. M. Mansfield and G. S. Kino. Solid immersion microscope. *Appl. Phys. Lett.*, 57(24):2615, 1990.

[36] S. E. Harris, J. E. Field, and A. Kasapi. Dispersive properties of electromagnetically induced transparency. *Phys. Rev. A*, 46(R29), 1992.

[37] R. C. Hilborn. Einstein coefficients, cross-sections, f values, dipole-moments, and all that. *Am. J. Phys.*, 50(11):982, 1982.

[38] J. J. Sakurai and San Fu Tuan. *Modern quantum mechanics.* Addison-Wesley Pub. Co., Reading, Mass., rev. edition, 1994.

[39] Rodney Loudon. *The quantum theory of light.* Oxford science publications. Oxford University Press, Oxford ; New York, 3rd edition, 2000.

[40] Anders Bjarklev. *Optical fiber amplifiers : design and system applications.* Artech House, Boston, 1993.

[41] P. Weßels, M. Auerbach, and C. Fallnich. Narrow-linewidth master oscillator fiber power amplifier system with very low amplified spontaneous emission. *Opt. Commun.*, 205(1-3):215, 2002.

[42] L. V. Hau, S. E. Harris, Z. Dutton, and C. H. Behroozi. Light speed reduction to 17 metres per second in an ultracold atomic gas. *Nature (London)*, 397(6720):594, 1999.

[43] K. Y. Song, M. G. Herraez, and L. Thevenaz. Observation of pulse delaying and advancement in optical fibers using stimulated brillouin scattering. *Opt. Express*, 13(1):82, 2005.

[44] Y. Okawachi, M. S. Bigelow, J. E. Sharping, Z. M. Zhu, A. Schweinsberg, D. J. Gauthier, R. W. Boyd, and A. L. Gaeta. Tunable all-optical delays via brillouin slow light in an optical fiber. *Phys. Rev. Lett.*, 94(15):153902, 2005.

[45] L. J. Wang, A. Kuzmich, and A. Dogariu. Gain-assisted superluminal light propagation. *Nature (London)*, 406(6793):277, 2000.

[46] Y. F. Chen, P. Fischer, and F. W. Wise. Negative refraction at optical frequencies in nonmagnetic two-component molecular media. *Phys. Rev. Lett.*, 95(6):067402, 2005.

[47] S. A. Ramakrishna and J. B. Pendry. Removal of absorption and increase in resolution in a near-field lens via optical gain. *Phys. Rev. B*, 67(20):201101(R), 2003.

[48] Tuck C. Choy. *Effective medium theory : principles and applications.* Oxford University Press, New York, 1999.

[49] F. J. Ribeiro and M. L. Cohen. Amplifying sommerfeld precursors and producing a discontinuous index of refraction with gains and losses. *Phys. Rev. E*, 64(4):046602, 2001.

[50] Robert W. Boyd. *Nonlinear optics.* Academic Press, Boston, 1992.

[51] D Pohl and W. Kaiser. Time-resolved investigations of stimulated brillouin scattering in transparent and absorbing media: Determination of phonon lifetimes. *Phys. Rev. B*, 1(1):31, 1970.

[52] http://www.comsol.com.

[53] Pochi Yeh. *Optical waves in layered media.* Wiley series in pure and applied optics. Wiley, New York, 1988.

[54] J. K. W. Yang, E. Dauler, A. Ferri, A. Pearlman, A. Verevkin, G. Gol'tsman, B. Voronov, R. Sobolewski, W. E. Keicher, and K. K. Berggren. Fabrication development for nanowire GHz-counting-rate single-photon detectors. *IEEE Trans. Appl. Supercond.*, 15(2):626, 2005.

[55] A. J. Kerman, E. Dauler, W. E. Keicher, J. K. W. Yang, K. K. Berggren, G. Gol'tsman, and B. Voronov. Kinetic-inductance-limited reset time of superconducting nanowire photon counters. *Appl. Phys. Lett.*, 88:111116, 2006.

[56] Eric A. Dauler, Bryan S. Robinson, Andrew J. Kerman, Vikas Anant, Richard J. Barron, Karl K. Berggren, David O. Caplan, John J. Carney, Scott A. Hamilton, Kristine M. Rosfjord, Mark L. Stevens, and Joel K. Yang. 1.25 Gbit/s photon-counting optical communications using a two-element superconducting nanowire single photon detector. In Wolfgang Becker, editor, *Proc. SPIE*, volume 6372 of *Advanced Photon Counting Techniques*, page 637212, Oct 2006.

[57] K. M. Rosfjord, J. K. W. Yang, E. A. Dauler, A. J. Kerman, V. Anant, B. M. Voronov, G. N. Gol'tsman, and K. K. Berggren. Nanowire single-photon detector with an integrated optical cavity and anti-reflection coating. *Opt. Express*, 14(2):527, 2006.

[58] M. J. Fitch, B. C. Jacobs, T. B. Pittman, and J. D. Franson. Photon-number resolution using time-multiplexed single-photon detectors. *Phys. Rev. A*, 68(4):43814, 2003.

[59] P. Kok and S. L. Braunstein. Detection devices in entanglement-based optical state preparation. *Phys. Rev. A*, 63(3):33812, 2001.

[60] E. Dauler. *Photon-number resolution with SNSPDs.* Internal memo, Quantum Nanostructures and Nanofabrication group, MIT, 2007.

[61] E. Knill, R. Laflamme, and G. J Milburn. A scheme for efficient quantum computation with linear optics. *Nature (London)*, 409:46, 2001.

[62] A.J. Kerman, E.A. Dauler, B.S. Robinson, R. Barron, D.O. Caplan, M.L. Stevens, J.J. Carney, S.A. Hamilton, W.E. Keicher, J.K.W. Yang, K. Rosfjord, V. Anant, and K.K. Berggren. Superconducting nanowire photon-counting detectors for optical communications. *Lincoln Laboratory Journal*, 16:217, 2006.

[63] G. Gol'tsman, O. Okurov, G. Chulkova, A. Lipatov, A. Semenov, K. Smirnov, B. Voronov, A. Dzardanov, C. Williams, and R. Sobolewski. Picosecond superconducting single-photon optical detector. *Appl. Phys. Lett.*, 79(6):705, 2001.

[64] Y. Wang and E. Irene. Consistent refractive index parameters for ultrathin SiO_2 films. *J. Vac. Sci. Technol. B*, 18(1):279, 2000.

[65] K. Herbert, S. Zafar, E. Irene, R. Kuehn, T. McCarthy, and E. Demirlioglu. Measurement of the refractive index of thin SiO_2 films using tunneling current oscillations and ellipsometry. *Appl. Phys. Lett.*, 68(2):266, 1996.

[66] A. DeFranzo and B. Pazol. Index of refraction measurement on sapphire at low temperatures and visible wavelengths. *Appl. Opt.*, 32(13):2224, 1993.

[67] X. J. Yu and H. S. Kwok. Optical wire-grid polarizers at oblique angles of incidence. *J. Appl. Phys.*, 93(8):4407, 2003.

[68] P. Yeh. New optical-model for wire grid polarizers. *Opt. Commun.*, 26(3):289, 1978.

[69] J. Aizpurua, P. Hanarp, D. S. Sutherland, M. Kall, G. W. Bryant, and F. J. G. de Abajo. Optical properties of gold nanorings. *Phys. Rev. Lett.*, 90(5):057401, 2003.

[70] S. O'Brien and J. B. Pendry. Magnetic activity at infrared frequencies in structured metallic photonic crystals. *J. Phys.-Condens. Mat.*, 14(25):6383, 2002.

[71] P. Mühlschlegel, H. J. Eisler, O. J. F. Martin, B. Hecht, and D. W. Pohl. Resonant optical antennas. *Science*, 308(5728):1607, 2005.

[72] Eugene Hecht. *Optics.* Addison-Wesley, Reading, Mass., 4th edition, 2002.

[73] S. M. Rytov. Electromagnetic properties of a finely stratified medium. *Sov. Phys. JETP*, 2:466, 1956.

[74] P. Yeh, A. Yariv, and C. S. Hong. Electromagnetic propagation in periodic stratified media. I. general theory. *J. Opt. Soc. Am.*, 67(4):423, 1977.

[75] A. Yariv and P. Yeh. Electromagnetic propagation in periodic stratified media. II. birefringence, phase matching, and x-ray lasers. *J. Opt. Soc. Am.*, 67(4):438, 1977.

[76] P. Yeh. New optical-model for wire grid polarizers. *Opt. Commun.*, 26(3):289, 1978.

[77] Measurement made at room temperature by J. A. Woolam, Inc. using spectroscopic ellipsometry on a 12-nm-thick NbN film deposited on a sapphire wafer.

[78] I. H. Malitson. Refraction and dispersion of synthetic sapphire. *J. Opt. Soc. Am.*, 52(12):1377, 1962.

[79] P. Lalanne and D. Lemercier-Lalanne. Depth dependence of the effective properties of subwavelength gratings. *J. Opt. Soc. Am. A*, 14(2):450, 1997.

[80] M. G. Moharam and T. K. Gaylord. Diffraction analysis of dielectric surface-relief gratings. *J. Opt. Soc. Am.*, 72(10):1385, 1982.

[81] Allen Taflove and Susan C. Hagness. *Computational electrodynamics : the finite-difference time-domain method.* Artech House antennas and propagation library. Artech House, Boston, 3rd edition, 2005.

[82] K. S. Yee. Numerical solution of initial boundary value problems involving Maxwell's equations in isotropic media. *IEEE Trans. Ant. Prop.*, 14(4):302, 1966.

[83] K. L. Shlager and Schneider J. B. A selective survey of the finite-difference time-domain literature. *IEEE Ant. Propagat. Mag.*, 37(4):39–56, August 1995.

[84] P. J. Schuck, D. P. Fromm, A. Sundaramurthy, G. S. Kino, and W. E. Moerner. Improving the mismatch between light and nanoscale objects with gold bowtie nanoantennas. *Phys. Rev. Lett.*, 94(1):017402, 2005.

[85] A. Farjadpour, D. Roundy, A. Rodriguez, M. Ibanescu, P. Bermel, J. D. Joannopoulos, S. G. Johnson, and G. W. Burr. Improving accuracy by subpixel smoothing in the finite-difference time domain. *Opt. Lett.*, 31(20):2972, 2006.

[86] A.K. Wong and A.R. Neureuther. Rigorous three-dimensional time-domain finite-difference electromagnetic simulation for photolithographic applications. *IEEE Trans. Semicond. Manuf.*, 8(4):419, 1995.

[87] J. N. Reddy. *An introduction to the finite element method.* McGraw-Hill, New York, 1984.

[88] Comsol Multiphysics v. 3.2 Electromagnetics Module User's Guide.

[89] Edward D. Palik. *Handbook of optical constants of solids.* Academic Press handbook series. Academic Press, Orlando, 1985.

[90] Joel K. Yang. *Fabrication of superconducting nanowire single proton detectors.* M.S. thesis, Massachusetts Institute of Technology, 2005.

[91] J. K. W. Yang, V. Anant, and K. K. Berggren. Enhancing etch resistance of hydrogen silsesquioxane via postdevelop electron curing. *J. Vac. Sci. Technol. B*, 24(6):3157, 2006.

[92] T. Chang. Proximity effect in electron-beam lithography. *J. Vac. Sci. Technol. B*, 12(6):1271, 1975.

[93] These parameters were obtained from the Raith 150 software for a sapphire substrate.

[94] A. J. Kerman, E. A. Dauler, J. K. W. Yang, K. M. Rosfjord, V. Anant, K. K. Berggren, G. N. Gol'tsman, and B. M. Voronov. Constriction-limited detection efficiency of superconducting nanowire single-photon detectors. *Appl. Phys. Lett.*, 90(10):101110, 2007.